POLYPUBLIE

Multi-Modality Diffuse Fluorescence Imaging Applied to Preclinical Imaging in Mice

Baoqiang Li

Document en libre accès dans PolyPublie
Open Access document in PolyPublie

Date	2014
Type	Mémoire ou thèse / Dissertation or Thesis Thèse de doctorat/Ph.D. thesis
URL de PolyPublie PolyPublie URL	https://publications.polymtl.ca/1448/
Conditions d'utilisation Terms of use	© Tous droits réservés / All rights reserved
Référence Citation	Li, B. (2014). Multi-Modality Diffuse Fluorescence Imaging Applied to Preclinical Imaging in Mice [Thèse de doctorat, École Polytechnique de Montréal]. PolyPublie. https://publications.polymtl.ca/1448/

Détails de la thèse
Thesis details

Directeurs de recherche Advisors	Frédéric Lesage
Programme Program	Génie biomédical

Ce fichier a été téléchargé à partir de PolyPublie, le dépôt institutionnel de Polytechnique Montréal
This file has been downloaded from PolyPublie, the institutional repository of Polytechnique Montréal
https://publications.polymtl.ca

UNIVERSITÉ DE MONTRÉAL

MULTI-MODALITY DIFFUSE FLUORESCENCE IMAGING APPLIED TO PRECLINICAL IMAGING IN MICE

BAOQIANG LI
INSTITUT DE GÉNIE BIOMÉDICAL
ÉCOLE POLYTECHNIQUE DE MONTRÉAL

THÈSE PRÉSENTÉE EN VUE DE L'OBTENTION
DU DIPLÔME DE PHILOSOPHIÆ DOCTOR
(GÉNIE BIOMÉDICAL)
JUILLET 2014

© Baoqiang Li, 2014.

UNIVERSITÉ DE MONTRÉAL

ÉCOLE POLYTECHNIQUE DE MONTRÉAL

Cette thèse intitulée:

MULTI-MODALITY DIFFUSE FLUORESCENCE IMAGING APPLIED TO PRECLINICAL IMAGING IN MICE

présentée par : LI Baoqiang
en vue de l'obtention du diplôme de : Philosophiæ Doctor
a été dûment acceptée par le jury d'examen constitué de :

M. LEBLOND Frédéric, Ph. D., président
M. LESAGE Frédéric, Ph. D., membre et directeur de recherche
M. SAVARD Pierre, Ph. D., membre
M. NEAR Jamie, Ph. D., membre

DEDICATION

To My Family

致我的家人

ACKNOWLEDGMENTS

This work embraces not only my effort but many others'. First, I would like to thank Prof. Frederic Lesage who accepted me in his group, and the China Scholarship Council that awarded me a scholarship from the "*Chinese government graduate student overseas study program*", which practically facilitated my ideal of studying abroad, following, initiated my long, but memorable journey to Montreal, Canada.

Next, living in Montreal, it was very pleasant to find kind friends, with whom I spent many of our week-ends and holidays to explore the city finding new and interesting aspects to spice up our lives.

I sincerely thank all the staff in the animal facility at the Montreal Heart Institute, particularly Natacha Duquette, Marc-Antoine Gillis, Vanessa Durocher-Granger, Karine Nadeau and Robert Clement. Their assistance in the animal manipulation and administrative management truly facilitated my scientific works with animals. I furthermore want to specially acknowledge my colleagues: Maxime Abran, Romain Berti, Foued Maafi and Philippe Pouliot, who provided invaluable technical and experimental support to my research. I am also grateful to other members who worked previously or currently in the LIOM Laboratory at Polytechnique, with whom we have built a multi-cultural, harmonious and collaborative working environment for our lab: Mahnoush Amiri, Pramod Avti, Simon Archambault, Clement Bonnery, Edward Baraghis, Samuel Belanger, Karim Zerouali-Boukhal, Alexandre Castonguay, Zhang Cong, Michele Desjardins, Simon Dubeau, Peng Ke, Joel Lefebvre, Alexis Machado, Mohammad Moeini, Emilie Beaulieu-Ouellet, Nicolas Ouakli, Carl Matteau-Pelletier, Leonie Rouleau, Abas Sabouni, Maryam Sadat Tabatabaei Shafiei and Tri Truong Van.

In the end, I want to, again, wholeheartedly express my gratitude to my PhD supervisor, a talented scientist and a dedicated professor: Frederic Lesage, with all the support and help he offered to my research and life. His patient and earnest coaching let me get into, following, understand my research subject. And his instruction and direction on my research works helped me gradually build confidence and develop deep interest in this research field, which I believe will benefit my research career for the future.

RÉSUMÉ

Cette thèse vise à explorer l'information anatomique et fonctionnelle en développant de nouveaux systèmes d'imagerie de fluorescence macroscopiques à base de multi-modalité. L'ajout de l'imagerie anatomique à des modalités fonctionnelles telles que la fluorescence permet une meilleure visualisation et la récupération quantitative des images de fluorescence, ce qui en retour permet d'améliorer le suivi et l'évaluation des paramètres biologiques dans les tissus. Sur la base de cette motivation, la fluorescence a été combinée avec l'imagerie ultrasonore (US) d'abord et ensuite l'imagerie par résonance magnétique (IRM). Dans les deux cas, les performances du système ont été caractérisées et la reconstruction a été évaluée par des simulations et des expérimentations sur des fantômes. Finalement, ils ont été utilisés pour des expériences d'imagerie moléculaire in vivo dans des modèles de cancer et d'athérosclérose chez la souris. Les résultats ont été présentés dans trois articles, qui sont inclus dans cette thèse et décrits brièvement ci-dessous.

Un premier article présente un système d'imagerie bimodalité combinant fluorescence à onde continue avec l'imagerie à trois dimensions (3D) US. A l'aide de stages X-Y motorisés, le système d'imagerie a été en mesure de recueillir l'émission fluorescente et les échos acoustiques délimitant la surface 3D et la position des inclusions fluorescentes dans l'échantillon. Une validation sur fantômes, a montré que l'utilisation des priors anatomiques provenant des US améliorait la qualité de la reconstruction fluorescente. En outre, un étude pilote in-vivo en utilisant une souris Apo-E a évalué la faisabilité de cette approche d'imagerie double modalité pour de futures études pré-cliniques.

Dans un deuxième effort, et sur la base du premier travail, nous avons amélioré le système d'imagerie par fluorescence-US au niveau des algorithmes, de la précision

d'échantillonnage et de la reconstruction. Plus précisément, en combinant maintenant imagerie ultrasonore et la profilométrie, à la fois la cible fluorescente et une surface 3D de l'échantillon peuvent être obtenues permettant une meilleure reconstruction de fluorescence. De plus, une reconstruction basée sur des patrons mesurés sur la surface de détection a été utilisée pour augmenter l'efficacité du calcul tout en préservant l'information utile. En retour, cette approche a nécessité une correction de la normalisation de Born. Il a été démontré par des simulations et des fantômes que les cibles fluorescentes pourraient être récupérés plus précisément et quantitativement par cette mise à niveau instrumentale et numérique. Enfin, ce système a été validé en imagerie in vivo avec un modèle de tumeurs précliniques. Les résultats ont confirmé que cette approche d'imagerie a été en mesure d'extraire des informations à la fois anatomiques et fonctionnelles, améliorant ainsi la quantification et la localisation des cibles moléculaires.

Le troisième article a développé un système multi- modalité combinant la tomographie moléculaire fluorescente (FMT) avec l'IRM à nouveau dans le but de faciliter la récupération et l'interprétation des informations fonctionnelles. Nos expériences sur fantôme et souris morte montrent que des modèles hétérogènes des propriétés optiques, dérivés d'images IRM, sont supérieurs à ceux homogènes pour quantifier la fluorescence. Le système FMT- IRM a été utilisé pour effectuer de l'imagerie moléculaire in vivo avec un modèle souris d'athérosclérose. Les résultats ont montré que les modèles hétérogènes donnent lieu à des reconstructions qui corrèlent mieux avec les données ex vivo que leurs homologues homogènes.

Globalement, cette thèse a été consacrée au développement de systèmes multi-modalité pour mesurer la fluorescence chez la souris. Les résultats des trois articles ont évalué la faisabilité et les performances de l'approche d'imagerie combinée à des simulations, des fantômes

et des souris in vivo. Les résultats suggèrent que la multi-modalité en appui à la fluorescence peut être un outil puissant pour les études précliniques et biologiques chez la souris.

ABSTRACT

This thesis aims to explore the anatomical and functional information by developing new macroscopic multi-modality fluorescence imaging schemes. Adding anatomical imaging to functional modalities such as fluorescence enables better visualization and recovery of fluorescence images, in turn, improving the monitoring and assessment of biological parameters in tissue. Based on this motivation, fluorescence was combined with ultrasound (US) imaging first and then magnetic resonance imaging (MRI). In both cases, the systems characterization and reconstruction performance were evaluated by simulations and phantom experiments. Eventually, they were applied to *in vivo* molecular imaging in models of cancer and atherosclerosis in mice. Results were presented in three peer-reviewed journals, which are included in this thesis and shortly described below.

A first article presented a dual-modality imaging system combining continuous-wave transmission fluorescence imaging with three dimensional (3D) US imaging. Using motorized X-Y stages, the fluorescence-US imaging system was able to collect boundary fluorescent emission, and acoustic pulse-echoes delineating the 3D surface and position of fluorescent inclusions within the sample. A validation in phantoms showed that using the US anatomical priors, the fluorescent reconstruction quality was significantly improved. Furthermore, a pilot *in-vivo* study using an Apo-E mouse evaluated the feasibility of this dual-modality imaging approach for future animal studies.

In a second endeavor, and based on the first work, we improved the fluorescence-US imaging system in terms of sampling precision and reconstruction algorithms. Specifically, now combining US imaging and profilometry, both the fluorescent target and 3D surface of sample could be obtained in order to achieve improved fluorescence reconstruction. Furthermore, a

pattern-based fluorescence reconstruction on the detection side was used to achieve a computational efficient but informative reconstruction. In turn, this required a correction of the standard Born-normalization by decreasing the attenuation effect for a quantitative fluorescence datasets. It was demonstrated with simulations and phantoms that the fluorescent targets could be recovered more accurately and quantitatively by this instrumental and computational upgrade. Finally, this system was validated during *in vivo* imaging with a preclinical tumor model. Results confirmed that this imaging approach was able to extract both functional and anatomical information, thereby improving quantification and localization of molecular targets.

The third article developed a multi-modality system combining fluorescent molecular tomography (FMT) with MRI again with the goal of facilitating recovering and interpreting functional information. Our investigations in phantom and dead mouse show that heterogeneous models derived from MRI images were superior to homogeneous ones in quantifying fluorescence. The FMT-MRI system was the used to perform *in vivo* atherosclerosis molecular imaging with mice. Results showed that, the MRI-derived heterogeneous models resulted in reconstructions correlating better with the *ex vivo* measurements than their homogeneous counterparts did.

Overall this thesis was dedicated to multi-modality targeted fluorescence imaging in mice. Results from the three articles evaluated the feasibility and performance of the combined imaging approach in simulations, phantoms and mice *in vivo*. Results suggested that multi-modality fluorescence imaging might serve as a potent tool for preclinical and biological study in mice.

TABLE OF CONTENTS

DEDICATION III

ACKNOWLEDGMENTS IV

RÉSUMÉ VI

ABSTRACT IX

TABLE OF CONTENTS XI

LIST OF TABLES XVI

LIST OF FIGURES XVII

LIST OF ACRONYMS AND ABBREVIATIONS XXI

CHAPTER 1 GENERAL CONTEXT 1

1.1 Overview 1

1.2 Brief literature review 3

1.3 Organization of the thesis by objectives 17

CHAPTER 2 THEORY OF DIFFUSE FLUORESCENCE IMAGING 20

2.1 Forward modeling 20

2.2 Inverse problem 24

2.3 Prior guided fluorescence reconstruction 25

CHAPTER 3 ARTICLE #1: LOW-COST THREE-DIMENSIONAL IMAGING SYSTEM COMBINING FLUORESCENCE AND ULTRASOUND 27

3.1 Presentation of the article 27

3.2 Abstract 27

3.2.1 Key words 28

3.3 Introduction 28

3.4 Methodology 32
3.4.1 System design 32
3.4.2 Reconstruction 34
3.4.3 Phantoms 35
3.5 Results 37
3.5.1 Sensitivity tests 37
3.5.2 Phantom tests 38
3.5.3 In vivo results 46
3.5.4 Analysis of the results 50
3.6 Discussion 51
3.7 Conclusion 54
3.8 Acknowledgements 54
3.9 References 54
CHAPTER 4 ARTICLE #2: ULTRASOUND GUIDED FLUORESCENCE MOLECULAR TOMOGRAPHY WITH IMPROVED QUANTIFICATION BY AN ATTENUATION COMPENSATED BORN-NORMALIZATION AND IN VIVO PRECLINICAL STUDY OF CANCER 59
4.1 Presentation of the article 60
4.2 Abstract 60
4.2.1 Key words 61
4.3 Introduction 61
4.4 Methods 64
4.4.1 System design 64

4.4.2 Attenuation compensated born normalization 67
4.4.3 Reconstruction 77
4.4.3.1 Pattern-based forward modeling 77
4.4.3.2 A combined structural prior 78
4.4.3.3 Inverse problem 78
4.4.4 Simulations 79
4.4.5 Phantom reconstruction 83
4.5 Experiment 85
4.6 Results 86
4.6.1 Fluorescence imaging with the ACBN method 86
4.6.2 Reconstruction results 88
4.6.3 Ex-vivo evaluation 89
4.7 Discussion 91
4.8 Conclusion 92
4.9 Acknowledgments 92
4.10 References 93
CHAPTER 5 ARTICLE #3: HYBRID FMT-MRI APPLIED TO IN VIVO ATHEROSCLEROSIS IMAGING 99
5.1 Presentation of the article 99
5.2 Abstract 99
5.3 Introduction 100
5.4 System 101
5.4.1 FMT system design 101

5.4.2 Optical probe design 103
5.5 Reconstruction 104
5.5.1 MR anatomy guided forward modeling 104
5.5.2 MR-prior constrained reconstruction 105
5.6 Experiments 107
5.6.1 Phantom experiment 107
5.6.2 Mouse corpse experiment 108
5.6.3 In vivo experiment 108
5.7 Results 110
5.7.1 Phantom experiment 110
5.7.2 Mouse corpse experiment 113
5.7.3 In vivo experiment 115
5.8 Discussion 117
5.9 Conclusion 119
5.9 Acknowledgments 119
5.10 References 119
CHAPTER 6 GENERAL DISCUSSION 124
6.1 Article #1 124
6.1.1 System characterization 124
6.1.2 Limitations 124
6.2 Article #2 125
6.2.1 System design 125
6.2.2 Attenuation compensated born normalization and pattern based reconstruction 125

6.2.3 In-vivo imaging with preclinical tumorous mice 126

6.2.4 Limitations 126

6.3 Article #3 126

6.3.1 Advantages 126

6.3.2 Atherosclerotic imaging with mice 127

6.3.3 Limitations 127

CHAPTER 7 CONCLUSION 128

REFERENCES 130

LIST OF TABLES

Table 3.1: Optical properties for both phantoms. Phantom 1 and 2 represent the rectangular phantom and semi-cylindrical phantom, respectively. 37

Table 3.2: CNR of the reconstruction images. CNR1 and CNR2 represent the CNR of the reconstructions with prior and the ones without priors, respectively. 50

Table 4.1: Dimension and optical properties of phantom. 72

Table 4.2: Four cases of the experiment. 73

Table 5.1: Dimension and optical properties of the phantom. 107

LIST OF FIGURES

Figure 3.1: Schematic of this dual-modality imaging system. 33

Figure 3.2: (a) Dimension of the rectangular phantom: phantom 1. (b)-(c) Schematic depiction showing the four heterogeneities (denoted by diff 1-4) and two holes for inserting fluorescent tubes (denoted by fluo 1-2). (d) Dimension of the semi-cylindrical phantom, phantom 2. 36

Figure 3.3: Illustration of measuring position in the sensitivity test. The red arrows represent the laser diode and the detection fiber. 37

Figure 3.4: (a) normalized values of different concentration as a function of scan position. The results show that the system was able to detect 1nm cy5.5 in the phantom; (b) the curve shows the fitted logarithmic peak values as a function of concentrations. The triangular markers denote the normalized amplitude of different concentrations. 38

Figure 3.5: (a) The normalized fluorescence intensity of phantom 1. (b) The normalized fluorescence signal of phantom 2. (c) The dimensions of the plastic tube. 40

Figure 3.6: Representative images of the acquisition using phantom 1. The US images (a), (d), (g), the fluorescence reconstruction image ($\eta\mu_{fl}$ in mm^{-1}) with priors (b), (e), (h), and without priors (c), (f), (i) are shown for image slices at x=20 (a)-(c), at y=14 (d)-(f) and at y=32 (g)-(i) respectively. Intensity plots along the red (j) dashed line in Figure 3.6 (e) and along the green (k) dashed line in Figure 3.6 (h) are also shown. 43

Figure 3.7: (a) Overlaid image at x=20. (b) Overlaid image at y=14. (c) Overlaid image at y=32. 44

Figure 3.8: Representative images using phantom 2. The US images (a) and (d), the fluorescence reconstruction image ($\eta\mu_{fl}$ in mm^{-1}) with priors (b) and (e), and without priors (c) and (f) are shown for image slices at x=12 (a)-(c) and at y=18 (d)-(f). Intensity plot along the red (g) dashed line in Figure 3.8 (e) is also shown. 45

Figure 3.9: (a) Overlaid image at x=12. (b) Overlaid image at y=18. 46

Figure 3.10: (a) The BN ratio overlaid with the picture. (b) Illustration of the animal manipulation. 47

Figure 3.11: Representative images of slice 3-1 of the mouse: (a) The US image shows the heart of the mouse; (b) the fluorescence reconstruction image ($\eta\mu_{fl}$ in mm^{-1}) with priors and (c) without. 49

Figure 3.12: The overlaid image of slice 3-1. 49

Figure 3.13: Quantification with the two phantoms by comparing the normalized maximum value of $\eta\mu_{fl}$ in each fluorescence image slice. 51

Figure 4.1: (a) System schematics of the Fluorescence-US imaging system; (b) photo of the imaging system; and the window for the scanning of both the laser source and the US transducer is indicated by the yellow square; (c) the scanning window is showed by an enlarged view; and the animal installation is also illustrated. 66

Figure 4.2: Illustration of light propagating in tissue. here, r_s and r_d represents an arbitrary source and detector position, respectively; l represents one effective traveling path of the incident light from r_s to r_d ; l' is a representative travelling path of the incident photons from r_s to fluorophore; l^x is a representative traveling path of fluorescent photons from the fluorophore to r_d 67

Figure 4.3: Illustration of the phantom and the inclusions. Here, S_a and S_b are the two surfaces of the phantom along the Z direction; F_a and F_b are two holes to insert the fluorescent tubes; D_a and D_b are the two heterogeneous inclusions. 71

Figure 4.4: Phantom images for the four cases: the first row shows the ROI for each scan; the second row shows the fluorescence images processed with the standard BN method; the third row shows the standard BN ratio images with only the measurement of the detector co-linear with the source; finally, the fourth row shows the fluorescence images processed with the ACBN method. 74

Figure 4.5: Representative image slices. (a) The segmentation of tissue types derived from the combined structural prior; (b) the localization was accurately reconstructed with prior; (c) reconstruction without structural prior. 80

Figure 4.6: (a) The true value of $\varepsilon\eta C$ only in the tumor region was changed; but the initial estimate was kept constant; (b) the true value of $\varepsilon\eta C$ was constant; but the initial estimate was changed; (c) the true values of $\varepsilon\eta C$ in both tissue regions were changed; and the value of the tumor region remained 4 times greater than that of the normal tissue region; but the but the initial estimate was kept constant; (d) true values in both tissue-type regions were constant, and the initial estimate was constant too. The reconstructed was assessed with different noise levels. 83

Figure 4.7: The comparison of the reconstruction between the ACBN method and the standard BN method. 85

Figure 4.8: As a representative, the tumor is approximately indicated by the dashed circle. 85

Figure 4.9: (a) The ROI of imaging was indicated by the red spots; (b)-(c) the fluorescence images acquired before and after injection of the molecular probe for the control; (d)-(e) the fluorescence images acquired before and after injection of the molecular probe for Tumor #1; (f)-(g) the fluorescence images acquired before and after injection of the molecular probe for Tumor #2... 87

Figure 4.10: (a)-(c) For Tumor #1, a representative US image slice and two representative fluorescence images overlaid the corresponding US image slices are shown; (d)-(f) For Tumor #2, a representative US image slice and two representative fluorescence images overlaid the corresponding US image slices are shown. 89

Figure 4.11: (a) Ex-vivo images of the tumors for Tumor #1 and Tumor #2. The ratio between the maximum reconstructed $\varepsilon\eta C$ of Tumor #1 and that of Tumor #2 is 1:0.61; (b) the maximum reconstructed $\varepsilon\eta C$ for Tumor #1 and Tumor #2 is shown with the ACBN method as well as the standard BN method. 90

Figure 5.1: Schematic (top) and photograph (bottom) of the FMT system. GM: Galvo mirror; EF: excitation fibers; DF: detection fibers; LD: laser driver; FW: Filter wheel..... 102

Figure 5.2: Schematic diagram (left, top side) and photograph (right) of the optical probe working in an experiment. AH: animal holder; AP: animal plate; FMR: fiducial marker..... 104

Figure 5.3: (a) Representative axial MR slice of ATX #2; (b) segmented image; (c) resampled segmented image with 1 mm voxel resolution. 104

Figure 5.4: Schematic diagram of the phantom: (a) view of X-Y plane; (b) view of X-Z plane. The attenuation and fluorescence inclusions are denoted by Diff and Fluo, respectively. 107

Figure 5.5: (a) A synthetic fluorescence slice of the phantom; (b) the corresponding slices of the reconstruction with the heterogeneous models (b), and with the homogeneous model (c), respectively; (d) plot of reconstructed values along the red dashed line. (e) CNR was compared with λ for both models. 110

Figure 5.6: (a) Ex vivo images of the fluorescent tubes were overlaid with transparency (alpha=0.5) on the photographs of tubes, respectively; (b) the average reconstructed values (both models) of the fluorescent tubes were normalized of the maximum being 1, to compare with the ex vivo measurement (reference). 112

Figure 5.7: (a) Three orthogonal MR slices are shown: axial slice (Y-Z), coronal slice (X-Y) and sagittal slice (X-Z). The arrow of the X axes points to tail of the mouse; and the arrow of the Z axes points to abdomen. The tube was indicated by the red arrow; (b) the reconstructions with the heterogeneous models were overlaid with transparency (alpha=0.5) on the MR slices, respectively; (c) the reconstructions with the homogeneous models were overlaid with transparency (alpha=0.5) on the MR slices, respectively. 113

Figure 5.8: The images in the first column are the MR slices for each mouse. Heart and part of aorta of ATX #1 were denoted by red arrows. In the second column, the reconstructed $\varepsilon\eta C$ with the heterogeneous models were overlaid with transparency (alpha=0.5) on the MR slices, respectively. Three orthogonal MR slices were chosen for each mouse: axial slice (Y-Z), coronal slice (X-Y) and sagittal slice (X-Z). 115

Figure 5.9: The hearts and aortas of the four mice were imaged ex vivo. In the first row, the ex vivo fluorescence images were overlaid with transparency (alpha=0.5) on the corresponding photographs. Shown by the curves below, the average reconstructed $\varepsilon\eta C$ of the hearts and aortas for all mice were normalized with the maximum being 1 to compare with the ex vivo measurement. 116

LIST OF ACRONYMS AND ABBREVIATIONS

AFA	Angular filter array
BEM	Boundary element method
BM	Boundary measurement
BN	Born-normalization
CNR	Contrast to noise ratio
CT	Computed tomography
CW	Continuous-wave
3D	Three dimensional
DFI	Diffuse fluorescence imaging
DOT	Diffuse optical tomography
EMCCD	Electron multiplying charge coupled device
FEM	Finite element method
FLI	Fluorescence lifetime imaging
FOV	Field of view
FMT	Fluorescence molecular tomography
GPU	Graphics processing unit
Hb	Deoxy-hemoglobin
HbO_2	Oxy-hemoglobin
ICG	Indocyanine green
MC	Monte Carlo
MEMS	Microelectromechanical systems
MicroCT	Microcomputed tomography

MRI	Magnetic resonance imaging
MMP	Matrix metalloproteinases
PAT	Photo-acoustic tomography
PCA	Principal component analysis
PET	Positron emission tomography
PMT	Photomultiplier tube
PpIX	Protoporphyrin IX
ROI	Region of interest
RTE	Radiative transfer equation
SNR	Signal to noise ratio
TR	Tikhonov regularization
US	Ultrasound
μ_s'	Reduced scattering coefficient
μ_a	Absorption coefficient

CHAPTER 1 GENERAL CONTEXT

1.1 Overview

Diffuse Fluorescence Imaging (DFI) has been widely used in biological, preclinical and clinical studies because of its excellent sensitivity and specificity (Gibson, Hebden, & Arridge, 2005; Frederic Leblond, Davis, Valdés, & Pogue, 2010; Frederic Leblond, Tichauer, Holt, El-Ghussein, & Pogue, 2011). With the administration of an exogenous fluorescent molecular probe, receptors expressed during a given disease could be targeted. In some cases, enzymes can activate a probe to fluoresce, specifically expressing the activity of the targeted molecules (H. H. Chen et al., 2013; Jaffer, Libby, & Weissleder, 2009a; Ripplinger et al., 2012; Sanz & Fayad, 2008; Tardif, Lesage, Harel, Romeo, & Pressacco, 2011; Vries et al., 2009). In both cases, the fluorescent molecules act as an antenna: after being excited, the fluorescent photons escaping from the tissue can be detected on the boundary of the tissue by a fluorescence imaging system. To quantify the received fluorescence, these boundary measures will be taken as input for a model-based 3D fluorescence reconstruction (Gibson et al., 2005). Following this modeling, with the reconstruction algorithm, fluorescent concentration can be quantified and localized, thereby, revealing the molecular activities in the progression of the disease (Markel, Mital, & Schotland, 2003).

In Fluorescence Molecular Tomography (FMT), light within the wavelength range 650 nm to 800 nm is typically employed in the form of collimated beam or wide-field patterns to excite the fluorophores in a given sample (Ntziachristos, Bremer, & Weissleder, 2003). The reason is that within this range of wavelengths, the main absorbers in tissue, e.g. deoxy-hemoglobin (Hb), oxy-hemoglobin (HbO_2) and water have relatively low absorption, which

allows deeper penetration in tissue and enable signal detection with better signal to noise ratio (SNR) (S. A. Prahl, n.d.; L. V. Wang & Wu, 2007).

In contrast to microscopic imaging techniques, FMT belongs to the regime of macroscopic diffuse light imaging and provides millimeter-level spatial resolution, but preserves the ability to image up to several centimeters deep in tissue (L. V. Wang & Wu, 2007). Distinct from anatomical imaging modalities, such as X-ray computed tomography (CT), magnetic resonance imaging (MRI) and ultrasound (US), it yields functional information about the biological processes or activities of disease-related molecules (Ntziachristos et al., 2003). Furthermore, when compared to ionizing imaging techniques, such as contrast enhanced X-ray CT or positron emission tomography (PET) (Fu et al., 2013; Nahrendorf et al., 2010; Ricketts, Guazzoni, Castoldi, Gibson, & Royle, 2013), FMT is non-ionizing, thus, does not create a risk for subjects with the imaging tasks. Therefore, given its simplicity and low-cost, FMT may have great potential in biological and preclinical/clinical applications.

Depending on the excitation mechanism, fluorescence imaging can be divided into frequency-domain, continuous-wave (CW) and time-domain fluorescence imaging (L. V. Wang & Wu, 2007). In the frequency-domain, the excitation light wave is modulated with a high frequency (e.g. 100MHz) and the measurement consists of both amplitude and phase information of the emitted photons. However, CW mode is a special case of the frequency-domain with modulation frequency set to zero. In this case the measurement only contains amplitude information. In the time-domain technique, a pulsed laser is typically used to excite the fluorophore and the emitted photons are recorded by a time-gated camera or photon-counting device. The frequency-domain and time-domain are more complex than the CW technique in term of system design but could offer more informative datasets to resolve both concentration

and lifetime of the injected fluorophores in tissue. However, the CW system has advantages in low-cost, easy implementation, and fast acquisitions. Beyond these three modes, recently efforts in optimizing the illumination spatial pattern were done. A spatial domain frequency method was reported in several studies, e.g. to resolve optical properties in tissue (Weber et al., 2011) as well as enhance resolution and contrast of fluorescence imaging (Mazhar et al., 2010).

In the next sub-chapter, different aspects of FMT will be introduced by briefly reviewing the recent literature. The versatility of the fluorescence imaging tools will first be reviewed for a variety of applications. Second, FMT, or in general, diffuse fluorescence imaging instrumentation will be summarized using recent studies. Then, the latest development of hybrid-modal FMT and its advantages will be briefly reviewed. Finally, we will review the computational progress in FMT, including both forward and inverse problems as well as the data calibration techniques.

1.2 Brief literature review

Applications

Diffuse fluorescence imaging, in general, has been mainly used in preclinical and biological studies. Several studies in-vivo were conducted showing that lymphatic function could be evaluated by monitoring the fluorescence signal in the micro-circulation following the administration of indocyanine green (ICG) (Kwon, Agollah, Wu, Chan, & Sevick-Muraca, 2013; Kwon & Sevick-Muraca, 2011; Solomon et al., 2011). The results suggested that by imaging fluorescence in lymphatic nodes, lymphatic architecture could be visualized and the progression and metastasis of cancer might be staged. Until now, tumorous/cancerous imaging remains one of primary applications with fluorescence imaging. Using wide-field fluorescence lifetime imaging (FLI), surface tumors could be detected by auto-fluorescence imaging of the skin at

video-rates (McGinty et al., 2010). In other studies, fluorescence imaging combined with other imaging techniques or working alone were employed to characterize tissue properties for the diagnosis of skin cancer (Dancik, Favre, Loy, Zvyagin, & Roberts, 2013; Gruber et al., 2010a; Nie, An, Hayward, Farrell, & Fang, 2013; Sunar, Rohrbach, Morgan, Zeitouni, & Henderson, 2013). These studies suggest a great potential of translation to humans for biopsy of cancerous tissue. Fluorescence imaging was also employed to characterize brain tumors by using near-infrared dyes (Davis et al., 2010; Fortin et al., 2012). The biophysics underlying these applications is that lesions and normal tissues will show distinctive characterizations with respect to the accumulation and metabolism of the fluorescent dye reflected by different levels of fluorescent signal intensity and pharmacokinetic rate. Using this principle, tumor neo-vasculature was measured by dynamic fluorescence imaging (M. Choi, Choi, Ryu, Lee, & Choi, 2011); and tumor contrast was obtained by late-fluorescence mammography aiming to separate malignant lesions by assessing tumor capillary permeability (Hagen et al., 2009). Furthermore, fluorescence imaging was employed intraoperatively to delineate lesion (tumor) margins (Q. Zhao, Jiang, et al., 2011) or to guide the concurrent surgery (Themelis, Yoo, Soh, Schulz, & Ntziachristos, 2009). It has been argued that the spectroscopic information measured during fluorescence imaging could aid in the diagnosis of many other carcinomatous diseases, such as oral cancer (Fatakdawala et al., 2013), glioma tumors in the brain (Gibbs-Strauss et al., 2009), prostate cancer (Boutet et al., 2009) and pancreatic cancer at early stage (Erten et al., 2010). Fluorescence imaging was also demonstrated using tomographic approaches to quantify and localize tumors (Ale, Ermolayev, Deliolanis, & Ntziachristos, 2013; Deliolanis et al., 2009; D. S. Kepshire et al., 2009; Konecky et al., 2012). In these three representative studies, different techniques in FMT,

such as hybrid modalities, single photon detection and complete-angle projections were explored to retrieve the functional information associated with cancer.

Cardiovascular imaging is another major application of fluorescence imaging. Spectroscopic measures were used to characterize atherosclerotic plaques using time or wavelength resolved detection methods (Larsen et al., 2011; Liu, Sun, Qi, & Marcu, 2012; Sćepanović et al., 2011; Yinghua Sun et al., 2011). Fluorescence imaging was also used to guide surgery for cardiovascular disease (Cooley, 2011). Moreover, as cardiovascular tissue exhibits high absorption due to the enriched blood content, in-vivo atherosclerotic imaging was mainly performed in the form of endoscopy (Bec et al., 2012; Calfon, Vinegoni, Ntziachristos, & Jaffer, 2010; Mallas et al., 2012; Razansky et al., 2010; Xie et al., 2012). In these studies, catheter probes were used to accommodate a fluorescence detector or coupled with additional US transducers to visualize intravascular vessels and characterize atherosclerotic plaques. One in-vivo study reported autophagy imaging in the heart using FMT by recovering cathepsin activity (H. H. Chen et al., 2013). However, until now, very few examples for non-invasive in-vivo atherosclerosis imaging exist. Developing such examples is one of the focus point of this thesis.

Beyond diagnosis, fluorescence imaging also contributed to assess therapy. It was reported that time-domain and spatial frequency domain fluorescence imaging could quantify fluorophore distribution in order to assess photodynamic therapy (Mo, Rohrbach, & Sunar, 2012; Saager, Cuccia, Saggese, Kelly, & Durkin, 2011). In radiotherapy, Cerenkov emission was used to excite fluorescent molecular reporters; ensuing fluorescence mapping could potentially evaluate and monitor tissue response of therapy (Axelsson, Davis, Gladstone, & Pogue, 2011; Demers, Davis, Zhang, Gladstone, & Pogue, 2013). Other examples using FMT include the quantification of asthma severity (Korideck & Peterson, 2008); photon-counting or multispectral

fluorescence techniques enabled pH sensing with biological samples as well as in small animals (Hight et al., 2011; J. Li et al., 2012). Dynamic FLI was used to assess protein-losing nephropathy due to renal diseases (Goiffon, Akers, Berezin, Lee, & Achilefu, 2009). A proof-of-concept study demonstrated the feasibility of employing time-resolved dynamic imaging of ICG to provide information on the blood supply to the brain of humans (Milej et al., 2012); parameters related with imaging geometries and fluorophore wavelength were optimized for imaging amyloid plaques with Alzheimer's disease mice (S B Raymond, Kumar, Boas, & Bacskai, 2009).

Many of the examples introduced above were also extended to humans. In the study of carcinomatous disease, fluorescence imaging combined with diffuse optical tomography (DOT) was employed to measure the pharmacokinetic rate of ICG to discriminate malignant lesions from normal tissue in the human breast (Leproux et al., 2011). Malignant tissue in the human breast could also be distinguished from healthy tissue by measuring deoxy-glucose using wide-field fluorescence imaging (Langsner et al., 2011). In the same application, integration between DOT and time-resolved fluorescence was used to recover optical properties and fluorescent properties towards a comprehensive diagnosis for breast cancer (W. Zhang et al., 2013)(Grosenick et al., 2011). A hand-held fluorescence imaging scheme was proposed and expected to translate into clinical studies (Erickson et al., 2013; Ge, Erickson, & Godavarty, 2010; J, Sj, & A, 2009). Ex-vivo fluorescence imaging was also enabled by activatable molecular probes: multispectral FMT was employed to reveal matrix metalloproteinases (MMPs) activities in the characterization of human carotid plaque (Vries et al., 2009). Multimodal FLI was used to characterize the composition, structure and function of human atherosclerotic plaques ex-vivo (Yang Sun et al., 2011). Different aspects were investigated for fluorescence imaging guided

surgery. Here, a ratiometric fluorescence approach could result in a better delineation of tumor boundary in image guided surgery (F Leblond et al., 2011). This maneuver might even be achievable by a pulsed light excitation fluorescence imaging method to perform surgery under normal room lighting (Sexton et al., 2013).

General development of fluorescence imaging

The applications discussed above demonstrate the versatility of fluorescence as well as the efforts in this field for the development of different aspects. In this sub-section, recent instrumental and methodological advancements of fluorescence imaging will be concisely introduced. Multi-modal imaging and computational developments, such as forward/inverse problems and data calibration techniques will be introduced in the next two sub-sections.

Fluorescence imaging can be performed in different geometries. In epi-illumination mode, both illumination and detection are conducted on the same side of sample. In trans-illumination mode, illumination and detection are conducted on the separate sides of the sample. The former is sensitive to depth, but has limited penetration of light in tissue; and it is less immune to auto-fluorescence contamination. An all optical approach was developed that by dynamically measuring reflectance ICG signal, tissue anatomy could be revealed due to the distinctive pharmacokinetic rate of different tissue types (Hillman & Moore, 2007). It was reported recently that the Mellin-Laplace transform of time-domain reflection data could potentially help probe deep inclusions (Puszka et al., 2013). The transmission measures are less sensitive, but have better ability to detect objects embedded deeply, which would suggest a better SNR for measurements. For example, transmission fluorescence was employed to image biocompatible upconverting nanoparticles embedded in mice, which demonstrated an auto-fluorescence free detection approach (Vinegoni, Razansky, Hilderbrand, et al., 2009). Transmission fluorescence

working in the angular domain might decrease scattering effect to detect deep objects in mice (Vasefi et al., 2009). Here, angular domain refers to a technique using the angular filter array (AFA) to overcome to collect emission photons going through limited scattering events. A more advanced approach is to acquire projection measurement over 360^{o} around the imaging sample, which is expected to combine the merits of both reflection and transmission. Investigators combined both FMT and X-ray CT to acquire projection dataset in both modalities for animal studies in-vivo (Ale et al., 2012a; Ale, Schulz, Sarantopoulos, & Ntziachristos, 2010; Lapointe, Pichette, & Bérubé-Lauzière, 2012).

Besides imaging geometries, the development of detection mechanisms and illumination methods also had significant impact on the imaging performance. It has been broadly reported that time-domain could provide superior information in term of richness of information over CW-mode fluorescence imaging (Holt, Tichauer, Dehghani, Pogue, & Leblond, 2012). Instead of measuring optical intensity like the CW-mode does, time-domain measurement has temporal resolution up to hundred picoseconds, which could result in the recovery of lifetime of fluorophore. Different from CW intensity measures, lifetime measures are immune to experimental and biological factors, such as laser power, probe uptake and concentration (Goergen, Chen, Bogdanov, Sosnovik, & Kumar, 2012). The benefits of time-domain have been proven by theoretical studies (Ducros, Da Silva, Hervé, Dinten, & Peyrin, 2009; Ducros, Hervé, Da Silva, Dinten, & Peyrin, 2009). One of the appealing features of time-domain schemes would be to reconstruct or separate fluorescence yield and the lifetime of endogenous fluorophores (Gao et al., 2010; Nothdurft et al., 2009). And the contrast to background of lifetime measures could even be enhanced when employing a fluorophore having a distinct lifetime from the auto-fluorescence (May, Bhaumik, Gambhir, Zhan, & Yazdanfar, 2009). A time-gated method was

used to record the arrival time of photons. So, depending on arrival time of selected photon, the depth of fluorescent object could be resolved (Q. Zhao, Spinelli, et al., 2011). Other studies demonstrated in simulation and experiments that using early arriving photons could reduce the scattering effect in the detection, thereby yielding significant improvements in the quality of fluorescence reconstructions (Niedre & Ntziachristos, 2010; B. Zhang et al., 2011; Q Zhu et al., 2011). Further studies using early arrival photons showed that multiple point-like fluorescent inclusions could be separated with millimeter spatial error; and both spatial resolution and image contrast were improved. These conclusions were verified by simulation and phantom experiment (Pichette, Domínguez, & Bérubé-Lauzière, 2013). Another advantage of time-domain technique is lifetime multiplexing due to the distinct lifetime decay profiles of different fluorophores. This technique was demonstrated both in phantoms and mice in vivo (J. Chen, Venugopal, & Intes, 2011; Scott B Raymond, Boas, Bacskai, & Kumar, 2010; Rice, Hou, & Kumar, 2013). Lifetime measurements could also be achieved by the frequency-domain modality, using the detected intensity and phase information (Chatni, Li, & Porterfield, 2009; DiBenedetto, Capelle, & O'Neill, 2012; Elder, Kaminski, & Frank, 2009; Y Lin et al., 2011a). However, either time-domain or frequency-domain suggests implementation complexity, long acquisition and relatively high cost. Strategies have been developed in order to preserve low cost, fast acquisition and good performance. Illumination strategies were developed aiming to shorten acquisition time while preserving informative datasets. Line excitation was compared with point or area illumination and phantom and animal experiments showed it as a feasible illumination scheme to potentially achieve quantitative recovery of fluorescence (L. Cao & Peter, 2013; D. Wang, Liu, & Bai, 2009). Wide-field excitation was adopted in time-domain fluorescence to reconstruct fluorescence lifetime with high throughput acquisition (Venugopal, Chen, & Intes, 2010; L. Zhao,

Abe, Barroso, & Intes, 2013). Low modulation frequency and LED illumination was used to achieve an alternative solution for FLI (Gioux, Lomnes, Choi, & Frangioni, 2010). In one example, a function generator was used to modulate a laser diode; thereby, the frequency-domain mechanism became cost efficient (B. Yuan, McClellan, Al-Mifgai, Growney, & Komolafe, 2009). In this sense, the CW-mode technique could be a good compromise between performance and cost (Patel et al., 2010). Further studies showed that early photons detection suffered from a low SNR due to the rejection of a great amount of emitted light; hence, first reconstructing with the quasi-CW data and then refining with early photons measurements were shown to yield a better resolution of fluorescence reconstruction image (Z. Li & Niedre, 2011). More recently, a spatial-frequency domain system was developed. In this technique, a low-cost projector was used to spatially modulate the CW excitation light for detecting both spatial frequency and intensity information. Demonstrated in a phantom study, illumination patterns with multiple spatial frequencies were projected on the surface of the imaging object; the depth recovery of fluorescent objects could be achieved by varying the spatial modulation frequency (Mazhar et al., 2010). Spatial-frequency fluorescence acquisition was conducted in tomographic mode with rotating view (Ducros et al., 2013). Both theoretical and experimental studies have been conducted to optimize illumination patterns to exploit the illumination flexibility as well as reduce computation burden (Dutta, Ahn, Joshi, & Leahy, 2010; Ducros et al., 2010; Ducros, D'Andrea, Bassi, Valentini, & Arridge, 2012). Arguably, using Cramer-Rao theoretical analysis, it was stated that the best depth precision of fluorescent object with FLI was not significantly better than the spatially modulated CW technique (Boffety, Allain, Sentenac, Massonneau, & Carminati, 2011).

Additionally, multi-spectral approaches have been explored to increase the measurement dimension in the wavelength domain. First, simulation work was conducted to validate the feasibility of employing multispectral excitation for a quantitative fluorescence reconstruction (Chaudhari et al., 2009). And it was reported that multispectral excitation might be able to separate different fluorophores having different concentrations (Pu et al., 2013). Using a tunable wavelength selection device, hyper-spectral excitation was achieved (Klose & Pöschinger, 2011).

The development of fluorescence imaging was also motivated by precision machining and fabrication. For example, investigators used (angular filter array) AFA to overcome the effect of scattering in macroscopic fluorescence imaging. By the AFA, only the emitted photons going through minimal scattering events would be collected; as a result, the retrieved fluorescence mapping could be enhanced to sub-millimeter resolution (Najiminaini et al., 2010; Vasefi et al., 2009; Vasefi, Belton, Kaminska, Chapman, & Carson, 2010). Separately, a handheld fluorescence imager probe consisting of micro-electromechanical systems (MEMS)-based scanning mirror was developed. And its ability for 3D fluorescence tomography was evaluated in in-vivo imaging of small animals (He et al., 2012). Moreover, another study reported that a micro-lensed dual-fiber optical probe would largely improve the detection efficiency of light, hence, result in a better SNR of measurement (H. Y. Choi et al., 2011).

Multi-modality fluorescence imaging

These state-of-the-art techniques have also been pursed to work in conjunction with complementary anatomical imaging modalities, such as MRI, X-ray CT, and US. The benefits of this combination are multiple and improvements significant. In one instance, photo-acoustic tomography (PAT) was combined with FMT, thus the high resolution of PAT and high sensitivity of FMT could be correlated to for a comprehensive pathological analysis (B. Wang,

Zhao, Barkey, Morse, & Jiang, 2012). A clinical study was conducted to reconstruct oxygen saturation and water content of joint tissues to separate osteoarthritic joints from healthy ones in the hand. In this study, the physiological parameters were recovered guided by the X-ray CT images (Z. Yuan, Zhang, Sobel, & Jiang, 2010). Likewise, a fluorescence probe coupled with transrectal US was used on a prostate phantom, and demonstrated its feasibility on guiding biopsies of tumors (Laidevant et al., 2011). Also, US images were used to provide anatomical prior information in white light excited fluorescence imaging; the recovered protoporphyrin IX (PpIX) mapping was capable of evaluating photodynamic therapy for human skin tumor (Flynn, DSouza, Kanick, Davis, & Pogue, 2013). A handheld fluorescence imager combined with an acoustic sensor was able to detect small fluorescent objects deep in a phantom, as well as determine imager orientation and phantom geometry (Erickson, Martinez, Gonzalez, Caldera, & Godavarty, 2010).

Several studies showed that the prior information recovered from anatomical images could improve the quality of reconstructions in terms of quantification and localization. X-ray images were used to provide prior information to determine optical properties for bioluminescence tomography (Naser & Patterson, 2010a). Similar work showed that X-ray CT images provided anatomical guidance for FMT; and the image accuracy was improved even when using limited projection scans for FMT (Radrich, Ale, Ermolayev, & Ntziachristos, 2012). Microcomputed tomography (MicroCT) was also employed to couple with single photon counting FMT for small animal imaging; and with CT image guidance, PpIX was accurately recovered from mouse phantoms (D. Kepshire et al., 2009). Beyond anatomical priors, other studies showed that PET functional priors, which were also specific to a lesion, could improve fluorescence reconstruction when using targeted molecular fluorescent probe (C. Li, Wang, Qi,

& Cherry, 2009). Likewise, optical properties could be reconstructed by CW DOT; subsequently, the simulation of photons propagation could be optimized for a better fluorescence reconstruction (Naser & Patterson, 2010).

Tri-modality imaging appears as a more sophisticated imaging strategy. Herein, a commercial microPET/CT was integrated with frequency-domain fluorescence imaging and employed with small animals to image fluorescent agent targeting on orthotopic growth of human prostate cancer (Darne et al., 2012). Also, the combination of MRI, DOT and FMT could provide anatomical and functional priori information for an improved fluorescence reconstruction. In this last study, MRI anatomy guided the recovery of optical properties of tissue. Then both the anatomical and functional information helped recover a fluorescent inclusion embedded 15 mm deep in rat with less than 5% quantification error (Yuting Lin, Ghijsen, Nalcioglu, & Gulsen, 2012). Another study demonstrated that with both X-ray CT anatomy and DOT functional information, fluorescence could be quantitatively recovered. An in vivo evaluation showed quantification errors as low as 2% (Yuting Lin et al., 2010b).

Reconstruction, data extraction and calibration

As FMT process involves model-based reconstruction, the developments of forward modeling and the inverse problem are critical in this diffuse light imaging technique. The forward modeling is the process describing photons propagation in tissue and linking the variation of optical/fluorescent properties of tissue to individual sources or detectors. Monte Carlo (MC) is one of the most commonly used methods to simulate photons propagation. A MC program was presented in 1995, to simulate photons traveling in tissue with multi-layer structure. High agreement was reached with analytical diffusion models (L. Wang, Jacques, & Zheng, 1995). Following, the tMCimg algorithm was proposed to simulate photons in tissues having

complex 3D geometry (Boas, Culver, Stott, & Dunn, 2002). More recently, meshed based MC was developed, which displayed an accuracy comparable to analytical diffuse models for targets with curved boundaries (Fang, 2010). A direct MC algorithm was also reported that stored photons traveling paths and then showed that fit between fluorescent properties and tissue absorptions could be completed rapidly (Kumar, 2012). In addition to MC, radiative transfer equation (RTE) derived forward modeling was also broadly employed in fluorescence reconstruction. Several studies showed its accuracy and agreement with MC (Liemert & Kienle, 2012; Montejo, Klose, & Hielscher, 2010). To simplify the RTE in terms of complexity and computation time, the diffusion equation has also been commonly used. DE is the first order angular approximation to the RTE under an approximation that $\mu_s' >> \mu_a$, which is true when light travels a few millimeters in tissue but less accurate close to boundaries. In one study, an additive correction was added to the DE; and substantial improvements were shown in comparison to standard DE (Lehtikangas, Tarvainen, & Kim, 2012). Another way to improve the DE was to combine both RTE and DE. Specifically, DE was replaced with RTE in the spatial regions where the modeling accuracy increased (Gorpas & Andersson-Engels, 2012). Other high-order approximations of RTE were also explored and the improvement of modeling precision was observed comparing with the standard DE (Lu et al., 2010).

The inverse problem aims to retrieve the fluorescence properties, given the weight matrix found by the forward modeling and the experimental measurements. Since inversion involves taking the inverse of the weight matrix, the inverse computation is unavoidably ill-posed, thus is commonly resolved iteratively. Tikhonov Regularization (TR) is regarded as one of commonly used techniques in fluorescence reconstruction (Arridge & Schotland, 2009). Specifically in multi-modality fluorescence imaging, anatomical prior information can be coupled into the

objective function as a penalty term to constrain the optimization process (Yalavarthy, Pogue, Dehghani, & Paulsen, 2007). In addition to the L2 norm that is often used to integrate the prior in TR, other methods have been investigated to better utilize the prior for fluorescence reconstruction. The L1 norm was suggested as a penalty term to regularize the reconstruction, and it was shown that it gave sparse solutions and could avoid the over-smoothing effects particularly when solving sparsely localized small fluorescent objects (Basevi et al., 2012; Chamorro-Servent et al., 2013; Kavuri, Lin, Tian, & Liu, 2012; Q. Zhang, Chen, Qu, Liang, & Tian, 2012). A total variation regularization was proposed showing its advantages over the L2 norm of avoiding over-smoothness and enhancing the spatial resolution of fluorescent object in the reconstruction fluorescence images (J F P-J Abascal et al., 2011; Behrooz, Zhou, Eftekhar, & Adibi, 2012; Freiberger, Clason, & Scharfetter, 2010). A joint L1-total variation norm was seen to have the advantages of preserving the edge and the local smoothness (Dutta, Ahn, Li, Cherry, & Leahy, 2012). In all these techniques, the regularization parameter is also a subtle but important point to adjust the strength of the penalty term. Here, a L-curve method was often used, with which the regularization parameter would be determined at the corner of the log-log plot of the regularized solution and the norm of the corresponding residual (Hansen & O'Leary, 1993). Also, it was demonstrated that a U-curve method could be used to select the regularization parameter in the reconstruction of DFI (Chamorro-Servent, Aguirre, Ripoll, Vaquero, & Desco, 2011). Instead of these automatic methods, an optimal value of regularization parameter was often determined empirically (Yalavarthy, Pogue, Dehghani, & Paulsen, 2007).

Given a well-developed reconstruction algorithm, data of good quality is expected to bring good results. In this sense, data calibration can be used to cancel off experimental factors, or somehow bypass the difficulties in the forward model. Here, (Born-normalization) BN has

been widely applied in fluorescence imaging, by which the ratio between fluorescent signal and intrinsic light signal is taken as input for the reconstruction. With this approach, experimental factors, such as laser power and coupling loss can be cancelled (Ntziachristos & Weissleder, 2001). In another study, a workflow of calibration steps was elaborated for a CT-guided FMT system. The phantom results indicated the importance of careful calibration (Tichauer et al., 2011). When guided by anatomical image, the sampling of problematic data could be reduced; thus the fidelity of reconstruction was improved (X. Zhang et al., 2011). Also, work was done to reduce the image artifact due to tissue heterogeneity. In one study, fluorescence from the targeted lesion was corrected by an excitation image to reduce the artifact induced by the spurious fluorescent signal because of the parts of tissue that was thin or had low-absorption (Mohajerani, Adibi, Kempner, & Yared, 2009). Fidelity of measurements can also be enhanced experimentally. In one study, specific fluorescence signal was subtracted from an unbounded surrogate. This dual-tracer approach reduced the background signal originated from the bounded probe; thereby demonstrating substantial improvement in image contrast (Tichauer et al., 2013). Furthermore, good acquisition means having of a high SNR. In this endeavor, automatic control of imaging exposure time helps avoid saturation for the thin tissues, and enable high signal amplitude for the absorbing portions, ultimately to ensure linearity of measurement (D. L. Kepshire, Dehghani, Leblond, & Pogue, 2009). In fluorescence imaging, excitation light leakage contaminates the fluorescence signal. To overcome this, the combination between appropriate filter and collimation optics could efficiently reject excitation light thus potentially improve the detection sensitivity of fluorescence (B. Zhu, Rasmussen, Lu, & Sevick-Muraca, 2010).

Methods have been investigated to speed up the computation for both forward modeling and inverse problem. For instance, a coupled Boundary element method (BEM)-finite element

method (FEM) computational approach simplified the nodes for outer tissue but kept the complexity for the internal ones. And the computational speed using this approach was shown to be faster than the standalone FEM (Srinivasan, Ghadyani, Pogue, & Paulsen, 2010). The size of the forward model matrix could be compressed by wavelet methods whilst preserving the significant information (Correia, Rudge, Koch, Ntziachristos, & Arridge, 2013; Ducros et al., 2011). In a separate study, the wavelet method was applied to reduce model dimension in order to speed up the computation (Landragin-Frassati, Dinten, Georges, & Da Silva, 2009). Principal component analysis (PCA) methods were also used to reduce measurement redundancy for a fast and informative reconstruction (X. Cao et al., 2013; Mohajerani & Ntziachristos, 2013). Along the same line, a fast reconstruction was achieved by an iterated shrinkage based reconstruction method with sparsity regularization, showing accurate results with limited measurement data (Han et al., 2010).

Fast computations could also be achieved by advanced programming techniques. A matrix-free technique was developed using a Matlab function, called 'gmres', to optimize the objective function, in which the creation and storage of big Jacobian matrices were avoided, thus computation burden reduced (Zacharopoulos et al., 2009). Different studies demonstrated that the graphics processing unit (GPU) based parallel computing could largely shorten the computation in a MC based forward modeling (Fang & Boas, 2009), as well as for both forward modeling and inverse problem in a DE based scheme (Freiberger, Egger, Liebmann, & Scharfetter, 2011).

1.3 Organization of the thesis by objectives

Three objectives were set in this thesis and each is associated with different hypotheses.

Objective #1: To develop a low-cost multi-modality imaging system combining CW transmission fluorescence imager and home-made single-element-transducer US system. Proof-of-concept study was conducted to characterize the system and assess its feasibility for in-vivo animal imaging.

- Hypothesis #1-1: The fluorescent and structural information recorded from the fluorescence-US system could benefit the extraction of fluorescent functional information.
- Hypothesis #1-2: This low-cost combined system could potentially provide an imaging strategy for in-vivo study with mice.

The article that addressed this objective is:

Baoqiang Li, Maxime Abran, Carl Matteau-Pelletier, Léonie Rouleau, Tina Lam, Rishi Sharma, Eric Rhéaume, Ashok Kakkar, Jean-Claude Tardif and Frédéric Lesage, "Low-cost three-dimensional imaging system combining fluorescence and ultrasound," J. Biomed. Opt. 16, 126010 (Dec 06, 2011).

Objective #2: The second objective was to improve the fluorescence-US system in terms of sampling precision and reconstruction mechanism. The system would further be validated using in-vivo molecular imaging with tumorous murine model.

- Hypothesis #2-1: An electron multiplying charge coupled device (EMCCD) camera detection will enrich the recording of fluorescent emission. The US subsystem and the profilometer will provide accurate structural information of the imaging sample.
- Hypothesis #2-2: This fluorescence-US system can serve as a potent tool for preclinical tumorous imaging study with mice.

The article that addressed this objective is:

Baoqiang Li, Romain Berti, Maxime Abran and Frederic Lesage, "Ultrasound guided fluorescence molecular tomography with improved quantification by an attenuation compensated born-normalization and in vivo preclinical study of cancer," Rev. Sci. Instrum., vol. 85, no. 5, p. 053703 (May 2014).

Objective #3: Develop a MRI-guided FMT system for atherosclerotic imaging with mice.

- Hypothesis #3-1: MRI anatomy can help optimize the forward modeling for 3D fluorescence reconstruction.
- Hypothesis #3-2: This multi-modality imaging approach can achieve quantitative fluorescence reconstruction for atherosclerotic studies with mice.

The article that addressed this objective is:

Baoqiang Li, Foued Maafi, Romain Berti, Philippe Pouliot, Eric Rhéaume, Jean-Claude Tardif, and Frederic Lesage, "Hybrid FMT-MRI applied to in vivo atherosclerosis imaging," Biomed. Opt. Express 5, 1664-1676 (2014).

The thesis is planned as follows: In the second chapter, the basic theory of diffuse fluorescence imaging is described, which includes the concepts of forward modeling, inverse problem, as well as how to reconstruct fluorescence targets from boundary measurement (BM). From the third chapter to the fifth chapter, three published papers are presented addressing the objectives above. In these three chapters, DFI was first incorporated with US imaging, and then MRI. The benefits of these anatomical modalities were evaluated by simulation, phantoms and mice experiments *in vivo*. In the sixth chapter, a discussion of the advantages as well as limitations of the proposed multi-modality imaging approaches is discussed. Finally, the thesis is concluded in the seventh chapter.

CHAPTER 2 THEORY OF DIFFUSE FLUORESCENCE IMAGING

The theory behind Diffuse Fluorescence Imaging (DFI) consists of forward modeling and solving the inverse problem (Arridge & Schotland, 2009; L. V. Wang & Wu, 2007). The former predicts how the photons propagate through tissue with known optical properties of tissue, source/detector positions, as well as power and direction of illumination. The outcome of the forward modeling is a weight matrix. The latter is then used to reconstruct the fluorescent/optical properties from BM based on this same weight matrix which may be iteratively modified during this process. When linearizing the system, a simplified description of fluorescence reconstruction can be modeled by:

$$Y = AX \tag{2.1}$$

where Y represents the experimental measurements; X is the fluorescent properties to be reconstructed; A is weight matrix. Having the measurement, X could be reconstructed by inversing the weight matrix A:

$$X = A^{-1}Y \tag{2.2}$$

The inverse of the matrix A is often ill-posed and computationally demanding to compute. Hence, sophisticated method has been developed to reduce the ill-posedness of the inverse problem.

Furthermore, for accuracy, the forward modeling needs an accurate geometrical definition of the problem domain. This requirement motivates the incorporation with supplemental anatomical imaging modality. As an added bonus, the anatomical images can also be used to regularize the fluorescence reconstruction.

2.1 Forward modeling

Several methods exist to simulate the photons propagation in biological tissue. MC methods stochastically model a photon trajectory as random walk (L. Wang et al., 1995; Fang &

Boas, 2009; Boas et al., 2002). The eventual evaluation of a given process is estimated with averaging multiple independent photons. The RTE method models photons transport analytically (Gorpas & Andersson-Engels, 2012). Because of its complexity, it is often simplified to the DE under the approximation of $\mu_s' >> \mu_a$. The DE method is less accurate in comparison to MC and RTE, but computationally efficient, therefore, has been widely adopted in simulating photons propagation.

In this subchapter, the forward modeling will be strictly based on the DE in the CW mode. Nonetheless, the concepts, such as Green function, weight matrix can be translated to other modeling methods. Please refer to other materials (Arridge & Schotland, 2009; Dehghani et al., 2009; Markel et al., 2003; L. V. Wang & Wu, 2007) for a detailed equation derivation and comprehensive understanding of forward modeling.

The fluorescent photons propagation in diffusive medium can be described by the following coupled diffusion equations. Under the principle of red-shift (L. V. Wang & Wu, 2007), the fluorophore embedded in medium absorbs photons at the wavelength of λ_x; and then emits fluorescence at wavelengths greater than λ_x, λ_m. Because optical properties (μ_s' and μ_a) are wavelength dependent, the photon propagation in medium is described by the following two equations:

$$-\nabla \cdot D_x(r)\nabla U_x(r,\omega)c + [c\mu_{ax}(r) + i\omega]U_x(r,\omega) = q(r,\omega) \tag{2.3}$$

$$-\nabla \cdot D_m(r)\nabla U_m(r,\omega) + [\mu_{am}(r) + \frac{i\omega}{c}]U_m(r,\omega) = \eta(r)\mu_{fl}(r)U_x(r,\omega)\frac{1 - i\omega\tau(r)}{1 + [\omega\tau(r)]^2} \tag{2.4}$$

where the subscripts x and m represent excitation wavelength and emission wavelength, respectively; r is a random position in the imaging medium Ω; ω is modulation frequency, which equals to zero in the CW mode. The term $U(r,\omega)$ represents the photon density; $\mu_a(r)$ is the

optical absorption coefficient; $D(r) = \frac{1}{3(\mu_a(r) + \mu_s'(r))}$ is the diffusion coefficient with $\mu_s'(r)$ representing the reduced scattering coefficient; τ and η are the lifetime and quantum yield of fluorophore, respectively; $\mu_{fl}(r)$ is the absorption coefficient of fluorophore; $q(r,\omega)$ is the photons density source strength; c is velocity of light in the medium. The first equation describes the propagation of photons at the excitation wavelength in the medium. In turn, the second one describes the propagation of photons at the fluorescent emission wavelength in the medium. For each source-detector pair, the coupled partial differential equations can be solved by the Green's function method. Without giving the detailed equations derivation, the photon density $U_x(r,\omega)$ of the equation (2.3) is incorporated into the equation (2.4) as a part of the source term. Thus, $U_m(r,\omega)$ can be solved from the equation (2.4) as:

$$U_m(r_s, r_d) = K\int_\Omega G_x(r_s, r)A(r)G_m(r, r_d)d^3r \tag{2.5}$$

where $A(r)$ is the fluorescent yield, which can be represented as $A = \eta\mu_{fl}$; here, $\mu_{fl} = \varepsilon C$; and ε, C are the quantum yield and concentration of fluorophore, respectively; G_x is the Green's function describing photons propagation at the excitation wavelength from the source position r_s to a random position r in Ω. Likewise, G_m is the Green's function describing photons propagation at the emission wavelength from r to the source position r_s in Ω. The parameter K represents experimental factors, such as source power, camera gain and coupling loss.

Previous studies demonstrated that using a so-called BN could result in a quantitative measuring. Here, the BN is a ratio that dividing the fluorescence emission light by the intrinsic absorption light to diminish the experimental effects such as source intensity, detector gain and

coupling efficiency (Ntziachristos & Weissleder, 2001; Vinegoni, Razansky, Figueiredo, Nahrendorf, et al., 2009). In this formulation, this normalization scheme is directly given by:

$$U_B(r_s, r_d) = \frac{U_m(r_s, r_d)}{U_x(r_s, r_d)} = \frac{\alpha}{G_x(r_s, r_d)} \int_\Omega G_x(r_s, r) A(r) G_m(r, r_d) d^3 r \tag{2.6}$$

where U_B is the born normalization field; the constant α is a calibration factor re-scaling the fluorescence amplitude which could be experimentally determined by measuring fluorophores of known concentration (Frederic Leblond et al., 2009; Soubret, Ripoll, & Ntziachristos, 2005; Vinegoni, Razansky, Figueiredo, Nahrendorf, et al., 2009). From the equation (2.6), a sensitivity matrix $S(r_s, r_d)$ is obtained for each source-detector pair, as follows:

$$S(r_s, r_d) = \frac{1}{G_x(r_s, r_d)} \int_\Omega G_x(r_s, r) G_m(r, r_d) d^3 r \tag{2.7}$$

with the matrix $S(r_s, r_d)$ describing photons propagation between the source position of r_s and the detector position r_d. In experiments, measurement with multiple source-detector pairs will be acquired. For notation, the sensitivity matrix for the *i*th measurement is presented as S_i with each measurement corresponding to one source-detector pair. So, for total N measurements, the weight matrix W is built as:

$$W_{N \times M} = [S_1, S_2, \cdots, S_i, \cdots, S_N]^T \tag{2.8}$$

where M is number of element of the sensitivity matrix S.

As shown, the coupled DEs are solved to first have the Green function $G_{x,m}$ for either a source or a detector; and ultimately form the weight matrix W. Likewise, $G_{x,m}$ could also be computed by MC and RTE; and same process would be applied to finally generate W.

2.2 Inverse problem

In experiments, the optical signal of both the excitation wavelength and the emission wavelength are typically recorded. As reported, this enables to perform a BN ratio which will cancel off experimental factors, such as detector gain, detection exposing time, power of incident light and coupling loss. Instead of the direct fluorescent measurement, using the BN ratio is expected to enhance the quantification of the reconstruction (Ntziachristos & Weissleder, 2001).

In practice, the BN ratio M_B is calculated by dividing the measurement at the fluorescence emission wavelength M_m by the measurement at the excitation wavelength M_x, both at the same detector position r_d :

$$M_B = \frac{M_m}{M_x} \tag{2.9}$$

However, imperfect filtering might induce signal contamination by allowing $\theta_{leaking}$ percent of the excitation signal leaking into the fluorescence channel. In such case, the BN ratio can be corrected by:

$$M_B = \frac{M_m - \theta_{leaking} M_x}{M_x} \tag{2.10}$$

with the value of $\theta_{leaking}$ estimated experimentally by measuring a sample without fluorescent inclusion, given by:

$$\theta_{leaking} = \frac{M_m^{'}}{M_x^{'}} \tag{2.11}$$

where, $M_m^{'}$ and $M_x^{'}$ are the optical measurements recorded at the fluorescence emission channel and the excitation filter channel, respectively.

The reconstruction is started by minimizing the following objection function (Davis et al., 2007a; Dehghani et al., 2009; Yalavarthy, Pogue, Dehghani, & Paulsen, 2007; Yalavarthy, Pogue, Dehghani, Carpenter, et al., 2007):

$$\Omega = \left\| \Phi^{meas} - W\chi \right\|^2 + \lambda \left\| L\chi \right\|^2 \tag{2.12}$$

Taking the first-order condition, $\frac{\partial \Omega}{\partial \chi} = 0$, leads to the following iterative minimization process:

$$\chi_{i+1} = [W^T W + \lambda L^T L]^{-1} W^T (\Phi_i^{meas} - \Phi_i^C) + \chi_i \tag{2.13}$$

Here, Φ^{meas} and Φ^C are the experimental and simulated Born ratios; W is the weight matrix; χ represents the fluorescence yield εηC, in which ε, η and C are the extinction coefficient, quantum yield and concentration of the fluorophore, respectively. The matrix L encodes the prior localization of fluorescence emission in the Laplacian form (Yalavarthy, Pogue, Dehghani, & Paulsen, 2007); it is used to constrain reconstruction as a soft-prior. λ is the regularization parameter to adjust the strength of the penalty term. Finally, reconstruction it typically performed iteratively, and i represents the iteration index. Convergence is considered achieved when the projection error between two iterations is below 1%. However, a maximum of eight iterations it typically imposed to avoid the estimated error increasing (Yalavarthy, Pogue, Dehghani, & Paulsen, 2007).

2.3 Prior guided fluorescence reconstruction

The anatomical image can benefit both the forward modeling and the inverse problem. As discussed in the literature review in the previous chapter, separating different tissue types or organs in the anatomical images can allow specifically assigning the known optical properties to each tissue type or organ. With the proper assignment of the optical properties (Alexandrakis, Rannou, & Chatziioannou, 2005; S. A. Prahl, n.d.), the photon propagation in tissue can be more

precisely simulated; thus a more accurate weight matrix W would be expected for a better reconstruction. On the other hand, the structural prior derived from anatomical images can also be used to construct matrix L in equation (2.13) to constrain the reconstruction in a Laplacian form(Davis et al., 2007a; Yalavarthy, Pogue, Dehghani, & Paulsen, 2007). The mathematical form of L that is typically used is indicated below:

$$L_{ij} = \begin{cases} 0 & \text{if i and j are not in the same region} \\ -1/N & \text{if i and j are in the same region} \\ 1 & \text{if i=j} \end{cases} \quad (2.14)$$

Here, N represents the number of nodes. The anatomical image can also be co-registered with fluorescent functional images to provide a comprehensive interpretation; therefore, providing a valuable supplement to fluorescence imaging.

CHAPTER 3 ARTICLE #1: LOW-COST THREE-DIMENSIONAL IMAGING SYSTEM COMBINING FLUORESCENCE AND ULTRASOUND

Baoqiang Li[1,2], Maxime Abran[1,2], Carl Matteau-Pelletier[1,2], Léonie Rouleau[1,2,3], Tina Lam[4], Rishi Sharma[4], Eric Rhéaume[2], Ashok Kakkar[4], Jean-Claude Tardif[2], Frédéric Lesage[1,2]

[1]Institute of Biomedical Engineering, École Polytechnique de Montréal, Montreal, Canada.

[2]Montreal Heart Institute, Montreal, Canada

[3]Génie Chimique et Biotechnologique, Université de Sherbrooke, Sherbrooke, Canada

[4]Chemistry Department, McGill University, Montreal, Canada

3.1 Presentation of the article

This article (B. Li, et al., 2011) aimed to address the first objective of this thesis. In this work, we developed a low-cost fluorescence-US imaging system. Characterized by phantoms, it was shown that the supplemental US information could improve the fluorescence reconstruction. Also, proof-of-concept experiment with mice demonstrated its feasibility for future in vivo study. This article was published in *Journal of Biomedical Optics*.

3.2 Abstract

In this paper, we present a dual-modality imaging system combining 3D CW trans-illumination fluorescence tomography with 3D US imaging. We validated the system with two phantoms, one containing fluorescent inclusions (Cy5.5) at different depths, and another varying-thickness semi-cylindrical phantom. Using raster scanning, the combined fluorescence/US system was used to collect the boundary fluorescent emission in the X-Y plane, as well as recovered the 3D

surface and position of the inclusions from US signals. US images were segmented to provide soft a prior for the fluorescence image reconstruction. Phantom results demonstrated that with priors derived from the US images, the fluorescent reconstruction quality was significantly improved. As further evaluation, we show pilot in-vivo results using an Apo-E mouse to assess the feasibility and performance of this system in animal studies. Limitations and potential to be used in atherosclerosis studies are then discussed.

3.2.1 Key words

Fluorescence, US, reconstruction, imaging, tomography, prior information, atherosclerosis

3.3 Introduction

Diffuse optical fluorescence tomography has gradually been applied in biological research and pharmaceutical industry as it has the potential to lift topographic fluorescence techniques to a quantitative method for imaging molecular and cellular activity using specific fluorescent agents (Gibson et al., 2005; Frederic Leblond et al., 2010; Soubret et al., 2005). However, while multiple demonstrations of image reconstruction have been published, quantification of fluorescence signals in 3D remains a challenge. Instrumentation for fluorescence imaging comes in different flavours with camera based broad beam imaging being the most common configuration (Frederic Leblond et al., 2010). Pogue BW et al found that raster-scanned point sampling system had advantages over broad beam CCD camera system towards accurate quantification of fluorescence signals (Pogue, Gibbs, Chen, & Savellano, 2004). Epi-illumination, which illuminates objects and collects emission on the same side, is severely limited with respect to quantification when probing deep objects in tissue (a few millimetres) due to light absorption and scattering (Frederic Leblond et al., 2010). It is also subject to the non-specific signal contamination such as auto-fluorescence originating from the surface in small animals. Recent

work demonstrated that a camera based epi-illumination system could possibly resolve reflected GFP-like fluorescence signals from depth up to 10 mm in a phantom of optical properties μa=0.1 mm-1 and μs'=1 mm^{-1} (Björn, Ntziachristos, & Schulz, 2010). But the quality of the image deteriorated severely as the depth increased and the absorption coefficient used was not coherent with measured in vivo values for the wavelength employed in this study. However, in transmission mode, a collimated laser beam with large energy deposition, but still under the safety limits, can traverse several centimetres into the tissue (D'Andrea, Spinelli, Comelli, Valentini, & Cubeddu, 2005; Gibson et al., 2005; Graves, Ripoll, Weissleder, & Ntziachristos, 2003; Kumar, Raymond, Dunn, Bacskai, & Boas, 2008; Leavesley, Jiang, Patsekin, Rajwa, & Robinson, 2008; Frederic Leblond et al., 2010; Montet et al., 2007; Ntziachristos & Weissleder, 2002; Patwardhan, Bloch, Achilefu, & Culver, 2005; Zavattini et al., 2006a).

Besides imaging geometries, recent improvements in diffuse fluorescence imaging were made by incorporating structural information into the model-based reconstructions (Ale et al., 2010; Brooksby, Dehghani, Pogue, & Paulsen, 2003; Davis et al., 2007a, 2008; Fang, Moore, Kopans, & Boas, 2010; Guven, Yazici, Intes, & Chance, 2005; Intes, Maloux, Guven, Yazici, & Chance, 2004; D. Kepshire et al., 2009; Y Lin et al., 2011a; Y Lin, Gao, Nalcioglu, & Gulsen, 2007; Yuting Lin et al., 2010a; Schulz et al., 2009; Tan & Jiang, 2008; Yalavarthy, Pogue, Dehghani, & Paulsen, 2007; Yalavarthy, Pogue, Dehghani, Carpenter, et al., 2007). For example, Fang et al used a composition-based image segmentation method to combine X-ray structural priors into DOT for breast imaging (Fang et al., 2010). Kepshire et al reported a study, which combined X-ray microCT with fluorescence and assessed performance using protoporphyrin IX phantoms (D. Kepshire et al., 2009). The benefits to fluorescence imaging from X-ray priors were also demonstrated in several other studies (Ale et al., 2010; Yuting Lin et al., 2010a; Schulz

et al., 2009). Using the same modality, Y. Tan et al employed DOT, which might be easily integrated in the fluorescence imager, to provide functional priors for fluorescence reconstruction (Tan & Jiang, 2008). Structural priors from MRI have also been investigated for guiding DOT or fluorescence reconstructions (Brooksby et al., 2003; Davis et al., 2008; Y Lin et al., 2011a). Hence, structural information measured from the variety of imaging modalities mentioned above provide prior information that can be incorporated by a regularization method for image reconstruction (Davis et al., 2007a; Yalavarthy, Pogue, Dehghani, & Paulsen, 2007; Yalavarthy, Pogue, Dehghani, Carpenter, et al., 2007). Outcomes from these works confirmed that prior anatomical information benefited the fluorescence image reconstructions. However, these techniques require instruments associated with large cost and infrastructure. Moreover, they either necessitate custom integration of optical imaging in the MRI/CT imaging chambers, usually leading to lower optical sampling or require a multimodal 'animal bed' leading to serial instead of simultaneous imaging. Methods and systems that integrate anatomical information while keeping the lower cost advantages of fluorescence imaging would thus be beneficial.

In this endeavour, a few studies showcased the feasibility to employ US as a complement to fluorescence imaging. C. Snyder et al employed fluorescence imaging and 2D US imaging to assess tumour size in mice (Snyder et al., 2009). They used both imaging modalities separately and confirmed co-registered tumour detections but did not combine the information. Zhu et al used two orthogonal US slices to estimate tumour diameter and center (Quing Zhu et al., 2003). The estimated size was then employed to segment the tissue into lesion and background regions aiming to provide a priori knowledge in diffuse optical reconstruction. Zhu et al have used a phantom imaged using both US and optical absorption to investigate the improvement in image reconstruction in reflection geometry; but recovering small targets in this configuration might be

a challenge because of the distance (~4mm) between each element of the US detector array used as higher horizontal resolution may be needed, especially for recovering a non-regular object surface (Q. Zhu, Durduran, Ntziachristos, Holboke, & Yodh, 1999). In addition to guiding fluorescence imaging, other studies demonstrated that US images help in the estimations of the optical properties. For example, it was demonstrated that the geometrical constraints derived from US signals might provide improvement in computing the optical properties of DOT (Holboke et al., 2000). A recent study showed the recovery of the lesion tissue value by imaging protoporphyrin IX production in skin tumour and demonstrated that the fluorescence emission can be better quantified when using priors obtained by segmenting US image into tissue layers (Gruber et al., 2010a).

Distinct from the above studies (Gruber et al., 2010a; Holboke et al., 2000; Snyder et al., 2009; Q. Zhu et al., 1999; Quing Zhu et al., 2003), we built a low-cost system combining fluorescence tomography with US imaging in an attempt to explore 3D images from these two modalities. Instead of combining both modalities in reflection (Q. Zhu et al., 1999), our fluorescence configuration is in trans-illumination, thereby using the documented quantification benefits of this geometry. A raster-scanned 3D imaging was achieved in both modalities controlled by two motors, providing a simple and low-cost system design using a single US and fluorescence detector. To evaluate the performance of this simple system, we conducted phantoms and animal studies. We segmented 3D US images into background and fluorescence emission regions to provide an accurate structural prior to fluorescence reconstruction. Fluorescence tomography with US priors was facilitated by the co-registered scans. US imaging could also help investigator interpret functional images.

We characterized the system with phantoms in order to provide answers to whether US can be used to provide informative priors to fluorescence tomography. We also evaluated the feasibility and potential of this system to be used in animal study with an Apo-E mouse (Nakashima, Plump, Raines, Breslow, & Ross, 1994). Our results show that while US images are difficult to segment and provide limited structural information, their benefits to fluorescence reconstruction are still significant. As a result, this low cost (less than 9k$) multimodal fluorescence/US system may provide an interesting avenue towards quantitative molecular imaging.

3.4 Methodology

3.4.1 System design

A schematic of the system is shown in Figure 3.1. A laser diode (658nm, HL6512MG, Thorlabs) was used to generate a collimated laser beam illuminating from the bottom of the object. Laser light was further filtered by an optical band-pass filter D650/20 (Chroma Technology). On the opposite side, the emitted photons were detected with an optical fibre used to guide light towards a set of optical filters (Chroma Technology) mounted in a filter wheel (FW103/M, Thorlabs) thus enabling multi-spectral detection. Filtered photons were collected by a photomultiplier tube (PMT) (H5783-20, Hamamastu). To eliminate residual ambient light, the laser diode was modulated with a square wave at 1 KHz (software adjustable) and demodulated on detection. For US recordings, the system employed a single element transducer (5 MHz, ⌀0.5'', F=10cm, Olympus). The electronics were built to support transducers with frequencies between 2.25MHz and 30MHz. The laser and transducer scanned over the region of interest (ROI) point by point in the X-Y direction using a translation stage controlled by two actuators (L12-100-100-12-I, Firgelli Technologies) in 1mm steps (positional accuracy: ± 0.3 mm). A home-made electronic

circuit controlled the laser diode, derived the transducer, controlled the two actuators, sampled and pre-processed optical and ultrasonic signals. The received datasets were then sent to a computer through a USB link for post-processing. In addition, a monochrome CMOS camera (DCC1545M, Thorlabs) was used to capture a snapshot to select the scan area. By correlating the pixel index of snapshot to the positions of both actuators, the ROI for each scan was calibrated. For each point, fluorescence signals were sampled at a frequency of 200KHz and with an integration time for demodulation of typically 200ms (software adjustable). For US imaging, each point was sampled at 125MHz, and typically averaged 1000 times (software adjustable). In order to couple ultrasonic pulse-echoes in the experiments, the object was placed under a water bath separating water from the object with a plastic membrane to conduct both fluorescence and US imaging.

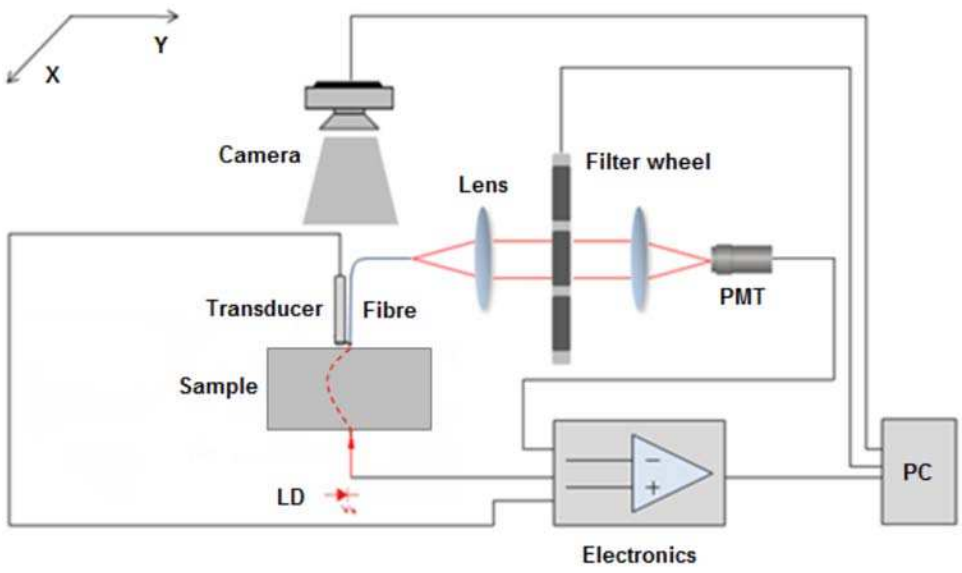

Figure 3.1: Schematic of this dual-modality imaging system.

3.4.2 Reconstruction

A coupled diffusion model was used to simulate fluorescence propagation in a diffusive media (Milstein et al., 2004). The propagation of excitation light is modeled by (3.1); the transport of excited fluorescence by (3.2).

$$\nabla \cdot [D_x(r)\nabla \phi_x(r,\omega)] - [\mu_{ax}(r) + \frac{j\omega}{c}]\phi_x(r,\omega) = -\delta(r - r_{sk}) \tag{3.1}$$

$$\nabla \cdot [D_m(r)\nabla \phi_m(r,\omega)] - [\mu_{am}(r) + \frac{j\omega}{c}]\phi_m(r,\omega) = -\phi_x(r,\omega)\eta\mu_{fl}(r)\frac{1 - j\omega\tau(r)}{1 + [\omega\tau(r)]^2} \tag{3.2}$$

where λ_x and λ_m denote the excitation and emission wavelength, ϕ is the photon flux (W/m^2), D is the diffusion coefficient, μ_a is the absorption coefficient. Quantum efficiency, absorption coefficient and lifetime of fluorophore are represented by η, μ_{fl} and τ respectively and c is the velocity of light in the medium (Milstein et al., 2004).

We employed the software package-NIRFAST to model photon propagation using a FEM for the forward model and to perform reconstructions (Dehghani et al., 2009). The inverse model was performed with the following Tikhonov minimization function equation (Yalavarthy, Pogue, Dehghani, & Paulsen, 2007).

$$\sigma^2 = \left\{ \sum_{i=1}^{NM} (\Phi_i^{Meas} - \Phi_i^C)^2 + \lambda \sum_{j=1}^{NN} (\chi_j - \chi_0)^2 \right\} \tag{3.3}$$

Where the measured and simulated boundary fluence are represented by Φ^{Meas} and Φ^C, respectively, NM is the total number of measurements, NN is the number of FEM node, λ is the Tikhonov regularization parameter, χ_0 is the initial guess of the fluorescence parameter, $\eta\mu_{af}$ in our case, and χ_j is the parameter to be updated (Yalavarthy, Pogue, Dehghani, & Paulsen, 2007).

Using equation (3.3) and applying a Levenberg Marquardt (LM) procedure, the update step is performed by (Yalavarthy, Pogue, Dehghani, & Paulsen, 2007):

$$\Delta\chi = [J^T J + \lambda I]^{-1} J^T (\Phi^{Meas} - \Phi^C) \tag{3.4}$$

with $\Delta\chi = \chi_j - \chi_0$. J is the Jacobian matrix which defines the relationship between the simulated boundary data and fluorescence parameter and I is the identity matrix (Yalavarthy, Pogue, Dehghani, & Paulsen, 2007).

3.4.3 Phantoms

To validate the system we employed two phantoms having different geometries and optical properties. As shown in Figure 3.2 (a), the first one had a rectangular parallelepiped shape and dimension of 100mm×30mm×20mm (provided by ART Inc). To model heterogeneous absorption, it included four inclusions with different optical properties, denoted by Diff 1-4 (see Table 3.1 for optical properties). As illustrated in Figure 3.2 (b) and (c), two holes were drilled along y direction and fluorescent tubes were inserted, denoted by Fluo 1 and 2. The second phantom (Figure 3.2(d)) had a semi-cylindrical geometry of 19-mm radius and 105-mm length and was homogeneous. It was used to assess performance in non-regular geometries. A fluorescent tube was inserted in the phantom perpendicular to the curved surface to model non-uniform fluorophore depths. Detailed design information on the two phantoms is provided in Table 3.1.

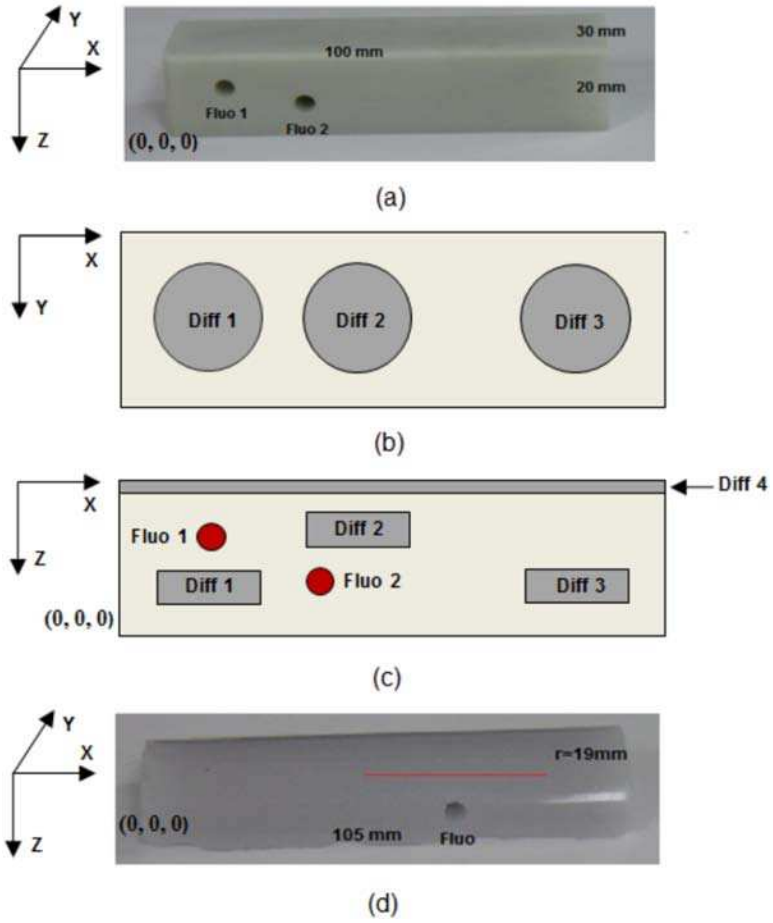

Figure 3.2: (a) Dimension of the rectangular phantom: phantom 1. (b)-(c) Schematic depiction showing the four heterogeneities (denoted by diff 1-4) and two holes for inserting fluorescent tubes (denoted by fluo 1-2). (d) Dimension of the semi-cylindrical phantom, phantom 2.

For experimental data, the fluorochrome used was Cy5.5 with an absorption peak at 675nm and emission peak at 694nm.

Table 3.1: Optical properties for both phantoms. Phantom 1 and 2 represent the rectangular phantom and semi-cylindrical phantom, respectively.

	Inclusion	Center position (mm)			Dimension (mm)				Optical properties (mm^{-1})	
		X	Y	Z	Diameter	X	Y	Z	μ_a	μ_s'
Phantom 1	**Bulk**	--	--	--	--	100	30	20	0.02	1.0
	Diff 1	13	15	7	18	--	--	6	0.005	0.5
	Diff 2	39	15	15	18	--	--	6	0.04	2.0
	Diff 3	79	15	7	18	--	--	6	0.01	~0
	Diff 4	--	--	--	--	100	30	1.5	0.01	2.0
	Fluo 1	14	15	13	5	--	30	--	--	--
	Fluo 2	*32*	*15*	*9*	5	--	30	--	--	--
Phantom 2	**Bulk**	--	--	--	--	100	38	19	0.01	1.0
	Fluo	66	19	8	5	--	35	--	**--**	**--**

3.5 Results

3.5.1 Sensitivity tests

We characterized the sensitivity of the fluorescence imaging subsystem using Phantom 2. Fluorescent tubes were inserted with varying concentrations of Cy5.5: 1000nM, 100nM, 10nM, 1nM and 0nM. As the red line shows in Figure 3.2 (d) and as shown in Figure 3.3, we scanned a 30 mm line across the phantom covering part of the fluorescent tube. The detection fibre was approximately 1 cm above the circular center of the cylindrical hole.

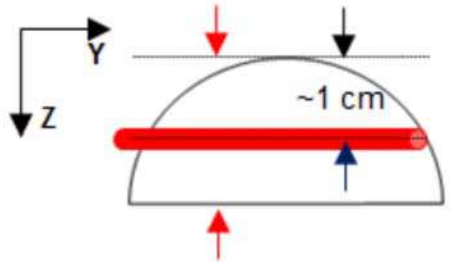

Figure 3.3: Illustration of measuring position in the sensitivity test. The red arrows represent the laser diode and the detection fiber.

The experimental parameters were as follows: 1s integration time for one scanned point, 200 KHz acquisition frequency and 10mW laser power. We collected the emitted fluorescence with a band-pass filter-710/20D (Chroma Technology). As shown in Figure 3.4 (a), the fluorescence imaging system was sensitive enough to detect 1 nM of Cy5.5 in this phantom. In Figure 3.4 (b), the fitted logarithmic peak amplitudes for different concentrations (1nM, 10nM, 100nM, 1000nM) are plotted. The linearity curve shows that the amplitudes are approximately linear over close to three decades.

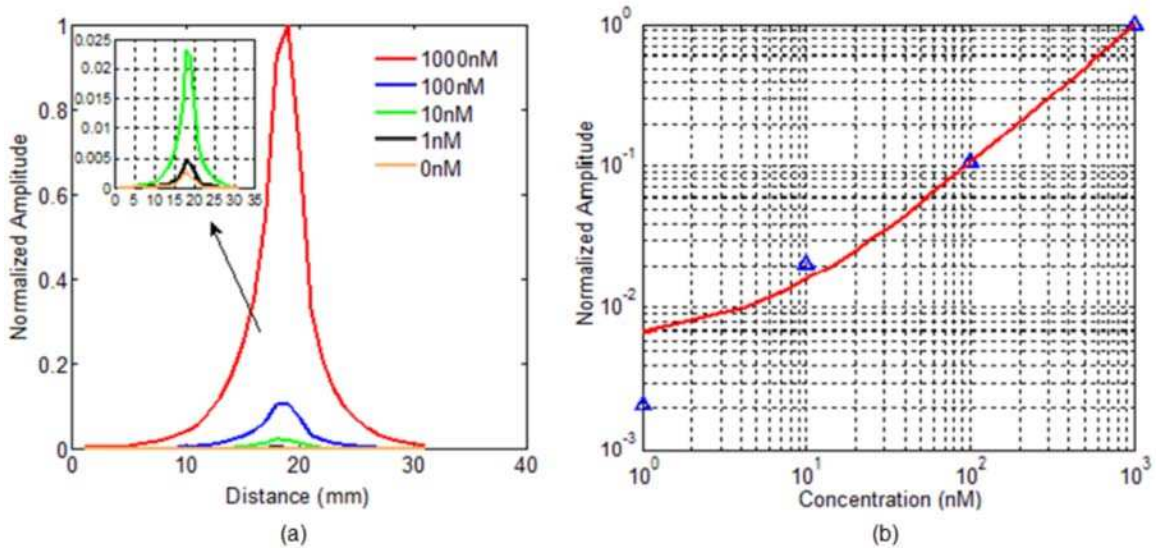

Figure 3.4: (a) normalized values of different concentration as a function of scan position. The results show that the system was able to detect 1nm cy5.5 in the phantom; (b) the curve shows the fitted logarithmic peak values as a function of concentrations. The triangular markers denote the normalized amplitude of different concentrations.

3.5.2 Phantom tests

We employed the two phantoms described above to assess the impact of using the US priors on image reconstruction. The experimental parameters for fluorescence imaging were: 200 ms exposure time for each point, 200 KHz acquisition frequency, 1 mm scan steps in X-Y direction.

For phantom 1, laser power for absorption/fluorescence measures was 20mW/50mW, whereas for phantom 2 it was 10mW/20mW. We collected the emitted fluorescence with a long-pass filter-HQ670LP (Chroma Technology) for both cases. The fiber was about 2 mm above the top surface of the phantoms. The source and detector were scanned together as a pair during each fluorescence scan. An absorption scan was also acquired for BN of fluorescence measures to eliminate the experimental factors. The varying distance between the fiber and the surface of phantom 2 was partly corrected by this normalization (for intensity), but the expanded detection area when the fiber-phantom distance increased caused some imprecision for reconstruction. The detection area with a fiber NA of 0.37 was ~1.1 mm^2 when the fiber was ~2 mm away from the surface of phantom 2 but expanded to ~4.2 mm^2 on the edges (~4mm distance). For the US imaging, we used the transducer mentioned above to scan the same ROI with the same scan steps as the fluorescence subsystem. In the experiments, the transducer surface was approximately 4 cm above the top surface of the phantoms and we averaged 1000 times for each scanned point.

Figure 3.5 shows the BN (Ntziachristos & Weissleder, 2001) transmission ratios overlaid over the pictures taken from the camera. As shown in Figure 3.5 (a), a 25mm×45mm area has been scanned on phantom 1. In Figure 3.5 (b), a 27mm×37mm area has been scanned on phantom 2. In order to couple ultrasonic pulse-echoes and optical imaging, imaging was performed in water. The phantoms were put in a container, and then separated the phantoms from water with plastic membranes. US gel was coupled to the phantom surface and then the plastic membrane overlaid to remove bubbles. We injected Cy5.5 at a concentration of 1000nM into transparent plastic tubes in both cases. As shown in Figure 3.5 (c), the cylindrical tube had varying external diameters of 4.7 mm, 3 mm, and 2.4 mm. The thickness of the wall was 0.6 mm (not shown). We inserted 30-millimetres of the tube into phantom 1 and 34-millimetres of the

tube into phantom 2, respectively. For phantom 1, we used two identical tubes with fluorochome at the same concentration (1000nM) but located at different depths. As illustrated in Figure 3.5 (a) and (b), the fluorescence signals decreased from right to left, in accordance with the decreasing dimension of the tube.

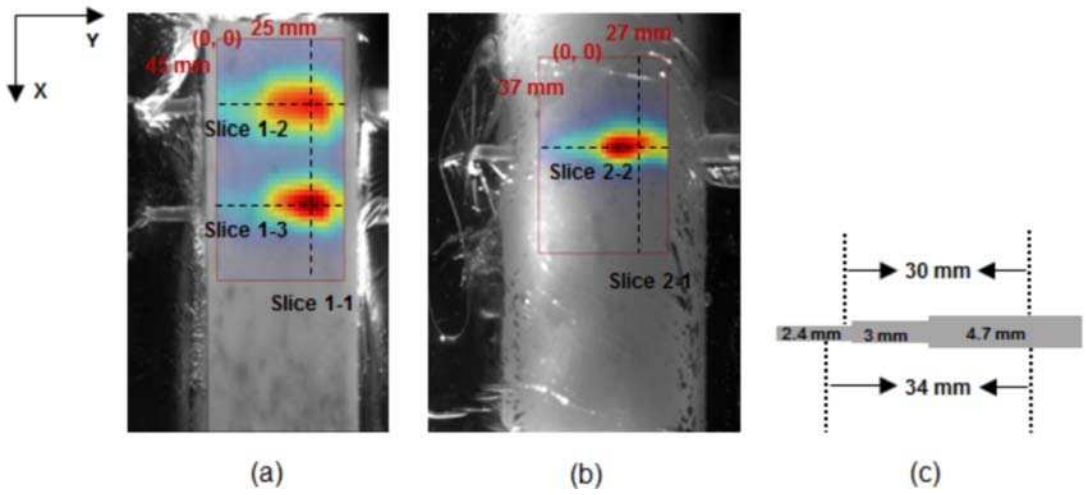

Figure 3.5: (a) The normalized fluorescence intensity of phantom 1. (b) The normalized fluorescence signal of phantom 2. (c) The dimensions of the plastic tube.

For 3D image reconstruction of these two phantoms: (1) mesh of 1 mm resolution was built for each phantom. Nodes in each mesh were assigned with homogeneous optical properties (μ_a and μ_s') using the bulk optical properties of Table 3.1. To get closer to realistic situations in vivo, we did not consider the heterogeneities in phantom 1 because the Born-normalization was expected to eliminate this effect; (2) although the surface contours of the two phantoms were recovered by the US subsystem, for simplicity, we built meshes having rectangular parallelepiped shapes for both phantoms; (3) for the reconstruction, we scaled the experimental Born-normalized ratios by the simulated excitation amplitudes and then used them as input to the forward model above (the detail of the reconstruction equations and processes can be found in

elsewhere (Dehghani et al., 2009); (4) for US image segmentation: we simply used an intensity threshold to identify inclusions in the US images which were thereafter segmented into a binary image. US image segmentation was performed slice by slice. Prior to segmentation, we multiplied the US images with a weight matrix which reduced boundary artifacts. Then we selected the pixels by a single thresholding procedure from this corrected US image generating a binary mask; the prior was defined from this mask by applying a Gaussian filter to increase the size of the selected region. Since US detected interfaces, in phantoms it led to a single line for each tube (e.g.: the two short bright lines in Figure 3.6 (a)), and the prior for the inclusion regions did not have a circular shape in X-Z direction but had the right width in Y direction. Across slices, this procedure led to consistent prior size in the volume. To account for water, the phantom 2 top surface was identified from US signals, and mesh properties were set so that optical properties for that region were set to very low absorption; (5) the US structural priors thus identified were implemented as a soft prior partially accounting for segmentation errors. Equation (3.5) was used to update the optical properties when using prior information. The regularization matrix L now encodes the spatial prior information for image reconstruction. The detail of this approach may be found elsewhere (Yalavarthy, Pogue, Dehghani, & Paulsen, 2007); (6) fluorescence field ($\eta\mu_{af}$) were reconstructed with and without the prior information for comparison.

$$\Delta\chi = [J^T J + \lambda L^T L]^{-1} J^T (\Phi^{Meas} - \Phi^C) \tag{3.5}$$

In Figure 3.6, the US images and the fluorescence reconstruction of phantom 1 are shown. The coordinate and dimension of each image slice is shown in Figure 3.5 (a). In the first column of Figure 3.6 (a), (d), (g), the US image sections at different planes (x=20, y=14 and y=32) are

shown. In the second column of Figure 3.6 (b), (e), (h), the reconstructed fluorescence images with prior information are shown for the different slices. Accordingly, in the third column of Figure 3.6 (c), (f), (i), the reconstructed fluorescence images without any prior information are shown for the different slices. As shown in Figure 3.6 (a), the width of the two tubes recovered by US is approximately 10 mm which is about two times larger than its real value. This can be explained by the use of a transducer having 0.5 inch diameter (about 2.7 times wider than the tubes) and the focal point was not well targeted at the inclusions. As shown in Figure 3.6 (j), (k), the fluorescence intensity normalized by the maximum intensity in Figure 3.6 (e), (h), respectively along each dashed line decreases from right to left. This is in agreement with the fluorescence map shown in Figure 3.5 (a) and the varying dimension of the tube shown in Figure 3.5 (c).

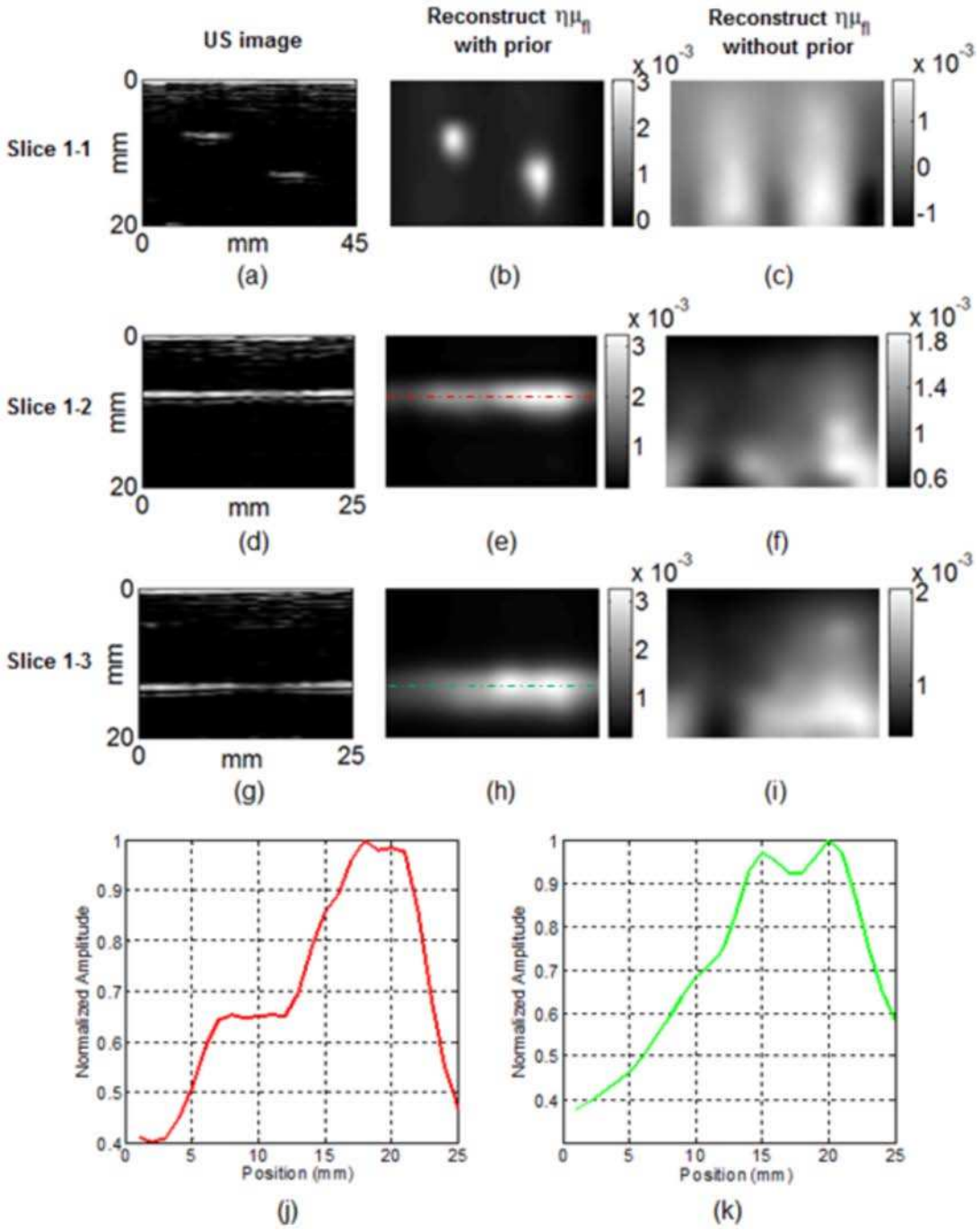

Figure 3.6: Representative images of the acquisition using phantom 1. The US images (a), (d), (g), the fluorescence reconstruction image ($\eta\mu_{fl}$ in mm^{-1}) with priors (b), (e), (h), and without priors (c), (f), (i) are shown for image slices at x=20 (a)-(c), at y=14 (d)-(f) and at y=32 (g)-(i)

respectively. Intensity plots along the red (j) dashed line in Figure 3.6 (e) and along the green (k) dashed line in Figure 3.6 (h) are also shown.

Figure 3.7 shows the fluorescence images overlaid on the US images. It confirms that the locations of the fluorescence inclusions may be accurately reconstructed and benefit from the co-registered US priors.

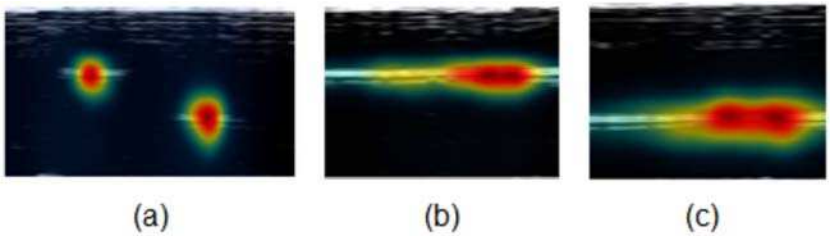

Figure 3.7: (a) Overlaid image at x=20. (b) Overlaid image at y=14. (c) Overlaid image at y=32.

In Figure 3.8, the US images and the fluorescence reconstruction of phantom 2 are shown. The coordinate and dimension of each image section may be referred to Figure 3.5 (b). In the first column of Figure 3.8 (a), (d), the US image sections at different slices (x=12, y=18) are shown, respectively. In the second column of Figure 3.8 (b), (e), the reconstructed fluorescence images at slices x=12, y=18 with prior information are shown. Accordingly, in the third column of Figure 3.6 (c), (f), the reconstructed fluorescence images at slices x=12, y=18 without any prior information are shown. As shown in Figure 3.8 (g), the fluorescence intensity normalized by the maximum intensity in Figure 3.8 (e) along the dashed line decreases from right to left. This is in agreement with the results found for phantom 1.

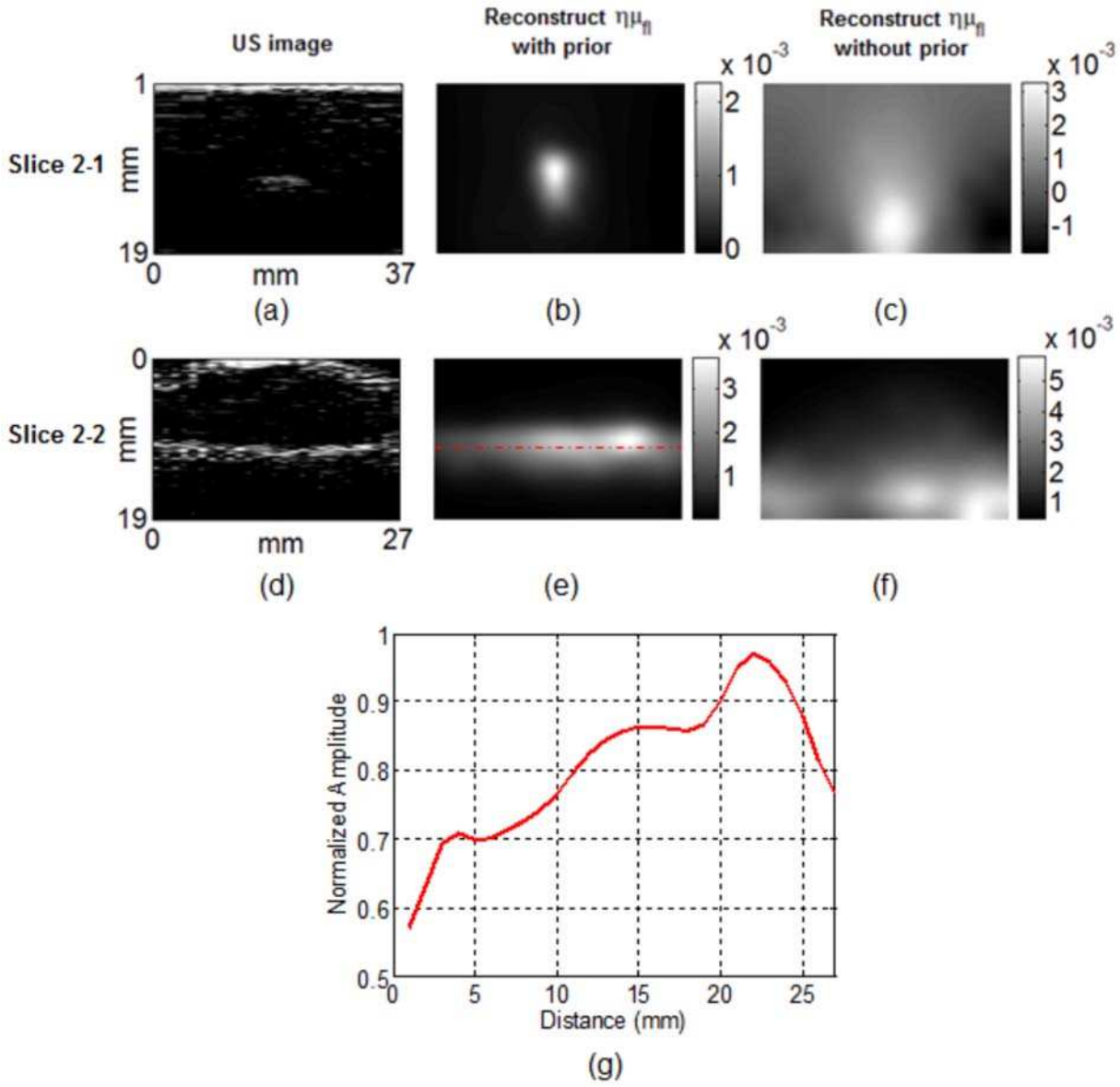

Figure 3.8: Representative images using phantom 2. The US images (a) and (d), the fluorescence reconstruction image ($\eta\mu_{fl}$ in mm^{-1}) with priors (b) and (e), and without priors (c) and (f) are shown for image slices at x=12 (a)-(c) and at y=18 (d)-(f). Intensity plot along the red (g) dashed line in Figure 3.8 (e) is also shown.

Figure 3.9 provides the fluorescence images overlaid on the US images confirming that the use of US priors improves fluorescence image reconstruction.

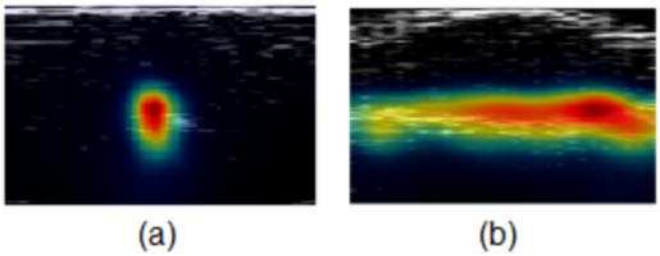

Figure 3.9: (a) Overlaid image at x=12. (b) Overlaid image at y=18.

3.5.3 In vivo results

We further tested our system in an in-vivo environment. As shown in Figure 3.10 (a), an Apo-E mouse of 23-week fed on high cholesterol diet (HCD) was imaged 20 hours after intravenous administration of a molecular probe. We employed an Alexa-647 based probe to detect VCAM monocyte recruitment activity, which was reported to be a valuable biomarker and an early signal involved in the formation of atherosclerotic plaque and the inflammation process (Jaffer, Libby, & Weissleder, 2007, 2009b; U. Prahl et al., 2010; Rader & Daugherty, 2008; Sanz & Fayad, 2008). VCAM is expected to be expressed in aorta, heart valve and heart. However, the 1 mm resolution acoustic scan was not precise enough to delineate the structure of the aorta. For our proof-of-concept study, we thus reconstructed the fluorescence emission from the heart area (Tardif et al., 2011).

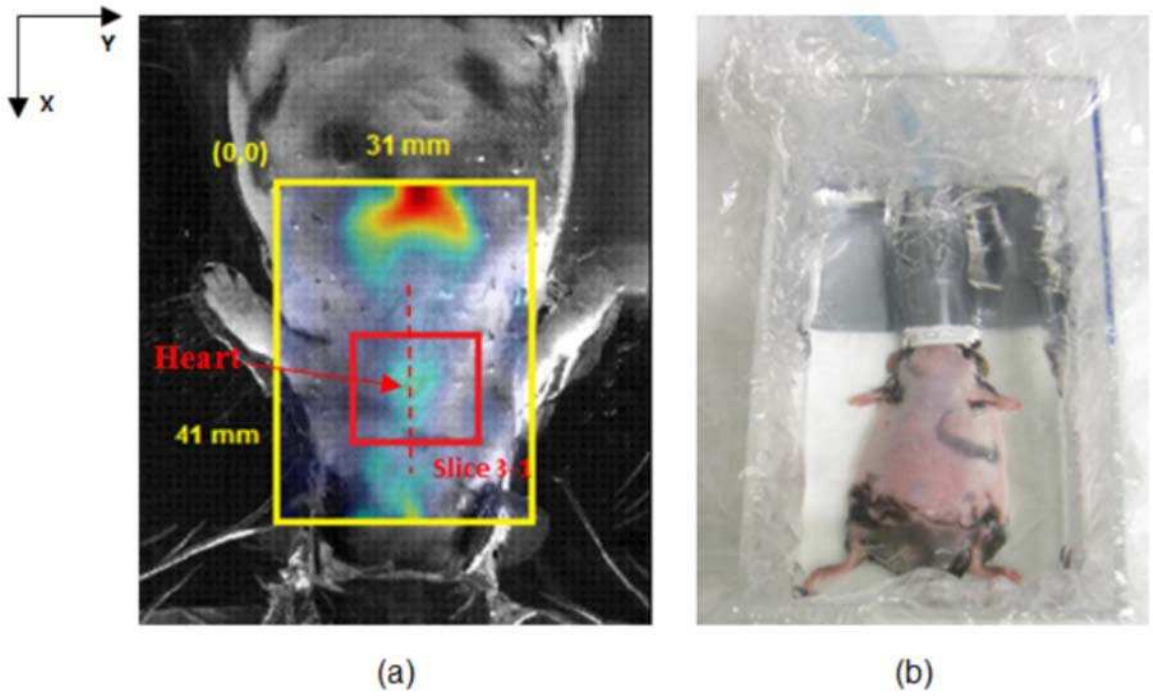

Figure 3.10: (a) The BN ratio overlaid with the picture. (b) Illustration of the animal manipulation.

To couple the ultrasonic pulse echoes, we performed US and fluorescence imaging in warm water. As shown in Figure 3.10 (b), the mouse was fit in a water container having a hole and connecting a tube used to deliver anesthetic gas. A transparent plastic membrane was used in similar fashion to phantoms with US gel used to couple the membrane to the body. The entire scan, including one absorption scan, one fluorescence scan and US scan, was performed under 45 minutes in vivo. The ethics committees of Montreal Heart Institute and École Polytechnique de Montréal approved all animal manipulations.

Figure 3.10 (a) shows the Born-normalized transmission ratios overlaid with the picture taken from the camera. As the yellow outline in Figure 3.10 (a), a 31mm×41mm area has been scanned on the mouse. The experimental parameters for fluorescence were: 200 ms exposure time for each point; 200 KHz acquisition frequency; 1 mm scan steps in X-Y direction; laser

power for absorption/fluorescence measures was 30mW/50mW, respectively. We collected the emitted fluorescence with a long-pass filter-HQ670LP (Chroma Technology). For US imaging, we used the transducer mentioned above to scan the same ROI with the same scan steps as the fluorescence subsystem did. In the experiment, the transducer surface was approximately 1.5 cm above the top surface of the mouse and we averaged 1000 times for each scanned point. For both fluorescence and US imaging, we detected the belly side of the mouse, which was close to the heart.

For 3D fluorescence image reconstruction of in-vivo data: (1) a volume based on the scanned area was reconstructed; (2) a mesh of 1 mm resolution was built. Optical properties of the mesh were assigned μ_a=0.02 mm^{-1} and $\mu s'$=1 mm^{-1} for the background, and μ_a=0.2 mm^{-1} and μ_s'=1 mm^{-1} for the heart; (3) although the surface contour of the mouse was recovered by the US subsystem, for simplicity, we built a mesh having a rectangular parallelepiped shape; (4) for the reconstruction, we employed the dataset detected from the area denoted by the red outline as shown in Figure 3.10 (a), which would cover the fluorescence emitted from the heart of the mouse. We scaled the experimental Born-normalized ratios by the simulated excitation amplitudes and then used them as input to the forward model above; (5) we manually segmented the US image into a binary image (0: background, 1: heart) slice by slice. The heart area is illustrated by the red dashed outline in Figure 3.11 (a). The region reconstructed over the heart was relatively flat and the profile was not taken into account in this reconstruction; (6) the US prior constrained the reconstruction as soft a prior; (7) fluorescence field ($\eta\mu_{fl}$) were reconstructed with and without the prior information for comparison.

In Figure 3.11, a representative 2D fluorescence reconstruction image in X-Z section and the correspondent US image slice of the mouse are shown. The coordinate and dimension of the

image slice (y=15, 25mm in x direction) are denoted by the red dashed line (Slice 3-1) in Figure 3.10 (a). In Figure 3.11 (a), the 2D US image slice shows the heart of the mouse. However, the outline of the heart and the aorta in this US image is not very clear. This can be explained by: (1) the transducer having a fixed focal length was not well focused on the interested spot; (2) 1mm resolution of motor motion was not enough for US imaging, especially small object; (3) the biological fact of mouse that heart was partly under rib cage posed a challenge for this application. In Figure 3.11 (b) and (c), the reconstructed fluorescence images with and without prior are shown, respectively. The improvement of the fluorescence image with prior over the one without demonstrates that US imaging may benefit fluorescence imaging even in an in-vivo environment. In Figure 3.12, the overlaid fluorescence/US image shows that the location of the fluorescence may be accurately reconstructed and benefit from the co-registered US priors.

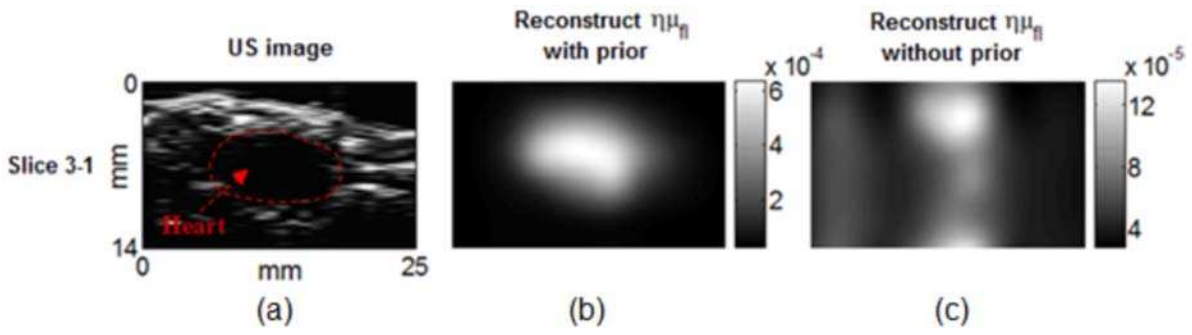

Figure 3.11: Representative images of slice 3-1 of the mouse: (a) The US image shows the heart of the mouse; (b) the fluorescence reconstruction image ($\eta\mu_{fl}$ in mm^{-1}) with priors and (c) without.

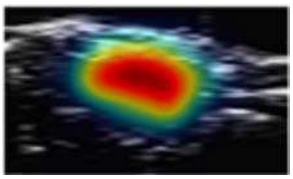

Figure 3.12: The overlaid image of slice 3-1.

3.5.4 Analysis of the results

Phantom results demonstrate that the US subsystem is able to recover the boundary and the inclusions of the phantoms, which provides a strategy to explore structural priors for fluorescence reconstruction. Furthermore, the US priors significantly improved fluorescence reconstruction quality. To quantify the results, we compared the contrast to noise ratio (CNR) to evaluate the performance of the reconstruction with priors. Herein, we define that CNR = $(S_A - S_B)/\sigma$, where S_A and S_B are the mean intensities of the ROI and background, respectively, and σ is the standard deviation of the background. Table 3.2 provides a resume of the results for both CNR1 and CNR2, which is the CNR of the reconstructions with and without priors respectively, showing that the use of priors resulted in CNRs 4-20 times higher than the ones without. This advantage is further confirmed by our in-vivo experiment, which shows that the image using US prior resulted in CNR 4.79 times higher than the one without.

Table 3.2: CNR of the reconstruction images. CNR1 and CNR2 represent the CNR of the reconstructions with prior and the ones without priors, respectively.

	Image section	**Coordinate**	**CNR_1/CNR_2**
Phantom 1	**Slice 1-1**	x = 20	5.78/1.31
	Slice 1-2	y = 14	4.33/0.28
	Slice 1-3	y = 32	5.18/0.63
Phantom 2	**Slice 2-1**	x = 12	7.09 /1.41
	Slice 2-2	y = 18	3.29/0.16
Mouse	**Slice 3-1**	y = 15	3.26/0.68

Herein, to evaluate quantification with the phantoms, we compared the normalized maximum values of $\eta\mu_{af}$ in the images Figure 3.6 (e), (h) and Figure 3.8 (e) denoted in Figure 3.13 as A, B and C, respectively. The same fluorophore concentration was used in both phantoms and different depths, the value of $\eta\mu_{fl}$ should be the same once reconstructed. In

phantom 1, but at different depths, error was found to be small ~4%. When comparing different phantoms (different optical properties and geometry), the error was ~14%. This could be explained by that the phantom 2 has a smaller μ_a and μ_s', and the expanded detection area caused inaccuracy in reconstruction.

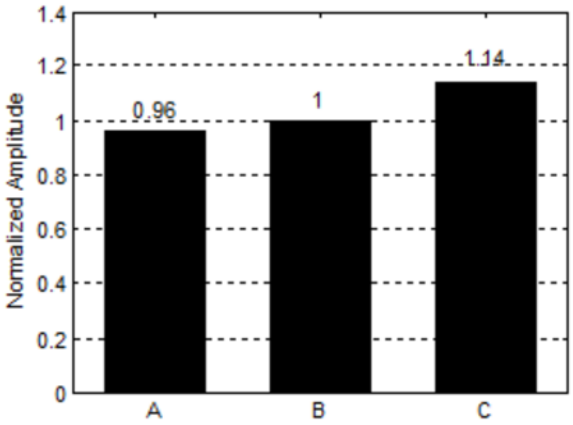

Figure 3.13: Quantification with the two phantoms by comparing the normalized maximum value of $\eta\mu_{fl}$ in each fluorescence image slice.

3.6 Discussion

In this paper we have presented a combined fluorescence/US imaging system. The fluorescence tomography subsystem was used to explore 3D fluorescence emission; the US subsystem was used to detect 3D interface of both the surface and the inclusion (e.g. fluorescent tube or the heart of the mouse) of the object, which could provide structural image and impose constraint for fluorescence reconstruction. The performance of this system was quantified using two phantoms having different shapes, constitutions and dimensions. Phantom results showed that the fluorescence reconstruction image quality could be significantly improved using the US structural priors. Also, the US images could help to interpret the reconstructed functional images at different sections. As a proof-of-concept study, we further tested the system by imaging

VCAM activity in a model of atherosclerosis. In-vivo results indicated that this system has the potential to be applied in in-vivo molecular imaging study.

Compared with previous studies, our system has achieved 3D imaging for both fluorescence and US imaging. Three dimensional US imaging is expected to provide richer structural prior information than a 2D US detector array did (Q. Zhu et al., 1999), and the raster-scanned 3D US data sampling available in this system enabled the delineation of structural priors by segmenting the US image rather estimating the size of inclusion by two orthogonal image-slices (Quing Zhu et al., 2003). We thus expect our system not to be limited to inclusions with regular shapes. As evidence, phantoms results also reconstructed the shapes of the fluorescent tubes having a decreasing diameter; and in-vivo results indicated that this system could record anatomical and functional images in small animals. The scanning configuration proposed here was automatically co-registered which further facilitated dual modality analyses.

Furthermore, in comparison to reflection mode, which is limited by detection depth in diffusive media (Björn et al., 2010), fluorescence imaging in transmission mode has better sensitivity and detection depth. Illumination with a collimated laser beam is expected to be less affected by non-specific signal contamination than a broad beam system would (Frederic Leblond et al., 2010). Combining all the advantages mentioned above, the work presented in this paper exhibits a promising strategy for exploring anatomical and functional information at very low-cost (less than 9k$).

The simplicity of this system brought the following main drawbacks. (1) The limited view by scanning a single source-detector pair achieved less information than a camera-based system would. (2) Raster-scanned point source imaging meant longer acquisition time compared with a wide illumination camera based configuration. With the experimental parameters

mentioned above, 1196 points, 1064 points, and 1344 points of measurement were collected for phantom 1, phantom 2, and the Apo-E mouse, respectively. For the in-vivo experiment, the acquisition including an absorption scan, a fluorescence scan and an ultrasonic scan was finished within 45 minutes. However, this time may vary depending on the dimension of field of view (FOV) and scan steps. (3) US imaging has limitations for this application. In particular US images are difficult to segment, which poses a challenge when trying to gather a precise atlas for the whole body of small animals. These difficulties were present in our experiments while trying to image over of the heart of the mouse since the heart, located partly under rib cage, blurred the US image in some sections. (4) US segmentation in some situations may lead to wrong priors due to these issues. The soft prior used here was however shown in other studies (Yalavarthy, Pogue, Dehghani, Carpenter, et al., 2007) to be more immune to the prior uncertainty.

This dual modality approach might be further improved by simple modifications whiles preserving the low-cost concept. (1) We employed a single trans-illumination channel to collect the fluorescent photons. Adding a source channel to explore reflective emission could further enhance the precision for quantification of fluorescence images. (2) The method used to couple ultrasonic pulse-echoes added difficulties in conducting experiments due to the necessity of using a membrane. When manipulating animals, overlay of the plastic membrane on the animal to separate it from water could be a drawback. A potential solution is to detect ultrasonic signals from the bottom of the object. In this way, the ultrasonic transducer will still be scanned in water with object located above water. (3) Further improvements to optimize the scanning: a translation stage to adjust the focusing of the ultrasonic transducer may improve the longitudinal resolution; stepping motors having better resolution and higher velocity can be employed to increase the horizontal resolution of the US image and speed up the scanning; finally, a portable

projector can be used in conjunction with the camera to measure the profile of the object quickly. In this proof of concept work we used simple threshold to implement spatial priors but improved algorithms can be developed for US image processing and segmentation.

3.7 Conclusion

So, although US imaging provide limited structural information comparing to that of MRI or X-ray CT, the benefits to fluorescence reconstruction are still significant. To be noticed, the multi-spectral feature of this system has not been fully used yet. Therefore, it is expected that the reconstruction quality may be further improved if we add multi-spectral measures to image reconstruction (Zavattini et al., 2006b). Finally, the co-registration of both imaging modalities may facilitate the understanding of the images by investigators. The future works include optimizing both hardware and algorithm of this system and cardiovascular disease study with small animals by molecular imaging offered by this proposed system.

3.8 Acknowledgements

The authors would like to thank Prof. Frederic Leblond for assistance in NIRFAST. We also thank Nicolas Ouakli for making the semi-cylindrical phantom. This work has been funded by a NSERC Discovery grant to F. Lesage. B. Li is funded by China Scholarship Council (CSC).

3.9 References

Ale, A., Schulz, R. B., Sarantopoulos, A., & Ntziachristos, V. (2010). Imaging performance of a hybrid x-ray computed tomography-fluorescence molecular tomography system using priors. Medical Physics, 37(5), 1976–1986.

Björn, S., Ntziachristos, V., & Schulz, R. (2010). Mesoscopic epifluorescence tomography: reconstruction of superficial and deep fluorescence in highly-scattering media. Optics Express, 18(8), 8422–8429.

Brooksby, B. A., Dehghani, H., Pogue, B. W., & Paulsen, K. D. (2003). Near-infrared (NIR) tomography breast image reconstruction with a priori structural information from MRI: algorithm development for reconstructing heterogeneities. Selected Topics in Quantum Electronics, IEEE Journal of, 9(2), 199–209. doi:10.1109/JSTQE.2003.813304

D'Andrea, C., Spinelli, L., Comelli, D., Valentini, G., & Cubeddu, R. (2005). Localization and quantification of fluorescent inclusions embedded in a turbid medium. Physics in Medicine and Biology, 50(10), 2313–2327. doi:10.1088/0031-9155/50/10/009

Davis, S. C., Dehghani, H., Wang, J., Jiang, S., Pogue, B. W., & Paulsen, K. D. (2007). Image-guided diffuse optical fluorescence tomography implemented with Laplacian-type regularization. Optics Express, 15(7), 4066–4082. doi:10.1364/OE.15.004066

Davis, S. C., Pogue, B. W., Springett, R., Leussler, C., Mazurkewitz, P., Tuttle, S. B., … Paulsen, K. D. (2008). Magnetic resonance-coupled fluorescence tomography scanner for molecular imaging of tissue. The Review of Scientific Instruments, 79(6). doi:10.1063/1.2919131

Dehghani, H., Eames, M. E., Yalavarthy, P. K., Davis, S. C., Srinivasan, S., Carpenter, C. M., … Paulsen, K. D. (2009). Near infrared optical tomography using NIRFAST: Algorithm for numerical model and image reconstruction. Communications in Numerical Methods in Engineering, 25(6), 711–732. doi:10.1002/cnm.1162

Fang, Q., Moore, R. H., Kopans, D. B., & Boas, D. A. (2010). Compositional-prior-guided image reconstruction algorithm for multi-modality imaging. Biomedical Optics Express, 1(1), 223–235. doi:10.1364/BOE.1.000223

Gibson, A. P., Hebden, J. C., & Arridge, S. R. (2005). Recent advances in diffuse optical imaging. Physics in Medicine and Biology, 50(4), R1–R43.

Graves, E. E., Ripoll, J., Weissleder, R., & Ntziachristos, V. (2003). A submillimeter resolution fluorescence molecular imaging system for small animal imaging. Medical Physics, 30(5), 901–911.

Gruber, J. D., Paliwal, A., Krishnaswamy, V., Ghadyani, H., Jermyn, M., O'Hara, J. A., … Pogue, B. W. (2010). System development for high frequency ultrasound-guided fluorescence quantification of skin layers. Journal of Biomedical Optics, 15(2), 026028. doi:10.1117/1.3374040

Guven, M., Yazici, B., Intes, X., & Chance, B. (2005). Diffuse optical tomography with a priori anatomical information. Physics in Medicine and Biology, 50(12), 2837–2858. doi:10.1088/0031-9155/50/12/008

Holboke, M. J., Tromberg, B. J., Li, X., Shah, N., Fishkin, J., Kidney, D., … Yodh, A. G. (2000). Three-dimensional diffuse optical mammography with ultrasound localization in a human subject. Journal of Biomedical Optics, 5(2), 237–247.

Intes, X., Maloux, C., Guven, M., Yazici, B., & Chance, B. (2004). Diffuse optical tomography with physiological and spatial a priori constraints. Physics in Medicine and Biology, 49(12), N155–N163. doi:10.1088/0031-9155/49/12/N01

Jaffer, F. A., Libby, P., & Weissleder, R. (2007). Molecular imaging of cardiovascular disease. Circulation, 116(9), 1052–1061. doi:10.1161/CIRCULATIONAHA.106.647164

Jaffer, F. A., Libby, P., & Weissleder, R. (2009). Optical and multimodality molecular imaging: insights into atherosclerosis. Arteriosclerosis, Thrombosis, and Vascular Biology, 29(7), 1017–1024. doi:10.1161/ATVBAHA.108.165530

Kepshire, D., Mincu, N., Hutchins, M., Gruber, J., Dehghani, H., Hypnarowski, J., … Pogue, B. W. (2009). A microcomputed tomography guided fluorescence tomography system for small animal molecular imaging. The Review of Scientific Instruments, 80(4), 043701. doi:10.1063/1.3109903

Kumar, A. T. N., Raymond, S. B., Dunn, A. K., Bacskai, B. J., & Boas, D. A. (2008). A time domain fluorescence tomography system for small animal imaging. IEEE Transactions on Medical Imaging, 27(8), 1152–1163. doi:10.1109/TMI.2008.918341

Leavesley, S., Jiang, Y., Patsekin, V., Rajwa, B., & Robinson, J. P. (2008). An excitation wavelength-scanning spectral imaging system for preclinical imaging. The Review of Scientific Instruments, 79(2 Pt 1), 023707. doi:10.1063/1.2885043

Leblond, F., Davis, S. C., Valdés, P. A., & Pogue, B. W. (2010). Pre-clinical whole-body fluorescence imaging: Review of instruments, methods and applications. Journal of Photochemistry and Photobiology. B, Biology, 98(1), 77–94. doi:10.1016/j.jphotobiol.2009.11.007

Lin, Y., Barber, W. C., Iwanczyk, J. S., Roeck, W., Nalcioglu, O., & Gulsen, G. (2010). Quantitative fluorescence tomography using a combined tri-modality FT/DOT/XCT system. Optics Express, 18(8), 7835–7850. doi:10.1364/OE.18.007835

Lin, Y., Gao, H., Nalcioglu, O., & Gulsen, G. (2007). Fluorescence diffuse optical tomography with functional and anatomical a priori information: feasibility study. Physics in Medicine and Biology, 52(18), 5569–5585. doi:10.1088/0031-9155/52/18/007

Lin, Y., Ghijsen, M. T., Gao, H., Liu, N., Nalcioglu, O., & Gulsen, G. (2011). A photo-multiplier tube-based hybrid MRI and frequency domain fluorescence tomography system for small animal imaging. Physics in Medicine and Biology, 56(15), 4731–4747. doi:10.1088/0031-9155/56/15/007

Milstein, A. B., Stott, J. J., Oh, S., Boas, D. A., Millane, R. P., Bouman, C. A., & Webb, K. J. (2004). Fluorescence optical diffusion tomography using multiple-frequency data. Journal of the Optical Society of America. A, Optics, Image Science, and Vision, 21(6), 1035–1049.

Montet, X., Figueiredo, J.-L., Alencar, H., Ntziachristos, V., Mahmood, U., & Weissleder, R. (2007). Tomographic fluorescence imaging of tumor vascular volume in mice. Radiology, 242(3), 751–758. doi:10.1148/radiol.2423052065

Nakashima, Y., Plump, A., Raines, E., Breslow, J., & Ross, R. (1994). ApoE-deficient mice develop lesions of all phases of atherosclerosis throughout the arterial tree. Arterioscler Thromb Vasc Biol. Retrieved from http://atvb.ahajournals.org/cgi/content/abstract/14/1/133

Ntziachristos, V., & Weissleder, R. (2001). Experimental three-dimensional fluorescence reconstruction of diffuse media by use of a normalized Born approximation. Optics Letters, 26(12), 893–895. doi:10.1364/OL.26.000893

Ntziachristos, V., & Weissleder, R. (2002). Charge-coupled-device based scanner for tomography of fluorescent near-infrared probes in turbid media. Medical Physics, 29(5), 803–809.

Patwardhan, S., Bloch, S., Achilefu, S., & Culver, J. (2005). Time-dependent whole-body fluorescence tomography of probe bio-distributions in mice. Optics Express, 13(7), 2564–2577. doi:10.1364/OPEX.13.002564

Pogue, B. W., Gibbs, S. L., Chen, B., & Savellano, M. (2004). Fluorescence imaging in vivo: raster scanned point-source imaging provides more accurate quantification than broad beam geometries. Technology in Cancer Research & Treatment, 3(1), 15–21.

Prahl, U., Holdfeldt, P., Bergström, G., Fagerberg, B., Hulthe, J., & Gustavsson, T. (2010). Percentage white: a new feature for ultrasound classification of plaque echogenicity in carotid artery atherosclerosis. Ultrasound in Medicine & Biology, 36(2), 218–226. doi:10.1016/j.ultrasmedbio.2009.10.002

Rader, D. J., & Daugherty, A. (2008). Translating molecular discoveries into new therapies for atherosclerosis. Nature, 451(7181), 904–913. doi:10.1038/nature06796

Sanz, J., & Fayad, Z. A. (2008). Imaging of atherosclerotic cardiovascular disease. Nature, 451(7181), 953–957. doi:10.1038/nature06803

Schulz, R. B., Ale, A., Sarantopoulos, A., Freyer, M., Söhngen, R., Zientkowska, M., & Ntziachristos, V. (2009). Hybrid fluorescence tomography/x-ray tomography improves reconstruction quality, 73700H–73700H. doi:10.1117/12.831714

Snyder, C., Kaushal, S., Kono, Y., Tran Cao, H., Hoffman, R., & Bouvet, M. (2009). Complementarity of ultrasound and fluorescence imaging in an orthotopic mouse model of pancreatic cancer. BMC Cancer, 9(1), 106. doi:10.1186/1471-2407-9-106

Soubret, A., Ripoll, J., & Ntziachristos, V. (2005). Accuracy of fluorescent tomography in the presence of heterogeneities: Study of thenormalized born ratio. IEEE Transactions on Medical Imaging, 24(10), 1377–1386.

Tan, Y., & Jiang, H. (2008). Diffuse optical tomography guided quantitative fluorescence molecular tomography. Applied Optics, 47(12), 2011–2016. doi:10.1364/AO.47.002011

Tardif, J.-C., Lesage, F., Harel, F., Romeo, P., & Pressacco, J. (2011). Imaging Biomarkers in Atherosclerosis Trials. Circulation: Cardiovascular Imaging, 4(3), 319–333. doi:10.1161/CIRCIMAGING.110.962001

Yalavarthy, P. K., Pogue, B. W., Dehghani, H., Carpenter, C. M., Jiang, S., & Paulsen, K. D. (2007). Structural information within regularization matrices improves near infrared diffuse optical tomography. Optics Express, 15(13), 8043–8058. doi:10.1364/OE.15.008043

Yalavarthy, P. K., Pogue, B. W., Dehghani, H., & Paulsen, K. D. (2007). Weight-matrix structured regularization provides optimal generalized least-squares estimate in diffuse optical tomography. Medical Physics, 34(6), 2085. doi:10.1118/1.2733803

Zavattini, G., Vecchi, S., Mitchell, G., Weisser, U., Leahy, R. M., Pichler, B. J., Cherry, S. R. (2006a). A hyperspectral fluorescence system for 3D in vivo optical imaging. Physics in Medicine and Biology, 51(8), 2029–2043. doi:10.1088/0031-9155/51/8/005

Zavattini, G., Vecchi, S., Mitchell, G., Weisser, U., Leahy, R. M., Pichler, B. J., Cherry, S. R. (2006b). A hyperspectral fluorescence system for 3D in vivo optical imaging. Physics in Medicine and Biology, 51(8), 2029–2043.

Zhu, Q., Durduran, T., Ntziachristos, V., Holboke, M., & Yodh, A. G. (1999). Imager that combines near-infrared diffusive light and ultrasound. Optics Letters, 24(15), 1050–1052. doi:10.1364/OL.24.001050

Zhu, Q., Huang, M., Chen, N., Zarfos, K., Jagjivan, B., Kane, M., Kurtzman, H. S. (2003). Ultrasound-Guided Optical Tomographic Imaging of Malignant and Benign Breast Lesions: Initial Clinical Results of 19 Cases. Neoplasia (New York, N.Y.), 5(5), 379–388.

CHAPTER 4 ARTICLE #2: ULTRASOUND GUIDED FLUORESCENCE MOLECULAR TOMOGRAPHY WITH IMPROVED QUANTIFICATION BY AN ATTENUATION COMPENSATED BORN-NORMALIZATION AND IN VIVO PRECLINICAL STUDY OF CANCER

Baoqiang Li[1,2], Romain Berti[1,2], Maxime Abran[1,2], Frédéric Lesage[1,2]

[1]Institute of Biomedical Engineering, École Polytechnique de Montréal, Montreal, QC, H3C 3A7, Canada. [2]Montreal Heart Institute, Montreal, QC, H1T 1C8, Canada

4.1 Presentation of the article

This article (B. Li, et al., 2014) aimed to address the second objective of this thesis. Following the first work (article #1), we upgraded the fluorescence-US imaging system with respects to optical and acoustic sampling precision as well as reconstruction mechanism. The proposed data calibration technique and the reconstruction method were evaluated by simulations and phantoms. In vivo experiment with preclinical tumorous mice further validated this dual-modality imaging approach. This article was published in *Review of Scientific Instrument*.

4.2 Abstract

US imaging, having the advantages of low-cost and non-invasiveness over MRI and X-ray CT, was reported by several studies as an adequate complement to FMT with the perspective of improving localization and quantification of fluorescent molecular targets in-vivo. Based on the previous work, an improved dual-modality Fluorescence-US imaging system was developed, and then validated in imaging study with preclinical tumor model. US imaging and a profilometer were used to obtain the anatomical prior information and 3D surface, separately, to precisely extract the tissue boundary on both sides of sample in order to achieve improved fluorescence reconstruction. Furthermore, a pattern-based fluorescence reconstruction on the detection side was incorporated to enable dimensional reduction of the dataset while keeping the useful information for reconstruction. Due to its putative role in the current imaging geometry and the chosen reconstruction technique, we developed an attenuation compensated BN method to reduce the attenuation effects and cancel off experimental factors when collecting quantitative fluorescence datasets over large area. Results of both simulation and phantom study

demonstrated that fluorescent targets could be recovered accurately and quantitatively using this reconstruction mechanism. Finally, in-vivo experiment confirms that the imaging system associated with the proposed image reconstruction approach was able to extract both functional and anatomical information, thereby improving quantification and localization of molecular targets.

4.2.1 Key words

Fluorescence, ultrasound, reconstruction, prior, normalization, imaging, mice, cancer

4.3 Introduction

By combining optical imaging with administration of exogenous fluorescent agents (Jaffer, Kim, et al., 2007; Waldeck et al., 2008; Wallis de Vries et al., 2009; Weissleder, Tung, Mahmood, & Bogdanov, 1999; Tawakol et al., 2008), disease-related molecular activities can be revealed by recovering fluorophore distribution in tissue. Due to its simplicity, fluorescence imaging remains attractive for such studies; however, there is an increasing awareness of difficulties in quantifying such distributions, leading to efforts towards combining it with modalities providing complementary information. As a result, dual-modality molecular imaging is increasingly being used in in-vivo studies with small animals (Aikawa et al., 2007; Ale et al., 2012b; Jaffer et al., 2009a; Nahrendorf et al., 2009, 2010). Hybrid-modality systems have advantages over standalone solution by providing anatomical substrate, which in turn can be used to better quantify and localize fluorescent markers (Davis et al., 2007b; Y Lin et al., 2007; Yalavarthy, Pogue, Dehghani, Carpenter, et al., 2007). So far, X-ray CT, MRI and ultrasound (US) have been incorporated with fluorescence imaging; and benefits were demonstrated by several studies (Ale et al., 2010; Brooksby et al., 2003; Davis et al., 2008; Gruber et al., 2010b; Holboke et al., 2000; D. Kepshire et al., 2009; Y Lin et al., 2011b; Yuting Lin et al., 2010a; Schulz et al., 2009; Snyder

et al., 2009; Q. Zhu et al., 1999; Quing Zhu et al., 2003). In our previous work, a low-cost dual-modality Fluorescence-US imaging system was developed; and both phantom and animal experiments demonstrated significant potential for in-vivo applications (B. Li & Lesage, 2012; B. Li et al., 2011).

In this study, an improved Fluorescence-US system was developed using again transmission geometry but extending the detection from a single detector to a sensitive camera. The large detection area provided by the camera has multiple benefits: 1) it enables recording a large number of detector positions for each source position; 2) it can be used to integrate a profilometer providing, with US, a full view of the profile of sample thereby improving its geometric modeling. Due to the large number of detection points, a pattern-based Monte Carlo forward model was developed to simulate photon propagation in tissue. Inspired by other study (Markel et al., 2003), but adapted to non-uniform geometries, this reconstruction strategy had the advantage of preserving the important components of the dataset while avoiding intensive computation associated with a large number of detectors. It was demonstrated in several studies that a fast and quantitative reconstruction could be achieved by performing pattern modulated illumination. For example, D'Andrea et al developed a diffuse optical tomography system with structured light illumination (D'Andrea, Ducros, Bassi, Arridge, & Valentini, 2010). Projecting sinusoidal modulated light onto the surface of thick samples, reduced sampling for an informative dataset was achieved when compared to raster-scanned illumination; thereby a fast reconstruction was possible due to the reduced dimension of measurements. Ducros et al also reported that with the measurement-derived wavelet illumination patterns, informative measurements could be collected to enable a fast reconstruction (Ducros et al., 2010). As an extension, a virtual source pattern (VSP) method was further developed (Ducros et al., 2012).

This VSP method, which can get rid of DC components in illumination patterns as well as being capable of rejecting the undesirable sources of light, was demonstrated to significantly improve the reconstruction. In distinction from these studies, we kept a traditional point-based raster-scanned illumination for fluorescence imaging in order to incorporate fluorescence imaging with a US transducer for a dual-modality acquisition. Instead, the pattern-based approach was exploited on the detection side, which was also expected to reduce the dimension and keep the primary components of measurements. Further, to optimize the prior information for fluorescence reconstruction, the US anatomy and the 3D profile was combined. First, the boundary of the tissue close to the US transducer side could be recovered. Second, a profilometer was added to retrieve the tissue boundary of the opposite side. Therefore, concatenating these two surfaces information, we were able to precisely define a tissue region for forward modeling. Thirdly, from the 3D US imaging, the inclusion/lesion could be identified anatomically, and then used for constraining the reconstruction. Moreover, to correct the absorption and the distance effects along the light travelling path, an attenuation compensated Born-normalization (ACBN) method is proposed. In comparison to the standard BN (Ntziachristos & Weissleder, 2001), the ACBN method showed increased robustness when the object was deeply embedded within heterogeneous media. Finally, simulation study, phantom experiment and in-vivo experiment were conducted. In simulation, with the proposed reconstruction mechanism and the ACBN method, the averaged reconstructed fluorescence yield in the lesion was at worst as close as 86% of the true value with a noise level of 10%. Further, the benefit of the proposed reconstruction technique associated with the ACBN processing was evaluated with phantom; both the raw data and the reconstruction results showed the enhanced robustness of the ACBN over the standard BN. In animal experiment, with the imaging system and the proposed algorithm, the fluorescence

yield was quantified and correctly localized. Results were further validated with ex-vivo measurement.

4.4 Methods

4.4.1 System design

As illustrated in the Figure 4.1, an incident laser beam at 658nm (HL6512MG, Thorlabs) was first cleaned up by a band-pass filter D650/20 (Chroma Technology), then coupled into an optical fiber, and ultimately illuminated the bottom side of sample. The maximum power of this laser diode is 50mW with the coupling loss of ~40%. On the opposite side (top), the transmitted photons were measured at the excitation wavelength through a ND filter (NE2R20A, Thorlabs), or alternatively measured at the fluorescent emission wavelength through a band-pass filter (FF01-716/40, Semrock). Both optical filters were mounted on a filter wheel. The emitted photons were first reflected by a mirror, and then detected by an EMCCD camera (Nüvü Cameras) following the filters. The field of view of the camera could cover an area of ~90 mm × ~90 mm that was sufficient to image the objects/animal presented in this paper. Before each acquisition, a ROI was chosen for the scanning of laser source. Within the ROI and using a pair of motorized linear stages (LSM100B, Zaber Technologies), both optical imaging and acoustic recording were synchronized. For the optical imaging, the laser source was scanned with 2-mm steps (X and Y); with a camera exposure time of 100ms, imaging could be completed with ~3 minutes for one wavelength. For the US imaging, a single element transducer (10 MHz, diameter 0.25″, Focus 0.46″, Olympus) was scanned on the same side as illumination with ~50 μm resolution of motor steps for each slice in the X direction but 1-mm interval in the Y direction (the notion of both X and Y directions are illustrated in the Figure 4.9). For each A-line, the US signal was averaged 300 times to improve SNR. The US acquisitions performed in this study

were completed within ~20 minutes. Both optical illumination and US imaging were conducted in a water tank. During in-vivo acquisition, the mouse laid on its belly with the body supported by an animal bed. Scanning of both the laser source and the US transducer were performed through a square hole cut on the animal bed. The square hole was indicated by the yellow square in the Figure 4.1-(b); and the view was enlarged in the Figure 4.1-(c). More, the abdomen of the mice was further held by a metal stick (diameter 2 mm) placed across the middle of this square hole, so, partly submerged in water; while the rest of the body was exposed in air, thus facing the camera. In this configuration, animal installation took less than 2 minutes. In addition, a heating device was used to keep the water temperature around 37°C; and a home-built water circulation system was used to homogenize bath temperature. In addition, a home-made electronic circuit was employed to drive the laser diode, pulse the transducer, and sample the acoustic signal via USB. To perform profilometry, a projector (PK102, Optoma) was added to project white-black stripe patterns onto the upper side of the mice to capture 3D surface information using a standard FFT profilometry technique (Takeda & Mutoh, 1983). With this technique, the 3D surface of the object could be captured within 1 second, and the height resolution was up to 1 mm. The precision of the profilometry was validated using a phantom having a semi-circle surface in a previous study (B. Li & Lesage, 2012). To confirm precision, an additional phantom with 1mm steps and total height of 15mm, was employed to characterize the profilometer in the chamber. The results demonstrated (data not shown) confirmed the 1mm resolution and each step could be identified in the contour retrieved by the profilometer. In this study, the forward model was built with 1 mm voxel resolution. The reconstruction of diffuse fluorescence imaging has a resolution of 2-3 mm (Gibson et al., 2005). Therefore, the 3D profiling might not induce further modeling errors.

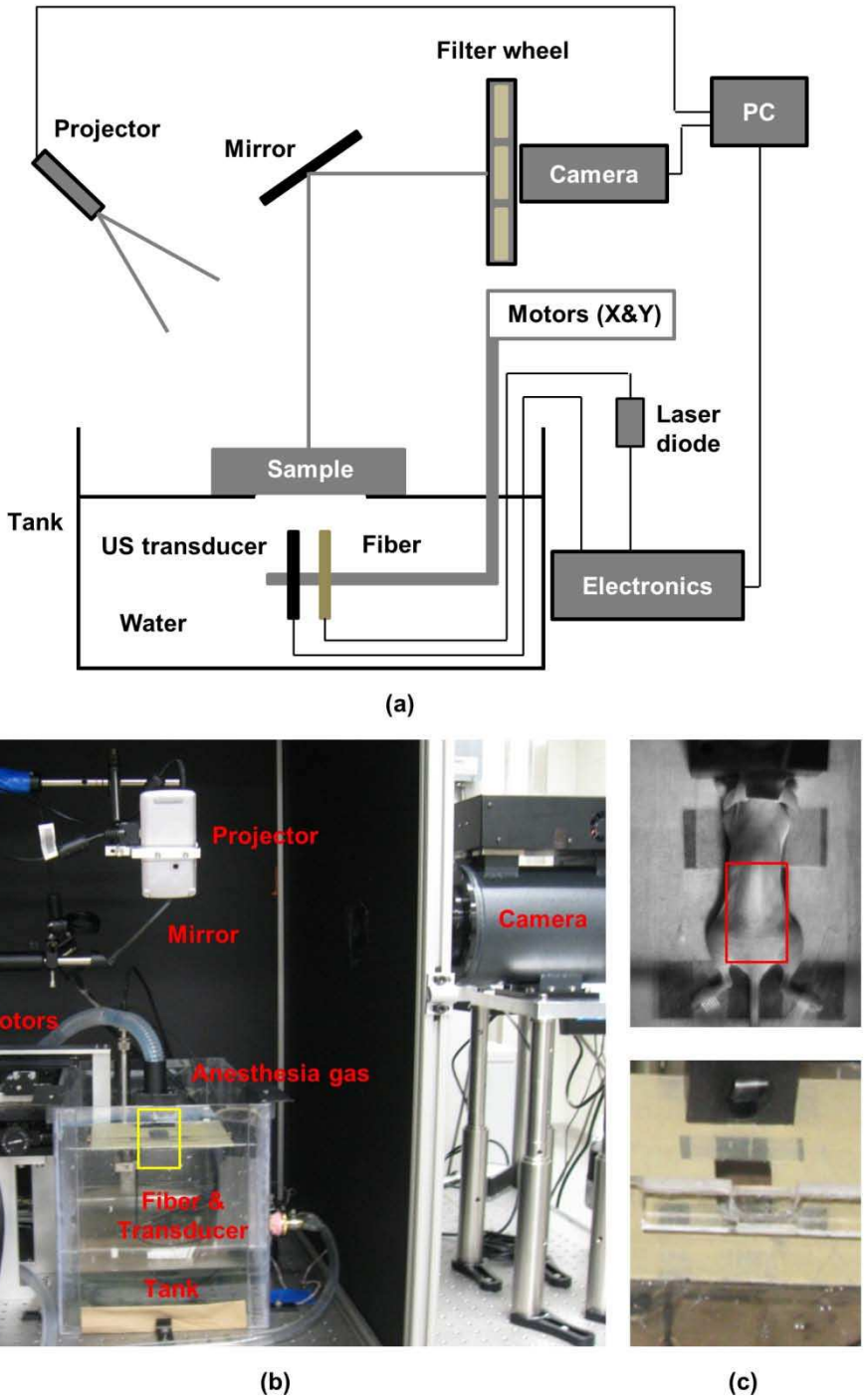

Figure 4.1: (a) System schematics of the Fluorescence-US imaging system; (b) photo of the imaging system; and the window for the scanning of both the laser source and the US transducer is indicated by the yellow square; (c) the scanning window is showed by an enlarged view; and the animal installation is also illustrated.

4.4.2 Attenuation compensated born normalization

A number of studies have reported that the BN method could be beneficial to reduce the effect of heterogeneity and cancel off experimental factors in order to gather a quantitative fluorescence dataset (Ntziachristos & Weissleder, 2001). This method was further validated in different geometries (Soubret et al., 2005; Vinegoni, Razansky, Figueiredo, Fexon, et al., 2009). However, spatial changes in scattering were shown to limit its application (Pyka, Schulz, Ale, & Ntziachristos, 2011). Moreover, fluorescence information might not be correctly extracted if the target was deeply embedded(Yuting Lin et al., 2010a). It was previously suggested that a well-built forward model could take into account scattering variations (Pyka et al., 2011); but the scattering coefficient cannot be recovered by the CW type measurement used here (Gibson et al., 2005). In this paper, a small modification termed ACBN, is proposed as an extension to the standard BN. While it remains an approximate correction, working first with a complex phantom, we show that the ACBN method may yield improved accuracy and robustness in a diffusive media with the fluorescent target embedded at different depths.

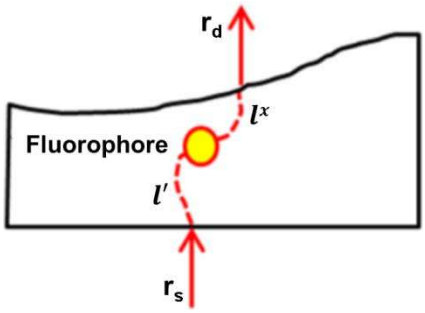

Figure 4.2: Illustration of light propagating in tissue. here, r_s and r_d represents an arbitrary source and detector position, respectively; l represents one effective traveling path of the incident light from r_s to r_d ; l' is a representative travelling path of the incident photons from r_s to fluorophore; l^x is a representative traveling path of fluorescent photons from the fluorophore to r_d .

As shown in the Figure 4.2, in the context of our current system configuration, a laser beam illuminates the surface of tissue at position r_s, and then propagates through tissue following random paths. Focusing on one such path and neglecting the amount of photons travelling along other paths, some incident photons travel along l' (indicated by the red dashed line) to the position of fluorophore. Following the Beer Lambert's law (L. V. Wang & Wu, 2007), the light intensity prior to being absorbed by the fluorophore is:

$$I' = I_0 \exp(-\mu_{ax} l') \tag{4.1}$$

where I_0 is the incident light intensity; μ_{ax} is the background absorption coefficient at the excitation wavelength. Writing the initial intensity of the excited fluorescence as:

$$I_o^{fluo} = I' A = A I_0 \exp(-\mu_{ax} l') \tag{4.2}$$

with A being the product of the extinction coefficient- ε, the quantum yield- η, and the concentration of the fluorophore-C. Thus, the detected fluorescence at r_d can be represented as:

$$I^{fluo} = Q I_0^{fluo} \exp(-\mu_{am} l^x) \tag{4.3}$$

where Q describes experimental factors, such as excitation laser power, gain and exposing time of the camera as well as coupling efficiency of the optics (filter and lens); μ_{am} is the absorption coefficient at the fluorescence emission wavelength; l^x is the traveling path of fluorescent photons from the fluorophore to r_d (indicated by the red dashed line). In the BN approximation, the detected fluorescence signal would be normalized by the photon intensity detected at the excitation wavelength which can be formulated as:

$$I^{abs} = Q I_0 \exp(-\mu_{ax} l) \tag{4.4}$$

where l is simply defined as one effective traveling path of the incident light from r_s to r_d. In BN, for both fluorescence signal and absorption signal, the distances can be viewed as effective

travelling path for the incident light in the form of a modified Beer-Lambert law. Making an assumption that $\mu_{ax} \approx \mu_{am}$, the BN method can be represented as:

$$BN = I^{fluo} / I^{abs} = A \exp(-\mu_{ax} \Delta l) \tag{4.5}$$

where $\Delta l = l - l^x - l'$ describes the difference between the effective travelling path of the incident light and that of the excited fluorescent light, which is related to the illumination/detection position and/or the localization of fluorophore.

Without a rigorous analytical analysis, the main message brought by the above simplified description is that the BN ratio may be affected by absorption/diffusion along the light propagation path and the travelling distance of the emission light. When the fluorophore is close to the detection position r_d, we may hypothesize that $l \approx l^x + l'$, thereby $BN \approx A$. When the fluorophore is localized on the surface on the detection side but far from r_d, BN would decay to zero, which still preserves the contrast for fluorescence emission. But when the fluorophore is embedded at depth, additional factors contribute and will be non-uniform across the detection plane. Moreover, the heterogeneity of the media further compromises the accuracy of the BN approximation. Therefore, an alternative correction technique is required in situations where detection is wide-field.

Preserving the simplicity of the BN approximation, we propose to include parameters to correct the distance effect in the standard BN ratio spatially according to the estimation of the relative distances between each source position and the associated detector positions. Furthermore, since accurately resolving for absorption and scattering spatially in small animals is difficult, as an intermediate solution, a normalized absorption image will be used to compensate the attenuation involved in the fluorescence signal. This so-called ACBN method is described below.

For one illumination position- r_s, the emitted photons are detected at different positions $\{r_{d1},\cdots,r_{di},\cdots,r_{dN}\}_{i=1:N}$ on the camera over the sample. A standard BN ratio image according to r_s can be represented as:

$$I_{BN} = \{I_{BN}^1,\cdots,I_{BN}^i,\cdots,I_{BN}^N\}_{i=1:N} \tag{4.6}$$

The ACBN method proposes to correct with:

$$I_{ACBN} = \{I_{BN}^1,\cdots,I_{BN}^i,\cdots,I_{BN}^N\}\cdot(I_{Norm}^{abs\ \alpha}) \tag{4.7}$$

where

$$\alpha = \{\|r_s - r_{d1}\|,\cdots,\|r_s - r_{di}\|,\cdots,\|r_s - r_{dN}\|\}_{i=1:N} \tag{4.8}$$

The spatial parameter α is the estimated distances from each source position to the associated detectors. The I_{Norm}^{abs} is the normalized absorption image with its maximum value being 1. With this correction, the experimental factors remain cancelled from the original ratios. Besides, the normalized absorption image I_{Norm}^{abs} encodes the information related to the additional attenuation effect; and, the spatially dependent parameter α, is estimated using the distances from each source to the associated detectors. Thus, the compensation term approximately corrects the term $\exp(-\mu_{ax}\Delta l)$ in the BN ratio in the equation (4.5). In this approach, the spatially dependent parameter α needs to be normalized to a given value in order to accurately recover the fluorescence emission but avoid over-correction. This point will be discussed below.

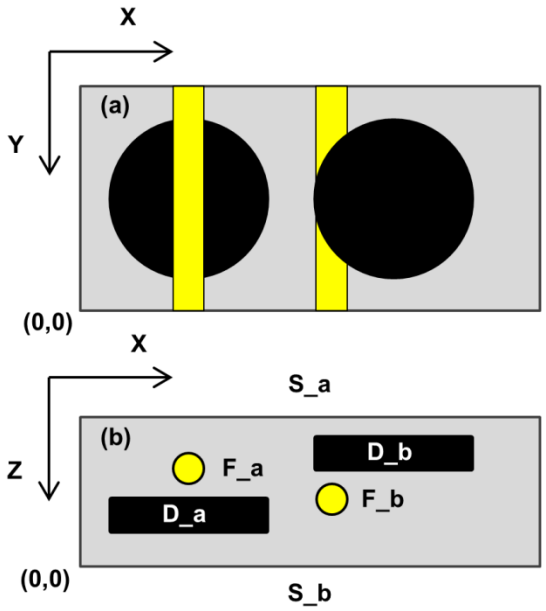

Figure 4.3: Illustration of the phantom and the inclusions. Here, S_a and S_b are the two surfaces of the phantom along the Z direction; F_a and F_b are two holes to insert the fluorescent tubes; D_a and D_b are the two heterogeneous inclusions.

Below, a series of phantom experiment was conducted to demonstrate the issue with the standard BN ratio, and then evaluate the proposed ACBN method. As illustrated in the Figure 4.3 (a), a rectangular parallelepiped phantom with two fluorescent inclusions (F_a and F_b) was used. Furthermore, two heterogeneous inclusions D_a and D_b were located above or below the two fluorescent inclusions, respectively. The dimension and the optical properties of this phantom are detailed in the Table 4.1.

Table 4.1: Dimension and optical properties of phantom.

Inclusion	Center position (mm)			Dimension (mm)				Optical properties (mm^{-1})	
	X	Y	Z	Diameter	X	Y	Z	μ_α	$\mu_s^{'}$
Bulk	--	--	--	--	61	30	20	0.02	1.0
D_a	13	15	7	18	--	--	6	0.005	0.5
D_b	39	15	15	18	--	--	6	0.04	2.0
F_a	14	--	13	4	--	30	--	--	--
F_b	32	--	9	4	--	30	--	--	--

A fluorescent tube filled with 100nM Cy5.5 was inserted successively into the hole F_a or F_b of the phantom. Then, imaging was performed with illumination on S_a or S_b separately, to gather a series of data representing the different situations that may occur experimentally. The experiment is explained in the Table 4.2, which gave four different scenarios with respect to fluorescent target localization (F_a or F_b) and the illumination/detection side (S_a or S_b). The raw data with the ACBN processing are presented in the Figure 4.4 showcasing the discussion above. The first row of images in the Figure 4.4 shows the ROI for each case. As denoted by the dots, each scan was conducted with 2-mm steps for source positions in X and Y directions. For each image, the bar crossing the phantom along the Y direction represents the horizontal location of the fluorescent tube. To compare uniformly, the same laser power and camera configuration were used for all scans. And to avoid boundary effect, the edge of the phantom was covered by black tape in experiment.

Table 4.2: Four cases of the experiment.

	Fluorescent tube localization	**Illumination side**	**Detection side**
Case #1	F_a	S_b	S_a
Case #2	F_a	S_a	S_b
Case #3	F_b	S_b	S_a
Case #4	F_b	S_a	S_b

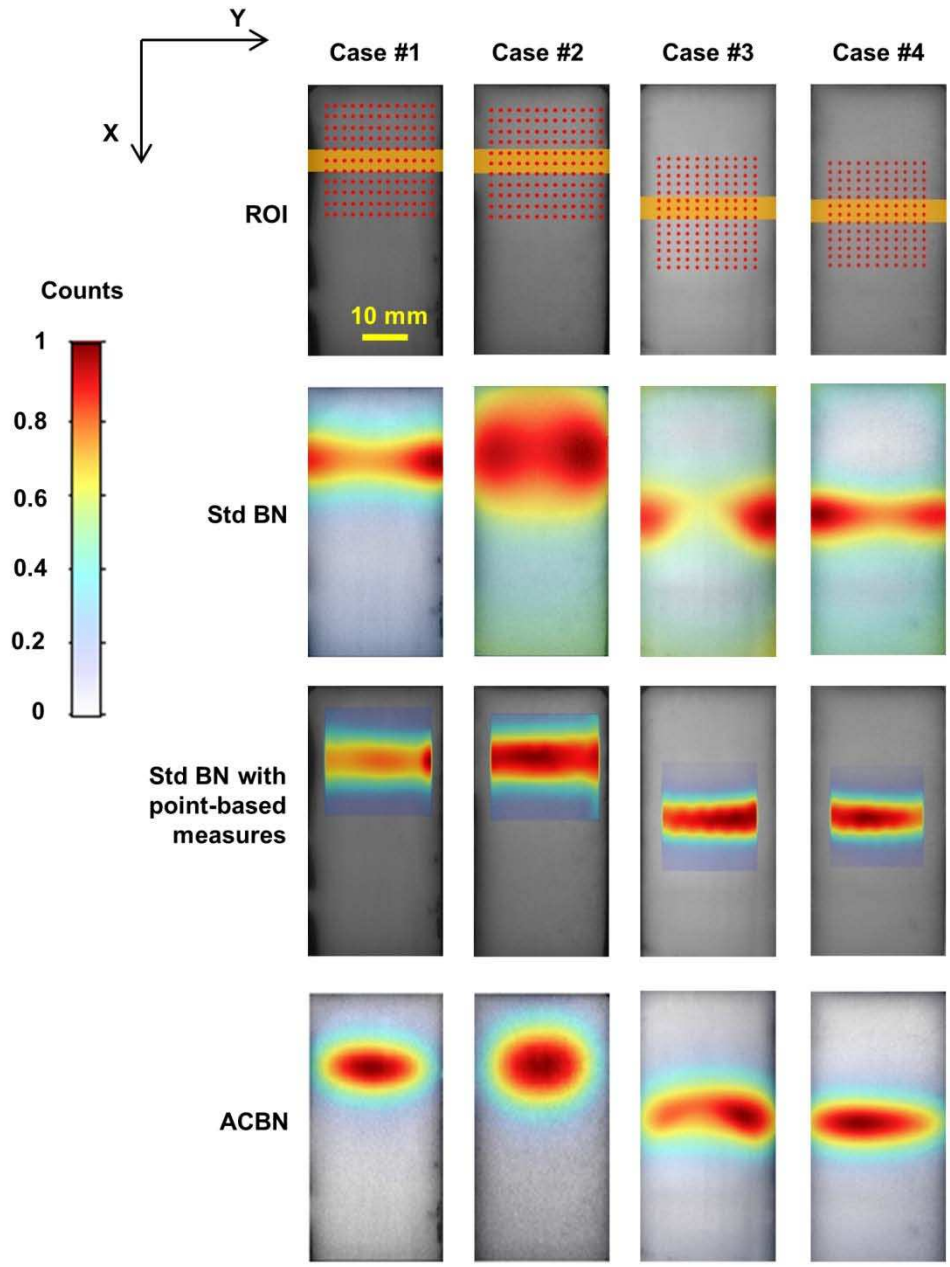

Figure 4.4: Phantom images for the four cases: the first row shows the ROI for each scan; the second row shows the fluorescence images processed with the standard BN method; the third row shows the standard BN ratio images with only the measurement of the detector co-linear with the source; finally, the fourth row shows the fluorescence images processed with the ACBN method.

The second row in the Figure 4.4 shows the images processed with the standard BN method for the four cases. Each image is the summation of images for all the source positions and normalized with its maximum value being 1. When the object was deeply embedded, we observed that the fluorescence emission map recovered by the standard BN does not reflect the 2D mapping of the fluorescent object in the phantom, hence might not provide adequate data for reconstruction using wide-field techniques, showcasing the necessity for attenuation correction.

In addition, as mentioned above, the distance effect will also affect the BN ratio. To verify this, for each source we kept only the measurement of the detector co-linear with the source. The result is shown in the third row of the Figure 4.4. Comparing with the BN ratio images shown in the second row of the Figure 4.4, by selecting the measurement being co-linear with the source, the standard BN method accurately recovered the fluorescence emission illustrating the distance effect involved in the BN ratio. In a wide-field detection scheme, it is essential to control this effect.

The fourth row of the Figure 4.4 shows that the proposed ACBN correction. This time, each image is the summation of images for all the source positions (i.e. all detector positions were kept). When the fluorescent inclusions (F_a or F_b) were closer to the detection side than the inclusions (D_a or D_b) were, e.g. case #1 and case #4, the emitted fluorescence could be accurately recovered by the ACBN method. However, when the inclusions (D_a or D_b) were closer to the detection side than the fluorescent inclusions (F_a or F_b) were, e.g. case #2 and case #3, the emitted fluorescence went through the inclusion D_a or D_b (different μ_α and μ_s') prior to being detected. In this condition, the ACBN method was also affected displaying its limitations. For example, in the case #2, because D_a has smaller μ_α and μ_s' than the bulk properties, the ACBN ratio image appears larger than the fluorescent tube does. And in case #3,

because the fluorescent tube is horizontally located near the edge of D_b and the D_b has a greater μ_α and μ_s' than the bulk properties, the fluorescent emission was non-uniformly absorbed by D_b along the tube, hence shows a curved shape.

As discussed above, the parameter α needs to be normalized to a proper value for an accurate recovery of the fluorescence emission without over-correction. Herein, it is suggested that the normalization value is determined by the ratio between the distance from the center of the fluorescent object to the detection plane and the distance from the center of the fluorescent object to the illumination plane. However, to analyze the reconstruction results in a consistent manner, we kept using the same normalization value for the spatial parameter α in each series of experiment. Specifically, in the phantom experiment, after estimating the distance ratio in this phantom experiment (illustrated in the Figure 4.3), the spatial parameter α was normalized to be 1 for the Case #1 – #4. It should be kept in mind that for the in-vivo case, fluorescence may originate from a broad area (e.g. liver, kidney, lesion, and so on); but in this paper we would regard the lesion (i.e. tumour in this study) as the main fluorescent target for estimating the distance ratio for normalizing the parameter α. Following a similar procedure, for the in-vivo experiment, the parameter α was normalized to be 4, which could be estimated from the segmentation of the US image, as shown in the Figure 4.5 (a).

Overall, in this phantom study, an improvement could be observed with the ACBN method in comparison to the standard BN method. Amongst the four cases investigated, if the fluorescent object was located on the detection side, e.g. case #1 and case #4, which meant the transmitted fluorescence did not go through the inclusion D_a or D_b, the ACBN could compensate the attenuation and recover the fluorescence emission. Otherwise, the inclusion D_a or D_b deformed the shape of the fluorescence emission, e.g. case #2 and case #3. This is most

likely due to the fact that the collected photons for each source position went through non-uniform absorption and scattering. To quantify the benefit of the ACBN method over the standard BN, contrast was computed for all the cases. Here, the contrast is defined as $(S_A-S_B)/S_B$. As illustrated in the first row of the Figure 4.4, S_A and S_B is the mean intensity of each image within the fluorescent tube area and the background area, respectively. As a result, on average, the contrast of the ACBN images is 2.5 times higher than that of the standard BN images in this wide-field configuration. In the next sub-section, we will further validate the benefit of the ACBN method in the pattern-based reconstruction mechanism.

4.4.3 Reconstruction

4.4.3.1 Pattern-based forward modeling

Below, we describe a reconstruction algorithm to recover fluorescent yield using patterns on the detection side. It has been reported that by performing singular-value decomposition, the dimension of the forward problem could be reduced to keep the important components of the measurement required for reconstruction as well as avoid heavy computations associated with the large number of detection points (J. Chen, Venugopal, Lesage, & Intes, 2010; Markel et al., 2003). In separate work, we showed that by directly projecting a series of patterns with different spatial frequencies onto a sample, one could implement dimension reduction during acquisition to achieve a high imaging through-put (Bélanger, Abran, Intes, Casanova, & Lesage, 2010). In a previous study, this pattern-based simulation was employed for the detection part while keeping the traditional point-based simulation for the illumination (B. Li & Lesage, 2012). However, all these studies used rectangular geometry.

Here, we incorporated the ACBN method and the combined structural prior (discussed below) into the forward problem and then employed the pattern-based simulation for photons

propagation. Since the primary information lies in low frequency components (Venugopal, Chen, Lesage, & Intes, 2010), 18 low-frequency sinusoidal patterns were chosen for each detected image. A GPGPU-based Monte Carlo program was then used for the forward problem (Fang & Boas, 2009). Finally, benefitting from the combined structural prior, we applied the Monte Carlo simulation in the curved geometry with analytically guided choice of patterns to develop a new mechanism to perform reconstruction.

4.4.3.2 A combined structural prior

In a previous study, the US image was used to specify the domain for the forward modeling and was also used as a regularizer for the inverse problem (B. Li et al., 2011). However, with a fixed focal distance, a single element US transducer could not recover the tissue boundary at the opposite side of sample. To measure geometrical information, a FFT profilometer was used here to recover the top boundary of the tissue (Takeda & Mutoh, 1983); while the US imaging was used to image the fluorescent target (i.e. lesion, tumor) as well as recover the tissue boundary on the laser source side (bottom). Therefore, the surface information retrieved separately by the profilometer and the US imaging was concatenated, which results in a precise definition of the problem domain for the simulation of photons propagation; and the anatomy of the lesion recovered by the US imaging was used to constrain the reconstruction as a soft prior (Yalavarthy, Pogue, Dehghani, Carpenter, et al., 2007). This combined structural prior was achieved without increasing acquisition time.

4.4.3.3 Inverse problem

The computation aimed to minimize the following objective function:

$$\Omega = \{\left\|\Phi^{meas} - W\chi\right\|^2 + \lambda\left\|L\chi\right\|^2\} \tag{4.9}$$

taking the first-order derivative with respect to χ led to the update equation:

$$\chi_{i+1} = [W^T W + \lambda L^T L]^{-1} W^T (\Phi_i^{meas} - \Phi_i^C) + \chi_i \tag{4.10}$$

where

$$W = \frac{\int_v G^m(Pattern, r) G^x(r_s, r) d^3 r}{\Phi^x(r_s, Pattern)} [\Phi^{x-Norm}(r_s, Pattern)\hat{}\,\alpha] \tag{4.11}$$

The detail of the equation derivation could be found elsewhere (Yalavarthy, Pogue, Dehghani, & Paulsen, 2007). Here, the symbol Φ^{meas} is the experiment measurement, in our case, the fluorescence data processed by the ACBN method; Φ^C is the simulated measurement; W is the sensitivity matrix obtained from Monte-Carlo simulations; χ represents the fluorescence yield $\varepsilon\eta C$; i represents the iteration index; L is a Laplacian form matrix encoding the prior information of the lesion (Yalavarthy, Pogue, Dehghani, & Paulsen, 2007); λ is the regularization parameter, of which the value might be determined by the data-model misfit but often empirically (Yalavarthy, Pogue, Dehghani, & Paulsen, 2007). Its value was updated according to the projection error in each iteration (Srinivasan et al., 2004). Convergence was defined to be reached when the change in projection error between two iterations was less than 1%, or, within a maximum of eight iterations pre-set to prevent the estimating error from increasing (Yalavarthy, Pogue, Dehghani, & Paulsen, 2007).

4.4.4 Simulations

To evaluate the proposed reconstruction mechanism, a simulation study was conducted. Here, photon propagation was simulated in a volume that was created based on the mouse Tumor #1 (discussed in the section 4). As a representative image slice shown in the Figure 4.5 (a), the volume was segmented into 4 regions with 1-mm voxel resolution: air, water, tissue, and tumour.

Benefiting from the combined structural prior, the sensitivity matrix could be computed in a well-defined space; and a Laplacian form matrix was used to constrain the reconstruction as a soft prior (Yalavarthy, Pogue, Dehghani, & Paulsen, 2007); plus, the air and water regions were excluded from the inverse problem, which helped reduce the ill-posedness and thus enabled a more accurate reconstruction (discussed later but confirmed by simulations in the Figure 4.5 (c)).

In simulation, photons were launched to the belly side on a point-point basis; detection was performed from the back side guided by patterns. Average optical properties were used for the entire tissue region (μ_a=0.05 mm^{-1}; μ_s'=2.3 mm^{-1}) (Chaudhari et al., 2005). And the spatial parameter α was normalized to 4, same as the reconstructions performed with the in-vivo measurements below. For assessment, reconstruction accuracy was defined as the ratio between the averaged reconstructed value-$\varepsilon\eta$C and the true value.

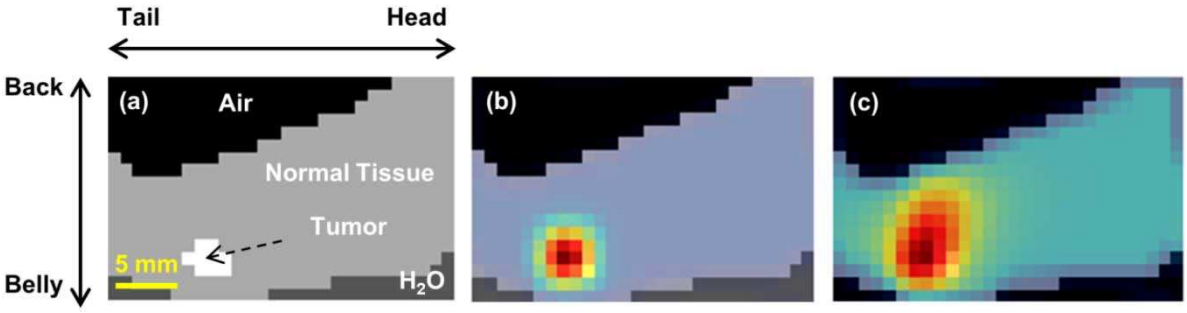

Figure 4.5: Representative image slices. (a) The segmentation of tissue types derived from the combined structural prior; (b) the localization was accurately reconstructed with prior; (c) reconstruction without structural prior.

As discussed above, both the ACBN processing and patterns-measurement integration were incorporated in the sensitivity matrix. With the sensitivity matrix, measurement was simulated, which leads to the following discussion. In this simulation study, different noise level was added to the simulated measurement after the integration between the sensitivity matrix and

the fluorescent field of the volume. Different scenarios were investigated. For every case, the reconstruction started from the same homogeneous initial estimate of $\varepsilon\eta C=5\times10^{-4}$. In the first case (1), a 3D volume was assigned nine different values of $\varepsilon\eta C$ (true values) to the tumor region, ranging from 3×10^{-3} to 19×10^{-3} with 2×10^{-3} interval, respectively, and a constant value of $\varepsilon\eta C=1\times10$-3 was assigned to the normal tissue region. Measures were simulated based on the image volumes, separately. A noise level of 10% was added to each set of measurement. 3D reconstructions were done using the update equation (4.9). The reconstructed $\varepsilon\eta C$ in the tumor region is shown in the Figure 4.6 (a). The X axis represents the true value of $\varepsilon\eta C$; the Y axis represents the reconstructed value. The averaged accuracy was 86%. For the background (normal tissue region), the perturbation of reconstruction amongst different initial estimates was larger; but the average accuracy was as good as 71%.

In the second case (2), we varied the initial estimate but kept the true value constant. Specifically, eleven different sets of initial estimate of $\varepsilon\eta C$ varying from 0.1×10^{-3} to 10×10^{-3} were used. While, the true value of $\varepsilon\eta C$ in the tumor region and normal tissue region were kept at 5×10^{-3} and 1×10^{-3}, respectively. Noise at a level of 10% was added to each set of measurements. The Figure 4.6 (b) shows that the averaged accuracy for the tumor region and the background was 88% and 87%, respectively.

In the third case (3), the true value of $\varepsilon\eta C$ was varied in both tissue regions. Here the true value of $\varepsilon\eta C$ was varied in the background ranging from 0.5×10^{-3} to 5×10^{-3} with an identical interval 0.5×10^{-3}. And the true value in the tumor region was constantly 4 times greater than that of background. Again, 5×10^{-4} was used as the initial estimate. For each simulated measurement, again, 10% noise was added. In the Figure 4.6 (c), it shows that the averaged ratio between the

reconstruction of the tumor region and that of background was 2.9, which is ~73% of the true ratio.

In the fourth case (4), the true values in the tumor region and background were kept constant as 5×10^{-4} and 1×10^{-3}, respectively and the initial estimate was still kept at 5×10^{-4}. Here, we varied the noise level from 5% to 50%. The Figure 4.6 (d) shows that the accuracy slightly drops down with increasing noise level, but maintained an average of 85%. For the background, because the true value of fluorescence level assigned is lower than that of the tumor region, the reconstruction in that region was more sensitive to noise. As a consequence, the averaged accuracy in background was 55%.

Overall, the reconstruction accuracy in the tumor region was as good as ~86% at the worst case using a coarse volume for the inverse problem with a noise level of 10%. The reconstruction in the normal tissue region had lower accuracy due to its smaller fluorescence level, thus being more sensitive to noise. In addition, the reconstruction in the background was typically overestimated because the embedded tumor region bleeding signals to the background. Even with priors, the fluorescence in the tumour region was underestimated and appeared larger in size in comparison to the segmented region. In all the cases, guided by the combined structural prior, the lesion localization was accurately reconstructed, which is shown in the Figure 4.5 (b). As a comparison, a reconstructed image slice without any prior is presented in the Figure 4.5 (c), which shows a deteriorated localization; besides, the reconstruction accuracy of the tumour region was ~60%, i.e. ~26% worse than the one with prior (Figure 4.6 (b)). Most importantly, linearity was achieved in all the simulation cases. Hence, quantification with in-vivo data may be possible.

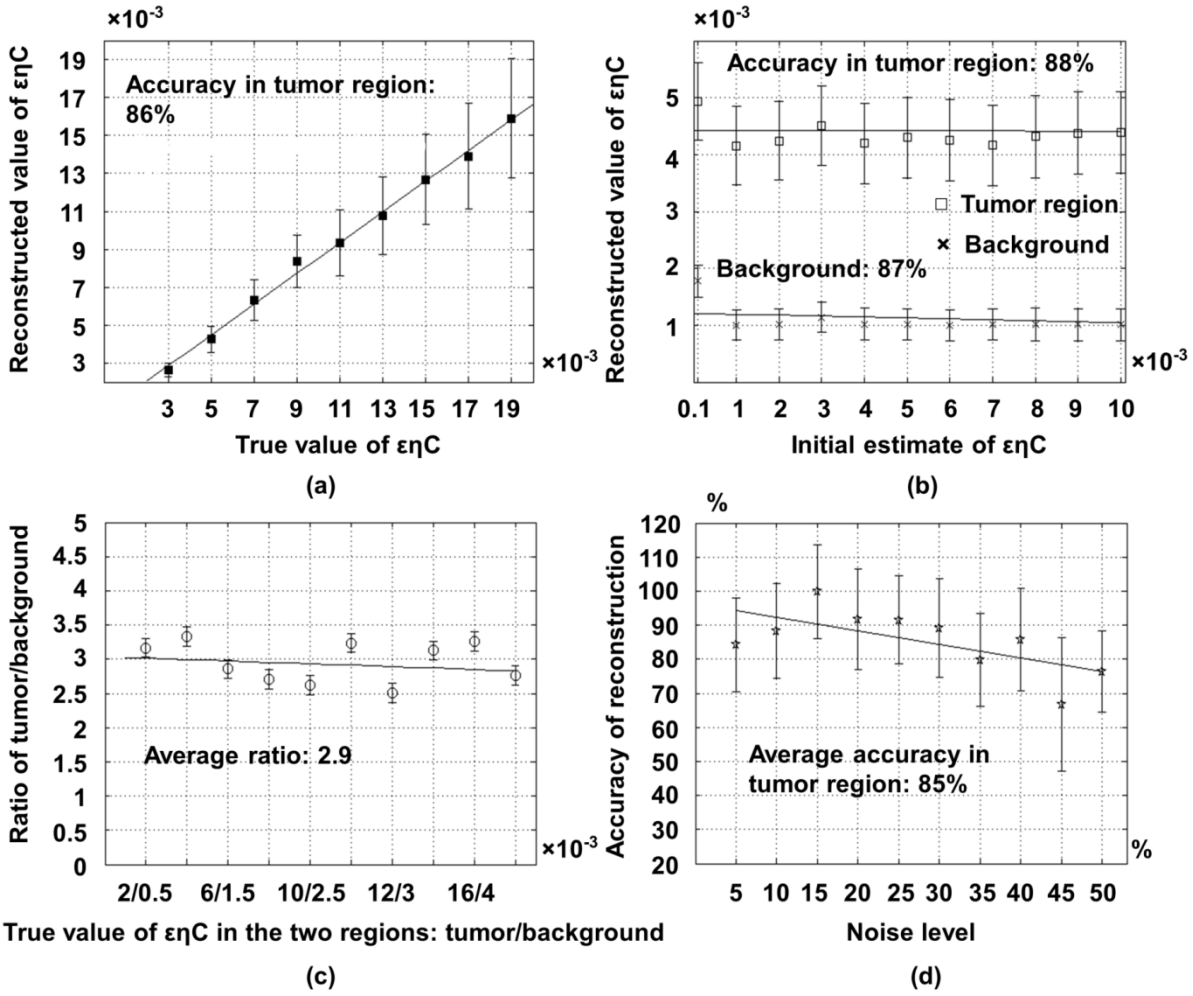

Figure 4.6: (a) The true value of εηC only in the tumor region was changed; but the initial estimate was kept constant; (b) the true value of εηC was constant; but the initial estimate was changed; (c) the true values of εηC in both tissue regions were changed; and the value of the tumor region remained 4 times greater than that of the normal tissue region; but the but the initial estimate was kept constant; (d) true values in both tissue-type regions were constant, and the initial estimate was constant too. The reconstructed was assessed with different noise levels.

4.4.5 Phantom reconstruction

Following the previous discussion, here we evaluate the ACBN method associated with the pattern-based reconstruction using the phantom measurement. As mentioned, we inserted the

same fluorescent tube into the holes F_a and F_b, respectively, and imaged the phantom in four separate cases by rotating the phantom by 180 degrees. Theoretically, the reconstruction, in these four cases, would recover the fluorescence field identically. Photons were simulated in a homogeneous media using the bulk optical properties; this is because that the US system could not separate the heterogeneous inclusions from the bulk but only the fluorescent tube; additionally it mimics the in-vivo situation, in which some organs could not be clearly separated from the body.

As detailed in the previous section, the emitted photons would go through different absorption and scattering events among the four cases. As shown in the Figure 4.7, the reconstructed field of the Case #1 has the greatest value because the photons travelling path in that case was subject to less absorption and scattering; in Case #2, due to the diffusion of the detected fluorescence emission (Figure 4.4), the reconstructed field was underestimated by the pattern-based reconstruction algorithm; in the Case #3 and Case #4, because of the inclusion D_b was located below (Case #3) and above (Case #4) the fluorescent tube, the reconstructed field was also underestimated to a different extent. However, Figure 4.7 shows that the reconstruction with measurement corrected by the ACBN method displayed a better consistency than the one with the standard BN method. The standard deviation of the reconstructions with the ACBN method was 0.15, less than the standard BN equivalent of 0.36. This phantom study indicates that the ACBN method might be beneficial and necessary when using wide-field fluorescence imaging geometries, in which case the fluorescence emission mapping of the raw data would affect the reconstruction.

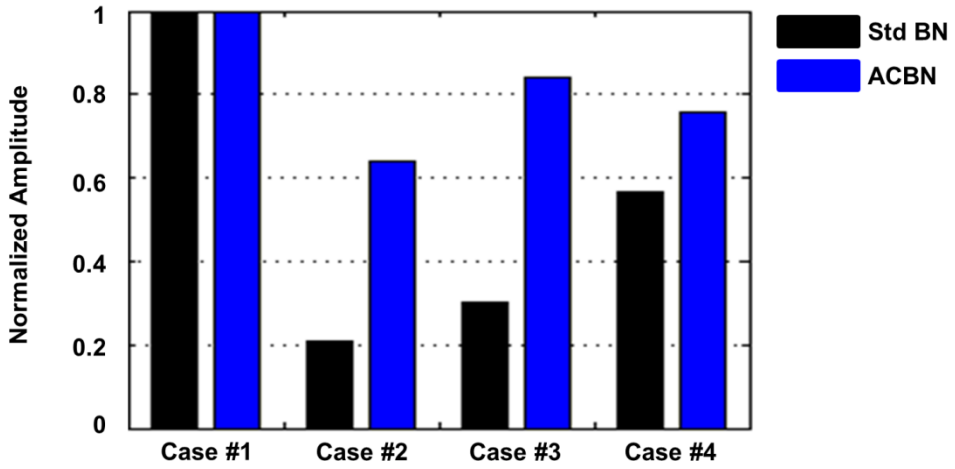

Figure 4.7: The comparison of the reconstruction between the ACBN method and the standard BN method.

4.5 Experiment

With the imaging system and the associated reconstruction mechanism described previously, a study was targeted at preclinical tumor model to quantify fluorescence emission from tumors. Three nude mice were employed. One of them was used as control. The two remaining mice, denoted as Tumor #1 and Tumor #2, were injected with MDA-MB-231 tumour cells to subcutaneously implant human lung cancer to the mammary fat pad. A representative model is shown in the Figure 4.8. Imaging was done 3-4 weeks after the injection of the tumour cells.

Figure 4.8: As a representative, the tumor is approximately indicated by the dashed circle.

For molecular imaging, a molecular probe IntegriSense™ 680 (PerkinElmer) was employed. This probe enabled imaging tumor cells by monitoring the integrin $\alpha_v\beta_3$ expression. As recommended, ~2 n mol of this probe was intravenously administrated for each mouse.

In experiments, the mice laid on the belly with their back facing the camera. So, part of the belly was submerged in water in order to couple acoustic pulse-echoes. In acquisitions, the same camera configuration was used for every optical imaging session. Due to variations in tissue thickness, a pre-scan was done to determine laser power for each illumination point in order to maintain a good SNR and avoid camera saturation. The pre-evaluated laser power sequence was used for absorption and fluorescence imaging, with a maximum laser power of 17 mW illuminated on an area of ~1 mm^2. Each imaging session, including optical and US imaging, was finished within 40 minutes. During the experiment, mice body temperature was kept around 37°C supported by the home-built water circulation system. All animal manipulations were approved by the ethics committee of Montreal Heart Institute.

4.6 Results

4.6.1 Fluorescence imaging with the ACBN method

In the Figure 4.9, the fluorescence images processed with the ACBN method are presented. Each image is the summation of images for all the source scans. Again, as explained above, we chose the value of 4 to normalize the spatial parameter α involved in the ACBN ratio. In the Figure 4.9, every image was normalized to 255. As shown in the Figure 4.9 (a), the laser source was scanned on the points denoted by the dots with 2-mm steps along the X and Y directions. The US transducer was scanned over the same ROI with ~50 μm resolution in the X direction, but 1 mm interval in the Y direction. The dimension of the ROI was about 28 mm × 22 mm for the X and Y direction, respectively. The first row of the Figure 4.9 (b), (d) and (f) shows the images

acquired prior to the injection of the molecular probe. The second row of the Figure 4.9 (c), (e) and (g) shows the images acquired 24 hours after the injection. Fluorescence was clearly seen in post-injection scans with some signal localized in excretion organs (kidneys). And as seen in the Figure 4.8, the fluorescence emission was mostly located in the tumor area for both diseased mice while the control one did not show specific fluorescence signal.

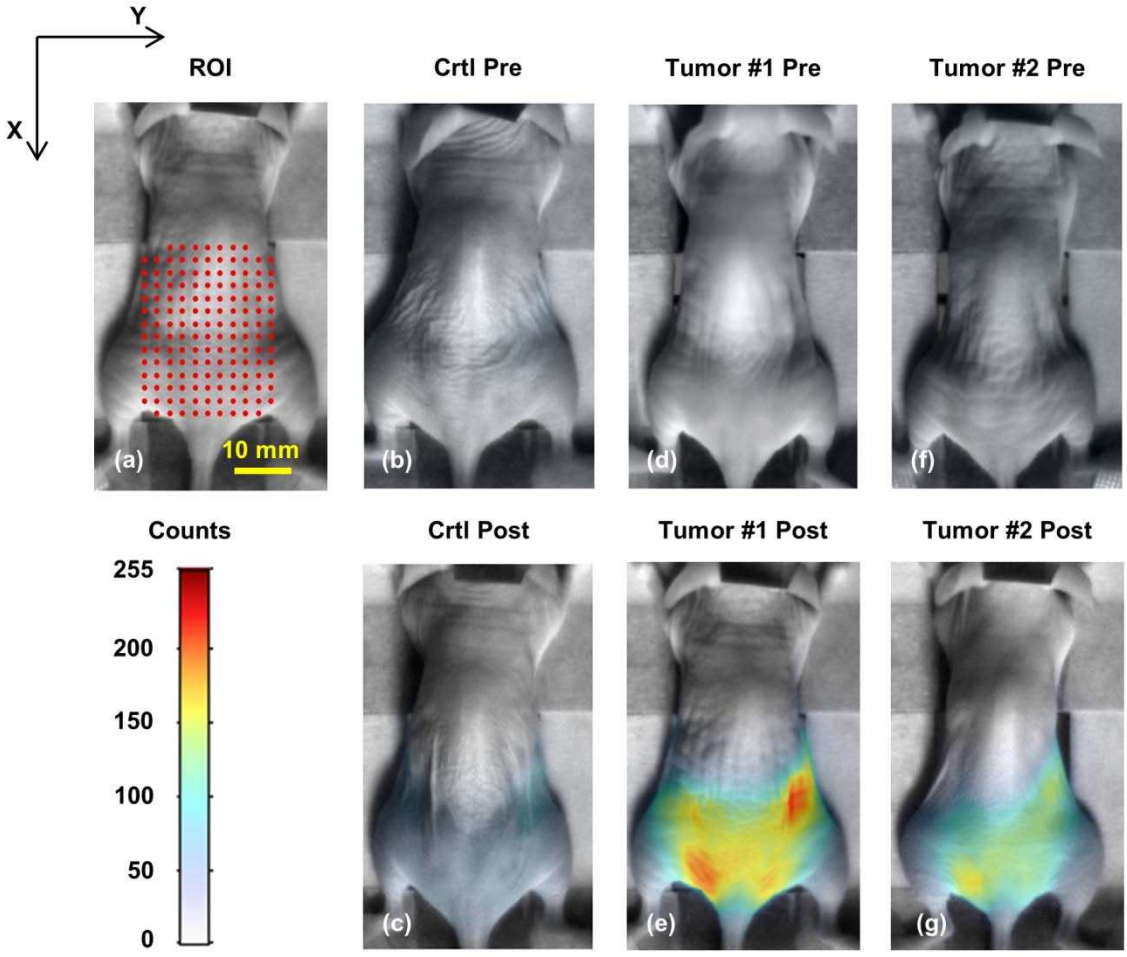

Figure 4.9: (a) The ROI of imaging was indicated by the red spots; (b)-(c) the fluorescence images acquired before and after injection of the molecular probe for the control; (d)-(e) the fluorescence images acquired before and after injection of the molecular probe for Tumor #1; (f)-

(g) the fluorescence images acquired before and after injection of the molecular probe for Tumor #2.

4.6.2 Reconstruction results

The reconstruction of εηC is shown in the Figure 4.10. In the reconstruction, homogeneous global optical properties (μ_α =0.05 mm^{-1}; μ_s' =2.3 mm^{-1}) were used for both excitation wavelength and emission wavelength to generate forward models (Chaudhari et al., 2005). In the inverse problem, all reconstructions started from the identical homogenous initial value of $\varepsilon\eta C=5\times10^{-4}$. As illustrated in the Figure 4.9 (a), the US image slice was along the X direction and around the center of tumor in the Y direction. Guided by the combined structural prior to recover geometry and build a soft prior for the tumor, the results show that the localization of tumor was accurately reconstructed. As reported in Ref. (Yalavarthy, Pogue, Dehghani, Carpenter, et al., 2007), this soft prior approach helps regulate the inverse problem while remaining somewhat immune to the prior uncertainty. In addition, as indicated by the dashed square in the Figure 4.10 (a), an artifact occurred in all the US images shown in the Figure 4.10. This was caused by the metal stick, which was placed across the square hole of the animal bed along the Y direction in order to prevent the body from sinking in water.

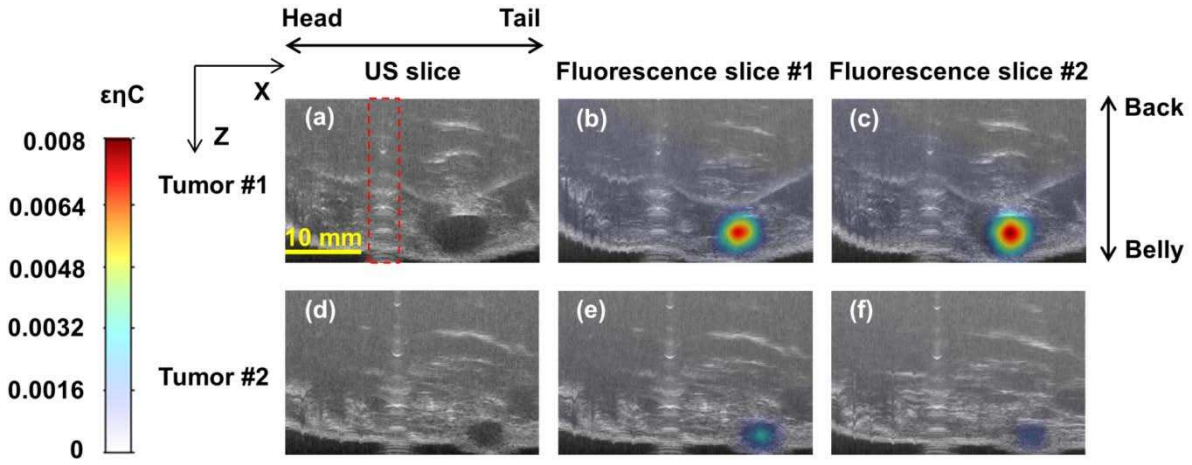

Figure 4.10: (a)-(c) For Tumor #1, a representative US image slice and two representative fluorescence images overlaid the corresponding US image slices are shown; (d)-(f) For Tumor #2, a representative US image slice and two representative fluorescence images overlaid the corresponding US image slices are shown.

To analyze the reconstructions, the CNR was computed for all the reconstructed images. Here, the CNR is defined as $(S_A-S_B)/\sigma$, where S_A and S_B are the mean intensities of the reconstructed fluorescence yield εηC for the tumour region and the normal tissue region, respectively; and σ is the standard deviation for the normal tissue region. As a result, the CNRs were over 40 for all cases.

4.6.3 Ex-vivo evaluation

Ex-vivo imaging for the mice Tumor #1 and Tumor #2 was conducted in reflection mode using a commercial fluorescence imaging system (IVIS Lumina II, Caliper Life Sciences). The ex-vivo images were normalized to 1 and are shown in the Figure 4.11 (a). As a reference of the H_2O image, the emitted fluorescence from the tumors could be clearly observed. The ratio between the maximum signal amplitude of Tumor #1 and that of Tumor #2 was 1:0.61. As shown in the Figure 4.11 (b), the normalized reconstructed εηC of the tumor region for the mice Tumor #1 and

Tumor #2 is also provided. The ratio between the maximum signal amplitude of Tumor #1 and that of Tumor #2 was 1:0.19 with the ACBN method, but 1:0.09 with the standard BN method showing a better agreement of ACBN to the ex-vivo analysis.

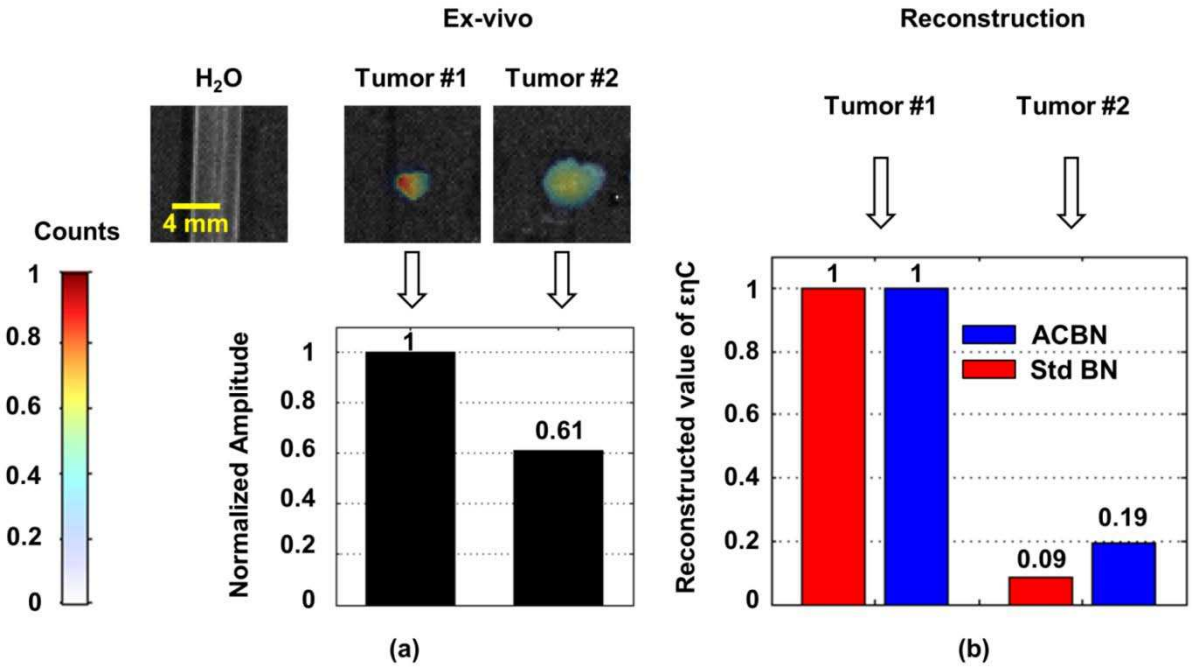

Figure 4.11: (a) Ex-vivo images of the tumors for Tumor #1 and Tumor #2. The ratio between the maximum reconstructed εηC of Tumor #1 and that of Tumor #2 is 1:0.61; (b) the maximum reconstructed εηC for Tumor #1 and Tumor #2 is shown with the ACBN method as well as the standard BN method.

However, the remaining difference between the reconstruction and the ex-vivo analysis also exposed the limitations of the ACBN method due to the unknown optical properties of the imaged objects. It should be kept in mind that the unknown optical properties for different tissue types might induce the following issues: (1) Typically, tumor is a blood enriched region because of angiogenesis (Hoffman, 2002), which implies being more absorbing than the surrounding tissue (Alexandrakis et al., 2005). Therefore, using the same homogenous optical properties for all the mice having different tumor sizes results in reconstruction inaccuracies. (2) Because the

anatomical resolution of US image is limited, some organs remain difficult to segment. Thus using literature optical properties (Alexandrakis et al., 2005) (which in turn may not reflect the in-vivo situation) could not be accurately assigned for different organs to perform a more precise forward modeling.

4.7 Discussion

In this paper, a dual-modality Fluorescence-US molecular imaging system was presented. Using an EMCCD camera associated with the point-based illumination, transmission imaging could be conducted for both fluorescence and absorption imaging. Compared with our previous study (B. Li et al., 2011), both optical imaging and US imaging were optimized in terms of acquisition speed and sampling precision. The 3D surfaces derived from both US imaging and profilometer, respectively, was concatenated to extract an adequate boundary, which resulted in a precise separation between tissue and air/water, hence benefiting the forward modeling and inverse problem. In addition, we amended the BN method to compensate the attenuation involved in the BN approximation. With the ACBN method, fluorescence emission mapping was accurately recovered in phantom using wide-field detection. Finally, to take advantage of the enriched measurements on the detection side, a pattern-based reconstruction mechanism was employed showing accurate recovery of fluorescence information. A simulation study further demonstrated linearity, accuracy and fidelity of this reconstruction mechanism; following, using the phantom measurement again, an enhanced quantification of reconstruction was achieved with the ACBN method.

The system was then applied in the in-vivo study with preclinical tumor model. Following injection of the molecular probe, specific fluorescence signal could be observed emitting from the tumor area. In addition, the simulated benefit of the reconstruction mechanism

was maintained with the in-vivo measurements: First (1), the localization of lesion was accurately reconstructed. On the other hand (2), the quantitative reconstruction of the mice Tumor #1 and Tumor #2 was in agreement with the ex-vivo result. Finally, CNRs of over ~40 were achieved for all the cases.

However, limitations remain. First, as shown in the phantom results, variation of absorption and scattering along the fluorescence propagation path compromised the accuracy of the ACBN method. One potential solution would be to take into account only the measurement relatively close to illumination, which, nonetheless, might lose some important information of the experimental data. Second, the limited organ contrast of US images challenged obtaining a precise segmentation. Because different organs contours were hardly identified from the US images, literature optical properties (Alexandrakis et al., 2005) could not be utilized, which would have helped achieve a more precise forward model. An alternative would be to employ time-domain measurement which could enable reconstructing optical properties (Lam, Lesage, & Intes, 2005; Venugopal, Chen, Lesage, et al., 2010).

4.8 Conclusion

In conclusion, we have explored the benefit of dual-modality Fluorescence-US molecular imaging system associated with the reconstruction mechanism could contribute to in-vivo imaging study with mice. Future work would be to extend the application to cardiovascular disease for small animals.

4.9 Acknowledgments

This study has been funded by a Canadian Institutes of Health Research Catalyst grant (107765) to F. Lesage. B. Li is supported by China Scholarship Council and F. Lesage.

4.10 References

Aikawa, E., Nahrendorf, M., Sosnovik, D., Lok, V. M., Jaffer, F. A., Aikawa, M., & Weissleder, R. (2007). Multimodality Molecular Imaging Identifies Proteolytic and Osteogenic Activities in Early Aortic Valve Disease. Circulation, 115(3), 377–386. doi:10.1161/CIRCULATIONAHA.106.654913

Ale, A., Ermolayev, V., Herzog, E., Cohrs, C., de Angelis, M. H., & Ntziachristos, V. (2012). FMT-XCT: in vivo animal studies with hybrid fluorescence molecular tomography-X-ray computed tomography. Nature Methods, 9(6), 615–620. doi:10.1038/nmeth.2014

Ale, A., Schulz, R. B., Sarantopoulos, A., & Ntziachristos, V. (2010). Imaging performance of a hybrid x-ray computed tomography-fluorescence molecular tomography system using priors. Medical Physics, 37(5), 1976–1986.

Alexandrakis, G., Rannou, F. R., & Chatziioannou, A. F. (2005). Tomographic bioluminescence imaging by use of a combined optical-PET (OPET) system: a computer simulation feasibility study. Physics in Medicine and Biology, 50(17), 4225–4241. doi:10.1088/0031-9155/50/17/021

Bélanger, S., Abran, M., Intes, X., Casanova, C., & Lesage, F. (2010). Real-time diffuse optical tomography based on structured illumination. Journal of Biomedical Optics, 15(1), 016006. doi:10.1117/1.3290818

Brooksby, B. A., Dehghani, H., Pogue, B. W., & Paulsen, K. D. (2003). Near-infrared (NIR) tomography breast image reconstruction with a priori structural information from MRI: algorithm development for reconstructing heterogeneities. Selected Topics in Quantum Electronics, IEEE Journal of, 9(2), 199–209. doi:10.1109/JSTQE.2003.813304

Chaudhari, A. J., Darvas, F., Bading, J. R., Moats, R. A., Conti, P. S., Smith, D. J., … Leahy, R. M. (2005). Hyperspectral and multispectral bioluminescence optical tomography for small animal imaging. Physics in Medicine and Biology, 50(23), 5421–5441.

Chen, J., Venugopal, V., Lesage, F., & Intes, X. (2010). Time-resolved diffuse optical tomography with patterned-light illumination and detection. Optics Letters, 35(13), 2121–2123. doi:10.1364/OL.35.002121

D'Andrea, C., Ducros, N., Bassi, A., Arridge, S., & Valentini, G. (2010). Fast 3D optical reconstruction in turbid media using spatially modulated light. Biomedical Optics Express, 1(2), 471. doi:10.1364/BOE.1.000471

Davis, S. C., Dehghani, H., Wang, J., Jiang, S., Pogue, B. W., & Paulsen, K. D. (2007). Image-guided diffuse optical fluorescence tomography implemented with Laplacian-type regularization. Optics Express, 15(7), 4066–4082.

Davis, S. C., Pogue, B. W., Springett, R., Leussler, C., Mazurkewitz, P., Tuttle, S. B., … Paulsen, K. D. (2008). Magnetic resonance-coupled fluorescence tomography scanner for molecular imaging of tissue. The Review of Scientific Instruments, 79(6). doi:10.1063/1.2919131

Ducros, N., D'Andrea, C., Bassi, A., Valentini, G., & Arridge, S. (2012). A virtual source pattern method for fluorescence tomography with structured light. Physics in Medicine and Biology, 57(12), 3811. doi:10.1088/0031-9155/57/12/3811

Ducros, N., D'andrea, C., Valentini, G., Rudge, T., Arridge, S., & Bassi, A. (2010). Full-wavelet approach for fluorescence diffuse optical tomography with structured illumination. Optics Letters, 35(21), 3676. doi:10.1364/OL.35.003676

Fang, Q., & Boas, D. A. (2009). Monte Carlo simulation of photon migration in 3D turbid media accelerated by graphics processing units. Optics Express, 17(22), 20178–20190. doi:10.1364/OE.17.020178

Gibson, A. P., Hebden, J. C., & Arridge, S. R. (2005). Recent advances in diffuse optical imaging. Physics in Medicine and Biology, 50(4), R1–R43.

Gruber, J. D., Paliwal, A., Krishnaswamy, V., Ghadyani, H., Jermyn, M., O'Hara, J. A., … Pogue, B. W. (2010). System development for high frequency ultrasound-guided fluorescence quantification of skin layers. Journal of Biomedical Optics, 15(2), 026028–5.

Hoffman, R. (2002). Green fluorescent protein imaging of tumour growth, metastasis, and angiogenesis in mouse models. The Lancet Oncology, 3(9), 546–556.

Holboke, M. J., Tromberg, B. J., Li, X., Shah, N., Fishkin, J., Kidney, D., … Yodh, A. G. (2000). Three-dimensional diffuse optical mammography with ultrasound localization in a human subject. Journal of Biomedical Optics, 5(2), 237–247.

Jaffer, F. A., Kim, D.-E., Quinti, L., Tung, C.-H., Aikawa, E., Pande, A. N., … Weissleder, R. (2007). Optical Visualization of Cathepsin K Activity in Atherosclerosis With a Novel, Protease-Activatable Fluorescence Sensor. Circulation, 115(17), 2292–2298. doi:10.1161/CIRCULATIONAHA.106.660340

Jaffer, F. A., Libby, P., & Weissleder, R. (2009). Optical and Multimodality Molecular Imaging. Insights Into Atherosclerosis. Arterioscler Thromb Vasc Biol, ATVBAHA.108.165530. doi:10.1161/ATVBAHA.108.165530

Kepshire, D., Mincu, N., Hutchins, M., Gruber, J., Dehghani, H., Hypnarowski, J., … Pogue, B. W. (2009). A microcomputed tomography guided fluorescence tomography system for small animal molecular imaging. The Review of Scientific Instruments, 80(4), 043701. doi:10.1063/1.3109903

Lam, S., Lesage, F., & Intes, X. (2005). Time Domain Fluorescent Diffuse Optical Tomography: analytical expressions. Optics Express, 13(7), 2263–2275.

Li, B., Abran, M., Matteau-Pelletier, C., Rouleau, L., Lam, T., Sharma, R., … Lesage, F. (2011). Low-cost three-dimensional imaging system combining fluorescence and ultrasound. Journal of Biomedical Optics, 16(12), 126010–126010–10. doi:doi:10.1117/1.3662455

Li, B., & Lesage, F. (2012). Ultrasound guided fluorescence tomography, 841208–841208. doi:10.1117/12.2001441

Lin, Y., Barber, W. C., Iwanczyk, J. S., Roeck, W., Nalcioglu, O., & Gulsen, G. (2010). Quantitative fluorescence tomography using a combined tri-modality FT/DOT/XCT system. Optics Express, 18(8), 7835–7850. doi:10.1364/OE.18.007835

Lin, Y., Gao, H., Nalcioglu, O., & Gulsen, G. (2007). Fluorescence diffuse optical tomography with functional and anatomical a priori information: feasibility study. Physics in Medicine and Biology, 52(18), 5569–5585. doi:10.1088/0031-9155/52/18/007

Lin, Y., Ghijsen, M. T., Gao, H., Liu, N., Nalcioglu, O., & Gulsen, G. (2011). A photo-multiplier tube-based hybrid MRI and frequency domain fluorescence tomography system for small animal imaging. Physics in Medicine and Biology, 56(15), 4731–4747. doi:10.1088/0031-9155/56/15/007

Markel, V. A., Mital, V., & Schotland, J. C. (2003). Inverse problem in optical diffusion tomography. III. Inversion formulas and singular-value decomposition. Journal of the Optical Society of America A, 20(5), 890–902. doi:10.1364/JOSAA.20.000890

Nahrendorf, M., Keliher, E., Marinelli, B., Waterman, P., Feruglio, P. F., Fexon, L., … Weissleder, R. (2010). Hybrid PET-optical imaging using targeted probes. Proceedings of the National Academy of Sciences, 107(17), 7910–7915. doi:10.1073/pnas.0915163107

Nahrendorf, M., Waterman, P., Thurber, G., Groves, K., Rajopadhye, M., Panizzi, P., … Weissleder, R. (2009). Hybrid In Vivo FMT-CT Imaging of Protease Activity in Atherosclerosis With Customized Nanosensors. Arterioscler Thromb Vasc Biol, ATVBAHA.109.193086. doi:10.1161/ATVBAHA.109.193086

Ntziachristos, V., & Weissleder, R. (2001). Experimental three-dimensional fluorescence reconstruction of diffuse media by use of a normalized Born approximation. Optics Letters, 26(12), 893–895. doi:10.1364/OL.26.000893

Pyka, T., Schulz, R., Ale, A., & Ntziachristos, V. (2011). Revisiting the normalized Born approximation: effects of scattering. Optics Letters, 36(22), 4329–4331. doi:10.1364/OL.36.004329

Schulz, R. B., Ale, A., Sarantopoulos, A., Freyer, M., Söhngen, R., Zientkowska, M., & Ntziachristos, V. (2009). Hybrid fluorescence tomography/x-ray tomography improves reconstruction quality, 73700H–73700H. doi:10.1117/12.831714

Snyder, C., Kaushal, S., Kono, Y., Tran Cao, H., Hoffman, R., & Bouvet, M. (2009). Complementarity of ultrasound and fluorescence imaging in an orthotopic mouse model of pancreatic cancer. BMC Cancer, 9(1), 106. doi:10.1186/1471-2407-9-106

Soubret, A., Ripoll, J., & Ntziachristos, V. (2005). Accuracy of fluorescent tomography in the presence of heterogeneities: Study of thenormalized born ratio. IEEE Transactions on Medical Imaging, 24(10), 1377–1386.

Srinivasan, S., Pogue, B. W., Dehghani, H., Jiang, S., Song, X., & Paulsen, K. D. (2004). Improved quantification of small objects in near-infrared diffuse optical tomography. Journal of Biomedical Optics, 9(6), 1161–1171. doi:10.1117/1.1803545

Takeda, M., & Mutoh, K. (1983). Fourier transform profilometry for the automatic measurement of 3-D object shapes. Applied Optics, 22(24), 3977–3982. doi:10.1364/AO.22.003977

Tawakol, A., Castano, A. P., Gad, F., Zahra, T., Bashian, G., Migrino, R. Q., … Hamblin, M. R. (2008). Intravascular detection of inflamed atherosclerotic plaques using a fluorescent photosensitizer targeted to the scavenger receptor. Photochemical & Photobiological Sciences, 7(1), 33–39.

Venugopal, V., Chen, J., Lesage, F., & Intes, X. (2010). Full-field time-resolved fluorescence tomography of small animals. Optics Letters, 35(19), 3189–3191. doi:10.1364/OL.35.003189

Vinegoni, C., Razansky, D., Figueiredo, J.-L., Fexon, L., Pivovarov, M., Nahrendorf, M., … Weissleder, R. (2009). Born normalization for fluorescence optical projection tomography for whole heart imaging. Journal of Visualized Experiments: JoVE, (28). doi:10.3791/1389

Waldeck, J., Hager, F., Holtke, C., Lanckohr, C., von Wallbrunn, A., Torsello, G., … Bremer, C. (2008). Fluorescence Reflectance Imaging of Macrophage-Rich Atherosclerotic Plaques Using an v 3 Integrin-Targeted Fluorochrome. Journal of Nuclear Medicine, 49(11), 1845–1851. doi:10.2967/jnumed.108.052514

Wallis de Vries, B. M., Hillebrands, J.-L., van Dam, G. M., Tio, R. A., de Jong, J. S., Slart, R. H. J. A., & Zeebregts, C. J. (2009). Multispectral Near-Infrared Fluorescence Molecular Imaging of Matrix Metalloproteinases in a Human Carotid Plaque Using a Matrix-Degrading Metalloproteinase-Sensitive Activatable Fluorescent Probe. Circulation, 119(20), e534–536. doi:10.1161/CIRCULATIONAHA.108.821389

Wang, L. V., & Wu, H. (2007). Biomedical Optics: Principles and Imaging (1st ed.). Wiley-Interscience.

Weissleder, R., Tung, C.-H., Mahmood, U., & Bogdanov, A. (1999). In vivo imaging of tumors with protease-activated near-infrared fluorescent probes. Nat Biotech, 17(4), 375–378. doi:10.1038/7933

Yalavarthy, P. K., Pogue, B. W., Dehghani, H., Carpenter, C. M., Jiang, S., & Paulsen, K. D. (2007). Structural information within regularization matrices improves near infrared diffuse optical tomography. Optics Express, 15(13), 8043–8058. doi:10.1364/OE.15.008043

Yalavarthy, P. K., Pogue, B. W., Dehghani, H., & Paulsen, K. D. (2007). Weight-matrix structured regularization provides optimal generalized least-squares estimate in diffuse optical tomography. Medical Physics, 34(6), 2085. doi:10.1118/1.2733803

Zhu, Q., Durduran, T., Ntziachristos, V., Holboke, M., & Yodh, A. G. (1999). Imager that combines near-infrared diffusive light and ultrasound. Optics Letters, 24(15), 1050–1052. doi:10.1364/OL.24.001050

Zhu, Q., Huang, M., Chen, N., Zarfos, K., Jagjivan, B., Kane, M., … Kurtzman, H. S. (2003). Ultrasound-Guided Optical Tomographic Imaging of Malignant and Benign Breast Lesions: Initial Clinical Results of 19 Cases. Neoplasia (New York, N.Y.), 5(5), 379–388.

CHAPTER 5 ARTICLE #3: HYBRID FMT-MRI APPLIED TO IN VIVO ATHEROSCLEROSIS IMAGING

Baoqiang Li,[1,2] Foued Maafi,[2] Romain Berti,[2] Philippe Pouliot,[1,2]

Eric Rhéaume,[2] Jean-Claude Tardif,[2] and Frederic Lesage[1,2]

[1]Institute of Biomedical Engineering, École Polytechnique de Montréal, Montreal, QC, H3C 3A7, Canada. [2]Montreal Heart Institute, Montreal, QC, H1T 1C8, Canada

5.1 Presentation of the article

This article (B. Li, et al., 2014) aimed to address the third objective of this thesis. In this work, we developed a dual-modality FMT-MRI system explore anatomy with high spatial resolution as well as molecular fluorescent information of mice. Evaluated first by phantom, and next a mouse corpse, it was demonstrated that the MR-anatomy could optimize the forward modeling and then improve the fluorescence reconstruction. Eventually, this system was applied to in vivo atherosclerosis imaging. This article was published in *Biomedical Optics Express*.

5.2 Abstract

Combining FMT with anatomical imaging, e.g. MRI facilitates interpreting functional information. Furthermore, using a heterogeneous model for light propagation has been shown in simulations to be superior to homogeneous modeling to quantify fluorescence. Here, we present a combined FMT-MRI system and apply it to heart and aorta molecular imaging, a challenging area due to strong tissue heterogeneity and the presence of air-voids due to lungs. First investigating performance in a phantom and mouse corpse, the MRI-enabled heterogeneous models resulted in an improved quantification of fluorescence reconstructions. The system was then used in mice for in vivo atherosclerosis molecular imaging. Results show that, when using

the heterogeneous model, reconstructions were in agreement with the ex vivo measurements. Therefore, the proposed system might serve as a powerful imaging tool for atherosclerosis in mice.

5.3 Introduction

One of the advantages of combining FMT with anatomical imaging is anatomical guidance for an improved quantification of reconstructions (Ale et al., 2010; Davis et al., 2007a; Flynn et al., 2013; B. Li et al., 2011; Yuting Lin et al., 2010b; Radrich et al., 2012). While previous reports show that BN could cancel off some experimental factors, such as laser coupling loss, camera gain and exposing time, as well as reduce the effect of absorption heterogeneity in fluorescence reconstructions (Ntziachristos & Weissleder, 2001); but limitations to suppress scattering variations were found (Pyka et al., 2011). Furthermore, it was demonstrated in simulations that homogeneous forward models might induce significant quantification errors in the reconstruction, which could be improved by propagating light in a heterogeneous model (Juan Felipe Perez-Juste Abascal et al., 2012). In this context, especially working with CW mode, in which absorption and scattering cannot be separated (Gibson et al., 2005), anatomical imaging is an essential addition in order to optimize forward modeling and achieve an accurate reconstruction.

Hybrid modality imaging combining FMT with MRI, X-ray CT, or ultrasound has been increasingly used in human breast, prostate and preclinical cancer models (Ale et al., 2012a, 2013; Boutet et al., 2009; Laidevant et al., 2011). However, cardiovascular imaging in small animals has mostly been limited to ex vivo or in vitro imaging (Sosnovik et al., 2007) due to the high absorption of light by the heart (Tardif et al., 2011), the presence of air gaps due to lungs and the heterogeneous nature of light absorption properties of tissue in this region. Furthermore, the aorta, which is often a target in atherosclerosis imaging (Jaffer et al., 2009a), has a relatively

small size leading to challenges both for optical detection and structural delineation. Nevertheless noninvasive in vivo imaging plays an important role in preclinical atherosclerosis studies (Jaffer et al., 2009a). Therefore, combining the high sensitivity of FMT with the high spatial resolution of MRI, a hybrid FMT-MRI system is expected to improve in vivo atherosclerosis imaging in small animals.

The objectives of this study were threefold: (1) To develop a novel hybrid modality FMT-MRI system to explore both functional information and anatomy simultaneously; (2) to evaluate the benefits of using a heterogeneous model of tissues for light propagation (Juan Felipe Perez-Juste Abascal et al., 2012); and (3) to provide a proof of concept for in vivo atherosclerosis imaging of mice. To achieve these objectives, we developed a fiber-based optical probe to acquire conduct FMT in parallel with MRI. By addressing source fibers sequentially with a Galvo mirror and detecting using a single snapshot of all the detection fibers with a sensitive EMCCD camera, our system enabled faster optical sampling than the existing FMT-MRI systems (Carpenter et al., 2010; Davis et al., 2008; Y Lin et al., 2011a). The system was next characterized with a phantom and then with a mouse corpse containing a known fluorescent inclusion, thereby demonstrating quantification improvements when using heterogeneous modeling. Finally, the system was used to image MMP activity, an important target for atherosclerosis imaging (Jaffer et al., 2009a; Sanz & Fayad, 2008) in atherosclerotic (ATX) and control (Ctrl) mice (Sanan et al., 1998).

5.4 System

5.4.1 FMT system design

As shown in Figure 5.1, a collimated laser beam at 660 nm (HL6545MG, Thorlabs) was first cleaned up by a band-pass filter (FF01-661/11, Semrock), and then re-directed by a galvo mirror

(GVS012, Thorlabs), to be focused by two lenses (LA1257-B, Thorlabs) towards an optical fiber matrix (FT200UMT, Thorlabs). A total of 36 fibers were used for excitation, positioned in a matrix covering a 15 mm × 15 mm area. Similarly, 36 fibers were employed for detection. The detection fibers were mounted on a metal plate, and filmed by a sensitive EMCCD camera (Nüvü Cameras).

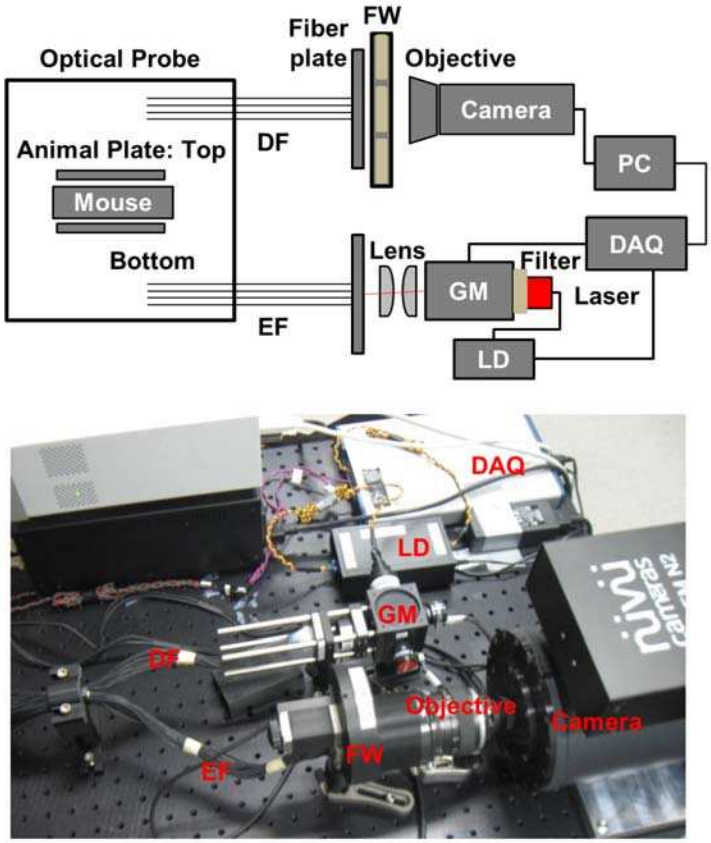

Figure 5.1: Schematic (top) and photograph (bottom) of the FMT system. GM: Galvo mirror; EF: excitation fibers; DF: detection fibers; LD: laser driver; FW: Filter wheel.

The received light corresponding to different detection fibers was thus collected by distinct pixels of the EMCCD chip. The camera exposition time was set to 100 milliseconds for all imaging presented in this work. Detection wavelength was selected by optical filters mounted on a motorized filter wheel (FW103, Thorlabs). In this study, the emitted fluorescence was

selected by a band-pass filter, FF01-716/40 (Semrock) optimized for Cy5.5. To reach the MRI bore, each fiber was 6 m long, and connected to a home-made MRI-compatible optical probe. Light coupling loss was measured to be around 40% on average. Components were synchronized by a data acquisition (DAQ) card (NI USB-6353, NI).

5.4.2 Optical probe design

The optical probe consisted of two MRI compatible plastic plates (animal plates). The top one is illustrated by the schematic diagram in Figure 5.2. This plate was mounted with 18 excitation fibers and 18 detection fibers interlaced with a distance of 3 mm and covering a total area of 15 mm × 15 mm. Likewise, the same geometry was employed for the bottom (not shown). As seen in the photograph, the animal was installed between the two plates with the ROI covered by the fibers. The distance between the two plates could be adjusted to allow the fibers to be brought into close contact with the sample. Each fiber was protected by a black rubber shrink-tube to prevent contamination from ambient light and to reduce crosstalk between fibers. Five holes, serving as fiducial markers, were made on the plate (Figure 5.2). By filling with water prior to MR imaging, the holes could be visualized in MR images and used as reference to localize fibers for the simulation of photon propagation for each source. The photograph in Figure 5.2 shows how the optical probe was installed on the MRI animal holder. With this planar setup, both transmission and reflection measurements were obtained from two sides of the animal. But only transmission data was used for reconstruction. A 7-Tesla MRI system with 30 cm bore (Agilent) was used in this study. As previously mentioned, MRI and fluorescence imaging were done simultaneously.

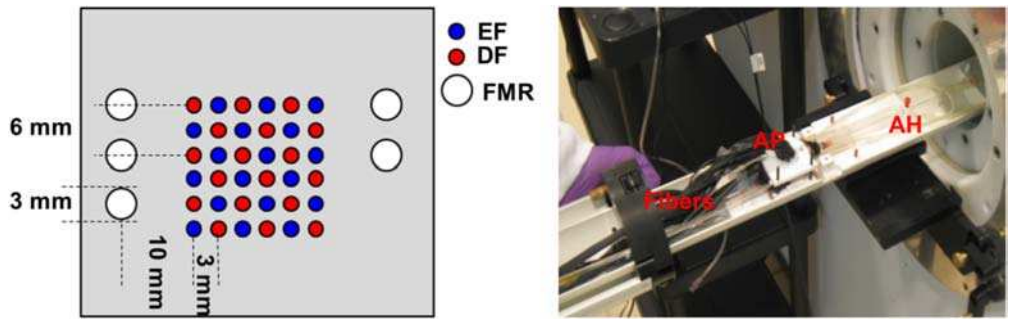

Figure 5.2: Schematic diagram (left, top side) and photograph (right) of the optical probe working in an experiment. AH: animal holder; AP: animal plate; FMR: fiducial marker.

5.5 Reconstruction

5.5.1 MR anatomy guided forward modeling

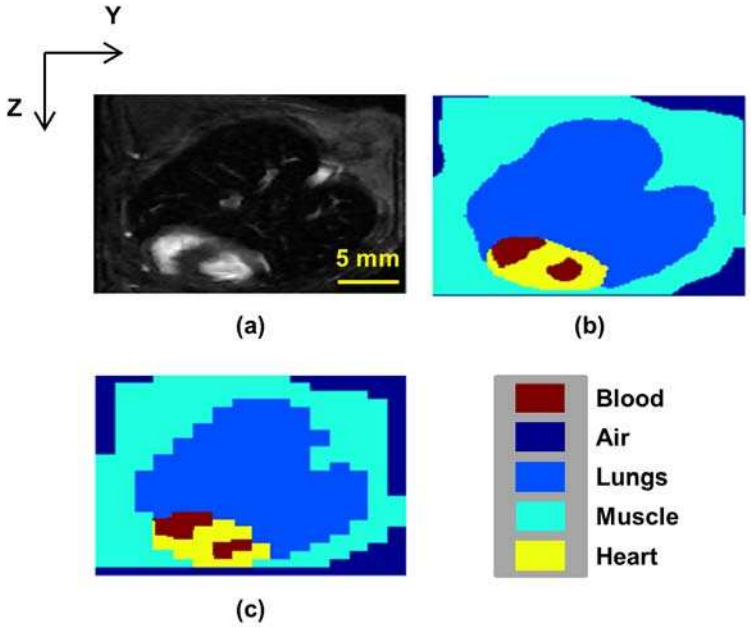

Figure 5.3: (a) Representative axial MR slice of ATX #2; (b) segmented image; (c) resampled segmented image with 1 mm voxel resolution.

Photons propagation was simulated using Monte-Carlo simulations on GPU (Fang & Boas, 2009). To define tissue boundaries for heterogeneous photon propagation, a fast segmentation algorithm was used (J. Yuan, Bae, & Tai, 2010) supplemented by manual correction. The

segmentation process is shown in a representative slice of one mouse (ATX #2 below). As shown by the MR slice in Figure 5.3 (a), blood was bright with this sequence so that the heart and aorta could easily be segmented. The rest of the body was automatically separated into air, lungs, blood and muscle. The boundaries between different sections were manually corrected for all the slices. Lung walls could not be separated, and were regarded as muscle for photon propagation. Lung cavities were set to air in forward modeling. The segmented image by this semi-automatic method is shown in Figure 5.3 (b). The image was resampled to 1 mm voxel resolution for forward modeling (Figure 5.3 (c)). Literature optical properties were assigned according to the segmentation (Alexandrakis et al., 2005; S. A. Prahl, n.d.).

This semi-automatic segmentation was also used in the experiment with the mouse corpse (images not shown). In that experiment, fat tissue was brighter in the MR images; and the fluorescent inclusions were approximately inserted into the liver area of the mouse corpse, where the heart and lungs were not included in the FOV of FMT. Because the biological composition was different from a living mouse and the organs were delocalized due to inserting fluorescence inclusions, the corpse was simply segmented to muscle and fat.

5.5.2 MR-prior constrained reconstruction

Image reconstruction was done by minimizing the following objective function:

$$\Omega = \left\| \Phi^{meas} - W\chi \right\|^2 + \lambda \left\| L\chi \right\|^2, \tag{5.1}$$

where $\lambda \left\| L\chi \right\|^2$ is a penalty term to regularize the reconstruction process and reduce its ill-posedness. Then, the first-order condition, $\frac{\partial \Omega}{\partial \chi} = 0,$ leads to the following iterative minimization process, as detailed in Ref. (Yalavarthy, Pogue, Dehghani, & Paulsen, 2007):

$$\chi_{i+1} = [W^T W + \lambda L^T L]^{-1} W^T (\Phi_i^{meas} - \Phi_i^C) + \chi_i, \tag{5.2}$$

where

$$W = \frac{\int_V G^x(r_s, r) G^m(r, r_d) d^3 r}{G^x(r_s, r_d)}. \tag{5.3}$$

Here, Φ^{meas} and Φ^C are the experimental and simulated Born ratios (Ntziachristos & Weissleder, 2001); W is the sensitivity matrix; χ represents the fluorescence yield εηC, in which ε, η and C are the extinction coefficient, quantum yield and concentration of the fluorophore. The matrix L encodes the prior localization of fluorescence emission in Laplacian form; it is used to constrain reconstruction as a soft-prior (Yalavarthy, Pogue, Dehghani, & Paulsen, 2007). λ is the regularization parameter to adjust the strength of the penalty term; $G^x(r_s, r)$ and $G^m(r, r_d)$ are two Green functions, which describe the photon propagations from source (r_s) to an arbitrary position in tissue (r), and from tissue to detector (r_d), respectively. Finally, reconstruction was performed iteratively, and i represents the iteration index. Convergence was said to be achieved when the projection error between two iterations was below 1%. However, a maximum of eight iterations was imposed to avoid the estimated error increasing (Yalavarthy, Pogue, Dehghani, & Paulsen, 2007).

To diminish the error in reconstruction induced by an imprecise segmentation and/or an inadequate knowledge on the localization of fluorescence emission, the matrix L encoding spatial priors was used only in the first iteration but replaced by an identity matrix in the following iterations. The initial value of fluorescent yield was set to be zero. It has been reported that an optimal λ was often determined empirically (Yalavarthy, Pogue, Dehghani, & Paulsen, 2007). But to avoid bias on this part, the initial value of λ was determined by an L-curve method (Hansen & O'Leary, 1993). As a result, the value of λ was less than 2 for all the reconstructions presented in this study.

5.6 Experiments

5.6.1 Phantom experiment

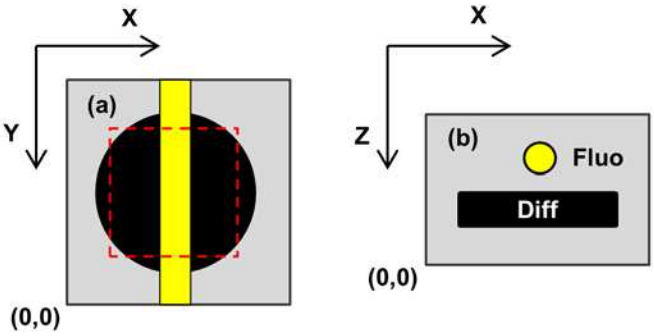

Figure 5.4: Schematic diagram of the phantom: (a) view of X-Y plane; (b) view of X-Z plane. The attenuation and fluorescence inclusions are denoted by Diff and Fluo, respectively.

Table 5.1: Dimension and optical properties of the phantom.

	Center position (mm)			**Dimension (mm)**				**Optical properties (mm^{-1})**	
	X	**Y**	**Z**	**Diameter**	**X**	**Y**	**Z**	μ_α	μ_s'
Bulk	--	--	--	--	30	30	20	0.02	1.0
Diff	13	15	7	18	--	--	6	0.005	0.5
Fluo	14	--	13	4	--	30	**--**	**--**	**--**

Phantom experiments were first conducted to characterize the FMT system and the associated reconstruction algorithm. The dimension of the phantom is illustrated in Figure 5.4 with detailed information provided in Table 5.1. The phantom was installed between the two plates with the fibers covering an area approximately illustrated by the dashed red square in Figure 5.4 (a). Cylindrical transparent tubes (length: 30mm, inner ⌀: 3mm) filled with Cy5.5 solution at concentrations of 200nM, 100nM and 50nM were inserted into 'Fluo' in Figure 5.4 (b), and then imaged. For confirmation and to account for potential dilution errors, each

fluorescent tube was imaged ex vivo using a commercial epi-illumination fluorescence imaging system (IVIS Lumina, PerkinElmer).

5.6.2 Mouse corpse experiment

To mimic the in vivo environment, a mouse corpse was employed to evaluate the FMT-MRI system. Transparent tubes, of each having a volume of ~106μL, filled with Cy5.5 solution at 600nM and 400nM were each inserted into approximately the same region in the body and then imaged by the FMT-MRI system. For MRI imaging, a T1-weighted 3D sequence was used so that fatty tissue was bright. Parameters were TR/TE = 5.0, 2.5 ms, FA = 30, matrix size of 256 × 192 × 256, 4 averages, 16 minutes scan time. Spatial resolution along the X, Y and Z direction was 0.18 mm, 0.16 mm and 0.16 mm (Figure 5.7). The whole FMT-MRI process took ~20 minutes for each concentration.

5.6.3 In vivo experiment

The FMT-MRI system was then used to evaluate in vivo molecular imaging of atherosclerosis. All animal manipulations were approved by the ethics committee of Montreal Heart Institute. Two ATX ($LDLR^{-/-}$; Human Tg ($apoB^{+/+}$); ~19 months old) and two Ctrl (C57/B6; ~3 months old) mice were imaged, labeled ATX #1, #2 and Ctrl #1, #2 in the following. The ATX mice have a gene deletion in the LDL receptor (Ldlr) gene and overexpress the human apolipoprotein B. Mice lacking the LDL receptor will develop atherosclerosis spontaneously without the need of high fat diet during 16 weeks (Sanan et al., 1998).

Using those mice at advanced age (19 months) allow them to develop a severe atherosclerotic plaque on a chow diet, in which the metalloproteinase's (MMP's) activity would be higher compared to the wild type mice (C57/B6). To visualize MMPs activity induced by

atherosclerosis, ~16 nmol of a molecular probe (MMPSense 680, PerkinElmer) was intravenously administered, with the dose being proportional to the individual weight. For each mouse, imaging was conducted before and 24 hours after the administration of the probe. For FMT, the FOV of the optical probe was designed to approximately cover the heart area. For MRI, a 2D CINE bright blood sequence (in rapid single phase mode) was used with cardiac but no respiratory gating. The parameters were as follows: TR in the range 120-140 ms (one R-R interval), TE = 1.8 ms, FA = 30, 256 x 256 matrix leading to 0.18 x 0.14 mm resolution (see Figure 5.8), 30 slices of 1 mm thickness, 20 averages. For each mouse, the FMT-MRI process was completed in ~45 minutes. After the experiment, the mice were sacrificed and dissected; hearts and aortas were imaged ex vivo for evaluation.

5.7 Results

5.7.1 Phantom experiment

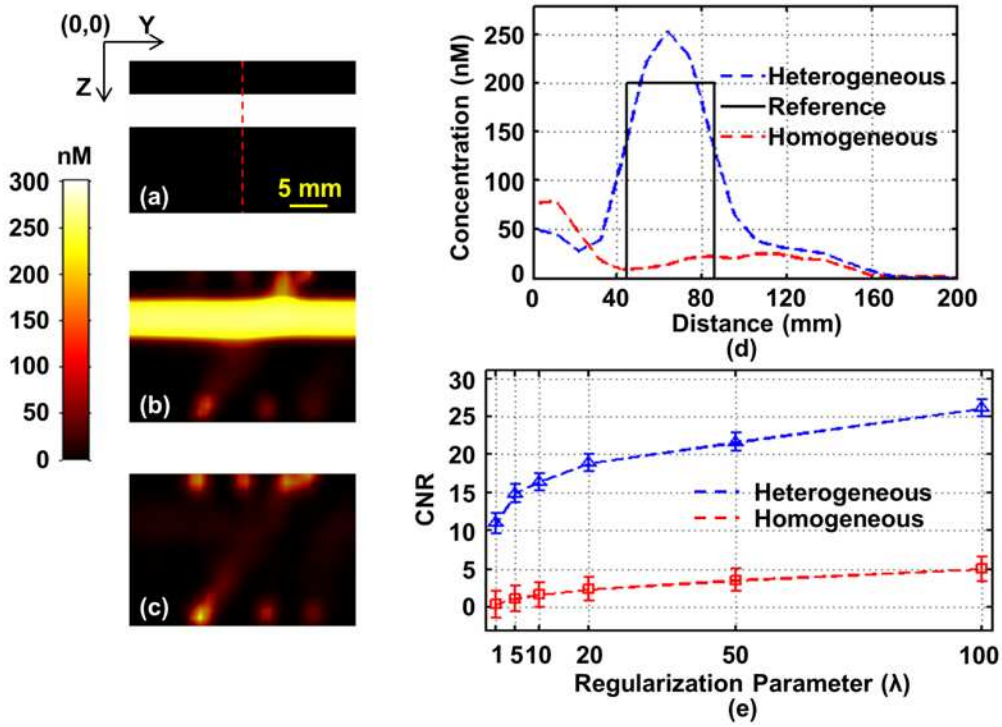

Figure 5.5: (a) A synthetic fluorescence slice of the phantom; (b) the corresponding slices of the reconstruction with the heterogeneous models (b), and with the homogeneous model (c), respectively; (d) plot of reconstructed values along the red dashed line. (e) CNR was compared with λ for both models.

Phantom experiments were used to evaluate the impact of heterogeneous modeling on the quantification of fluorescence reconstructions. A heterogeneous model was built as illustrated in Figure 5.4, with optical properties assigned according to Table 5.1. The homogeneous model used bulk optical properties to propagate light. In both models, the fluorescent inclusion, denoted by 'Fluo' in Figure 5.4 (b), was assigned with the bulk optical properties. Identical optical properties were assumed at the excitation and the emission wavelengths consistent with small absorption changes expected with this phantom. Finally, the localization of the tubes was used as

a soft-prior to constrain the reconstructions of the fluorescence yield $\varepsilon\eta C$. Taking the published values of ε and η (Talanov et al., 2006), concentration C of the embedded Cy5.5 fluorophore was then estimated. As shown in Figure 5.5, a representative reconstruction of the fluorescent tube filled with 200nM Cy5.5 solution. One slice of the phantom is illustrated in Figure 5.5 (a), with the fluorescent tube indicated by the white bar. The reconstructed concentration of the corresponding slice with the heterogeneous and homogeneous models is presented in Figure 5.5 (b) and (c). As shown, heterogeneous modeling resulted in better localization and quantification. The reconstructed concentration values along the red dashed line in Figure 5.5 (a) were plotted for analysis (Figure 5.5 (d)). Overall, the reconstructed concentrations of the fluorescent inclusions with the heterogeneous models for 200nM, 100nM and 50nM were estimated at ~260nM, ~151nM and ~83nM, respectively. Contrast to Noise Ratio was also evaluated as defined by $CNR = (S_A - S_B)/\sigma$, where S_A/S_B is the average value of the fluorescent inclusion/background respectively, σ is the standard deviation of background. With heterogeneous reconstructions, the CNRs were 11.6, 11.7 and 10.7 for the cases of 200nM, 100nM and 50nM, respectively. With the homogeneous models, the CNRs were ~29 times lower on average. Shown in Figure 5.5 (e), different λ from 1 to 100 were used in the reconstructions. The homogeneous reconstructions were significantly improved with greater λ. And a better CNR could be consistently achieved with heterogeneous model for each λ.

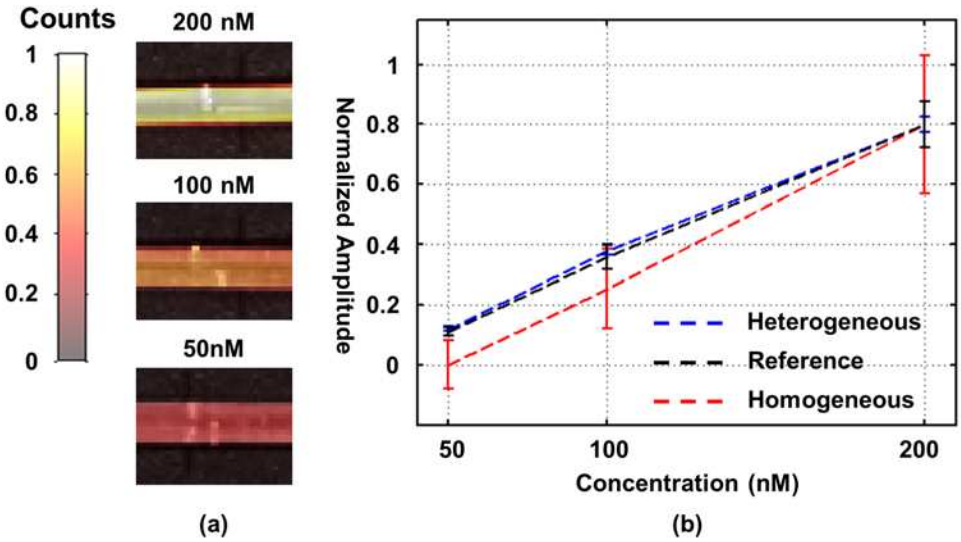

Figure 5.6: (a) Ex vivo images of the fluorescent tubes were overlaid with transparency (alpha=0.5) on the photographs of tubes, respectively; (b) the average reconstructed values (both models) of the fluorescent tubes were normalized of the maximum being 1, to compare with the ex vivo measurement (reference).

In Figure 5.6 (a), the fluorescent tubes were measured ex vivo as reference; and the fluorescence images were overlaid with transparency (alpha=0.5) on the photographs of the tubes. Then, the average reconstructed values in the fluorescent inclusions for different cases of concentrations were normalized to the maximum. As shown in Figure 5.6 (b), linearity was achieved for the reconstructions with both heterogeneous and homogeneous models. Nonetheless, the heterogeneous model reconstructions show a higher fidelity to the reference. When quantified, the standard deviation of the difference between the reconstruction with the heterogeneous model and the reference is ~0.01; but, drops to ~0.06 for the homogeneous counterpart.

5.7.2 Mouse corpse experiment

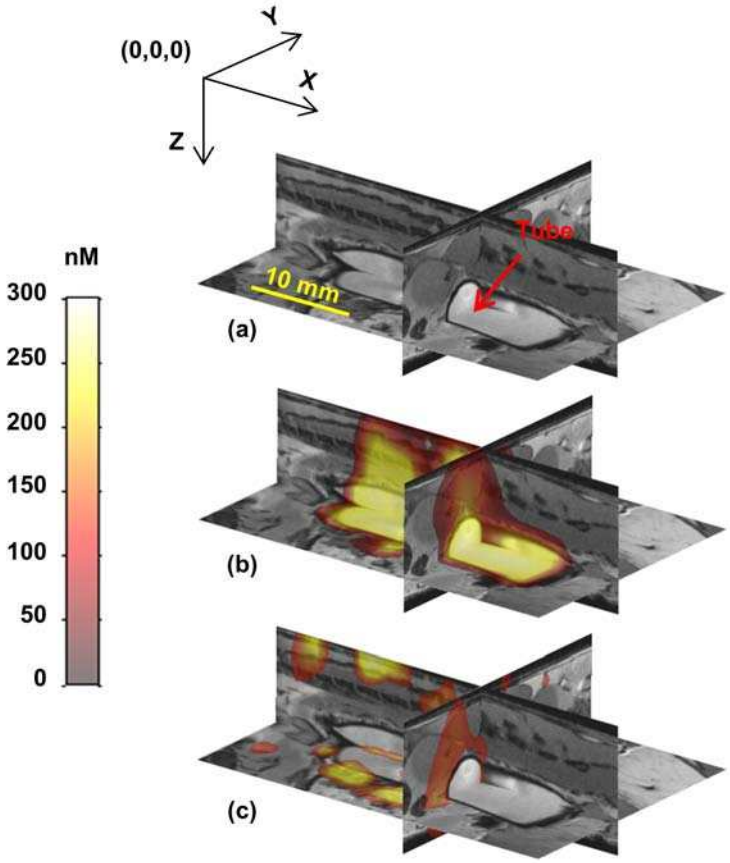

Figure 5.7: (a) Three orthogonal MR slices are shown: axial slice (Y-Z), coronal slice (X-Y) and sagittal slice (X-Z). The arrow of the X axes points to tail of the mouse; and the arrow of the Z axes points to abdomen. The tube was indicated by the red arrow; (b) the reconstructions with the heterogeneous models were overlaid with transparency (alpha=0.5) on the MR slices, respectively; (c) the reconstructions with the homogeneous models were overlaid with transparency (alpha=0.5) on the MR slices, respectively.

Results obtained with the fluorescent tube filled with 400nM Cy5.5 solution are presented as an example. Three orthogonal MR slices are shown in Figure 5.7 (a). For visualization, the reconstructed images were overlaid with transparency (alpha=0.5) on the MR slices and a threshold was set to reduce background intensities. With this experiment, the reconstructed

concentrations with the heterogeneous model for the cases of 600nM and 400nM were ~640nM and ~237nM with CNRs of ~7.7 and ~2.7, respectively. Again, the CNR of the reconstructions with the heterogeneous models were ~6.6 times better than their homogeneous counterpart. Linearity was compared for the reconstructions with both types of models and the standard deviation of the difference between the heterogeneous reconstructions and the reference was ~0.22, but dropped to ~0.89 for the homogeneous counterpart.

Both CNR and linearity of the reconstructions decreased when compared to the phantom experiment likely due to greater absorption and scattering of tissue, which deteriorated SNR of the corresponding measurements. The value of regularization parameter, determined by the L-curve method, was estimated lower in this case which may reduce reconstruction contrast (Yalavarthy, Pogue, Dehghani, & Paulsen, 2007). Finally, although taking into account the heterogeneity of the mouse corpse, the forward modeling remained a considerable approximation due to the rough segmentation.

5.7.3 In vivo experiment

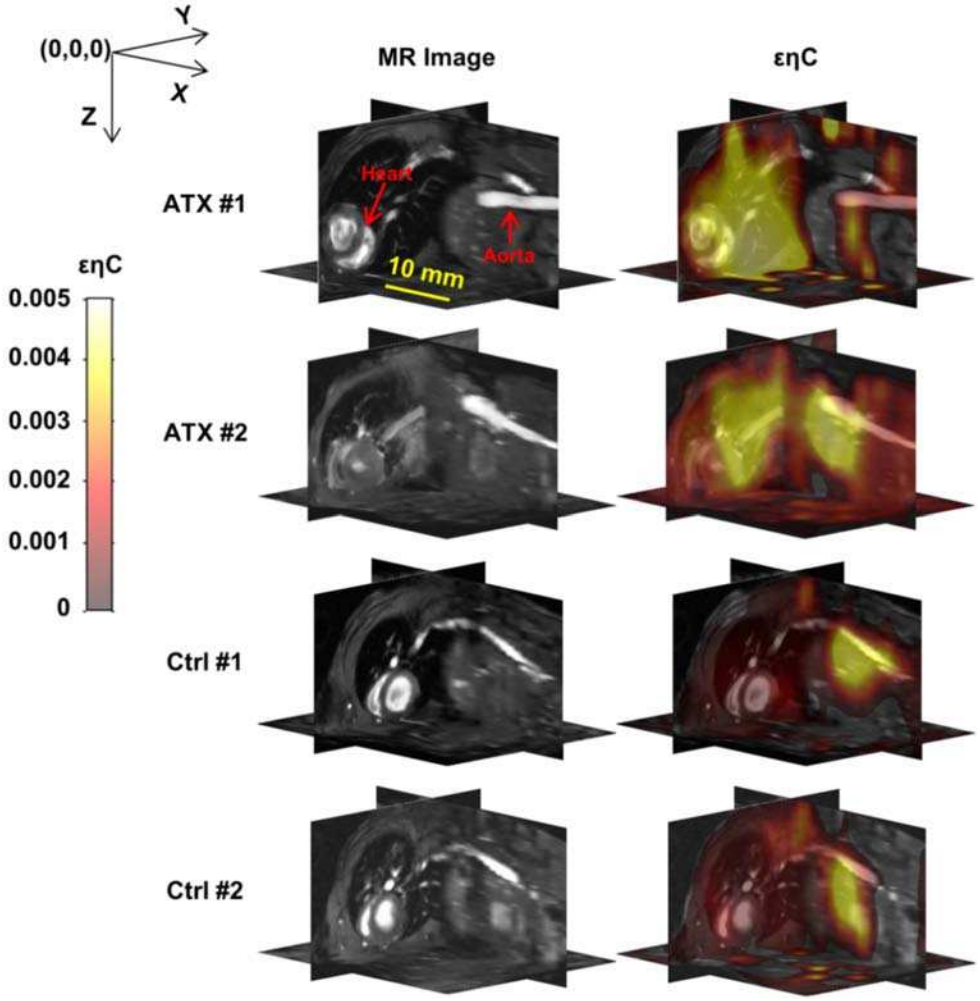

Figure 5.8: The images in the first column are the MR slices for each mouse. Heart and part of aorta of ATX #1 were denoted by red arrows. In the second column, the reconstructed εηC with the heterogeneous models were overlaid with transparency (alpha=0.5) on the MR slices, respectively. Three orthogonal MR slices were chosen for each mouse: axial slice (Y-Z), coronal slice (X-Y) and sagittal slice (X-Z).

Finally, the reconstructions of the four mice are shown in Figure 5.8. Because the values of ε and η are unknown for this molecular probe, fluorescence yield εηC instead of concentration is presented. As identified a posteriori by the ex vivo analysis, a considerable amount of

fluorescence signal was observed in the lungs. Therefore, the heart, aorta and lungs were used as soft-prior to constrain the reconstructions. MR image slices used for segmentation are shown in the first column of Figure 5.8. Here, the axial slice is approximately located in the center of the heart while the sagittal slice was chosen to visualize part of the descending aorta. In the second column of Figure 5.8, the reconstructed $\varepsilon\eta C$ with the heterogeneous model is overlaid with transparency (alpha=0.5) on the corresponding MR slices. For visualization, a threshold was set to reduce background intensities. Fluorescence intensity was higher in the ATX mice than the control ones, which might reflect the known increase MMPs activity of the ATX mice. The average value of $\varepsilon\eta C$ on the regions of heart and aorta for ATX #1, ATX #2, Ctrl #1 and Ctrl #2 was ~0.0027, ~0.0024, ~0.0011 and ~0.0011, respectively. As with the dead mouse experiment, reconstructions with the homogeneous models were underestimated (data not shown).

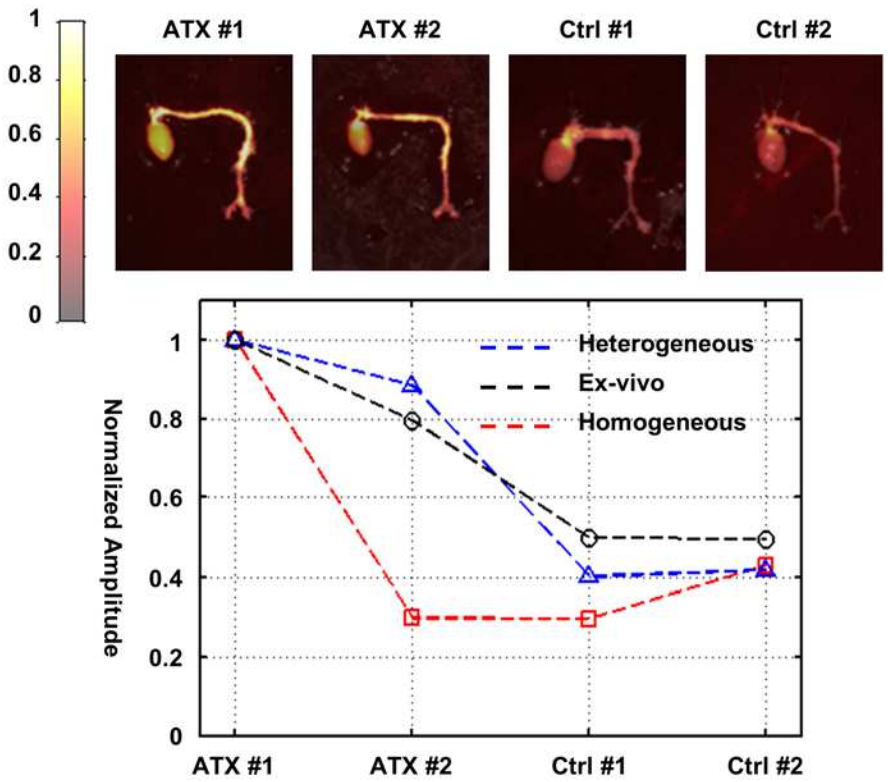

Figure 5.9: The hearts and aortas of the four mice were imaged ex vivo. In the first row, the ex vivo fluorescence images were overlaid with transparency (alpha=0.5) on the corresponding

photographs. Shown by the curves below, the average reconstructed εηC of the hearts and aortas for all mice were normalized with the maximum being 1 to compare with the ex vivo measurement.

Reconstructions were then evaluated by ex vivo measurements (Figure 5.9). In the first row, fluorescence from the heart and aorta is shown for all mice confirming increase uptake in ATX #1 and #2. A comparison of reconstruction estimations with ex vivo measurements is also provided for both homogeneous and heterogeneous forward modeling (normalized to ATX #1). Quantitatively, the standard deviation of the difference between the reconstructions with the heterogeneous models and the ex vivo measurement was ~0.08, but drops to ~0.22 for the homogeneous counterpart.

5.8 Discussion

In this paper, a hybrid-modal FMT-MRI system targeted to mouse cardiovascular imaging was presented. Working with long fibers, emitted photons corresponding to all detection fibers for each source could be recorded in one single snapshot with an EMCCD camera. Hence, a full measurement at one wavelength for all sources (36) was completed within ~30 seconds. An optical probe was designed to quickly install the animal within the MRI holder. Therefore, with fibers on the top and bottom sides of the optical probe, transmission measures were obtained from both sides of the animal; and MRI was conducted simultaneously to FMT.

One of the objectives of this study was to achieve an improved quantification of reconstructions with heterogeneous forward modeling. MR-anatomy enabled the construction of a heterogeneous model for improved simulations of photons propagation, including void regions created by lungs. To evaluate benefits of this approach, reconstructions with both heterogeneous and homogeneous models were compared using experimental measures on phantoms. The results

confirm that heterogeneous modeling is beneficial to reconstructions both in terms of localization and quantification. There results were further confirmed using a more realistic geometry using a mouse corpse.

Finally, the FMT-MRI system was applied in in vivo imaging of atherosclerosis. Following administration of a molecular probe, specific fluorescence signal was detected, which reflects the MMPs activity involved in the progression of atherosclerosis. With the heterogeneous models, the evaluation of fluorescence yield from the hearts and aortas were well correlated to the ex vivo measurements, not as clearly with homogenous modeling.

There remain limitations to this study: besides forward modeling, anatomical prior information could also benefit the inverse problem which was not investigated here. Second, although taking into account the heterogeneity of tissue, rough segmentations of the MR anatomies and the use of literature values for optical properties might induce modeling error. Time-resolved measurements may provide some help (Gao, Zhao, & Yamada, 2002) to reconstruct first the optical properties. Finally, we showed that a soft-prior could help obtain better quantitative reconstructions. Nonetheless, such priors are not always achievable in in vivo experimental situations. In this study, although heart and aorta are the major targets for atherosclerosis imaging, MMPs activated fluorescence was found more broadly from the body of mice. Lungs were found to have considerable fluorescence and thus included in the priors. However, to avoid over-constrain, the soft-priors were only used in the first iteration of reconstruction and replaced with an identity matrix for the following iterations. Alternatively, it might be expected that with an optimized forward model and a more advanced detection mechanism (Frederic Leblond et al., 2011) having better SNR, the reliance of prior on reconstruction could be alleviated.

5.9 Conclusion

In summary, we have developed a hybrid-modal FMT-MRI system to explore both functional and anatomical information in mice. Using MR-derived anatomical information, the benefits of heterogeneous forward modeling was demonstrated in experiments encompassing phantom, mouse corpse and in vivo imaging of atherosclerosis. The reconstructions with the heterogeneous models showed higher fidelity to the ex vivo measurements when compared to the homogeneous model. Therefore, the proposed FMT-MRI system associated with the reconstruction method might serve as a tool for atherosclerosis imaging of small animals. Furthermore, due to its improved acquisition rate, the future application of this system will be in dual-modality pharmacokinetic imaging with preclinical tumorous mice.

5.9 Acknowledgments

This study has been funded by a CIHR Catalyst grant (107765) and a NSERC Discovery grant (239876-2011) to F. Lesage. B. Li is supported by China Scholarship Council.

5.10 References

Abascal, J. F. P.-J., Aguirre, J., Chamorro-Servent, J., Schweiger, M., Arridge, S., Ripoll, J., Desco, M. (2012). Influence of absorption and scattering on the quantification of fluorescence diffuse optical tomography using normalized data. Journal of Biomedical Optics, 17(3), 0360131–0360139. doi:10.1117/1.JBO.17.3.036013

Ale, A., Ermolayev, V., Deliolanis, N. C., & Ntziachristos, V. (2013). Fluorescence background subtraction technique for hybrid fluorescence molecular tomography/x-ray computed tomography imaging of a mouse model of early stage lung cancer. Journal of Biomedical Optics, 18(5), 056006–056006. doi:10.1117/1.JBO.18.5.056006

Ale, A., Ermolayev, V., Herzog, E., Cohrs, C., de Angelis, M. H., & Ntziachristos, V. (2012). FMT-XCT: in vivo animal studies with hybrid fluorescence molecular tomography-X-ray computed tomography. Nature Methods, 9(6), 615–620. doi:10.1038/nmeth.2014

Ale, A., Schulz, R. B., Sarantopoulos, A., & Ntziachristos, V. (2010). Imaging performance of a hybrid x-ray computed tomography-fluorescence molecular tomography system using priors. Medical Physics, 37(5), 1976–1986.

Alexandrakis, G., Rannou, F. R., & Chatziioannou, A. F. (2005). Tomographic bioluminescence imaging by use of a combined optical-PET (OPET) system: a computer simulation feasibility study. Physics in Medicine and Biology, 50(17), 4225–4241. doi:10.1088/0031-9155/50/17/021

Boutet, J., Saroul, L., Duboeuf, F., Herve, L., Debourdeau, M., Vray, D., … Dinten, J.-M. (2009). Bimodal ultrasound and fluorescence approach for prostate cancer diagnosis. Journal of Biomedical Optics, 14(6), 064001–064001–7. doi:10.1117/1.3257236

Carpenter, C. M., Rakow-Penner, R., Jiang, S., Daniel, B. L., Pogue, B. W., Glover, G. H., & Paulsen, K. D. (2010). Inspired gas-induced vascular change in tumors with magnetic-resonance-guided near-infrared imaging: human breast pilot study. Journal of Biomedical Optics, 15(3), 036026. doi:10.1117/1.3430729

Davis, S. C., Dehghani, H., Wang, J., Jiang, S., Pogue, B. W., & Paulsen, K. D. (2007). Image-guided diffuse optical fluorescence tomography implemented with Laplacian-type regularization. Optics Express, 15(7), 4066–4082. doi:10.1364/OE.15.004066

Davis, S. C., Pogue, B. W., Springett, R., Leussler, C., Mazurkewitz, P., Tuttle, S. B., … Paulsen, K. D. (2008). Magnetic resonance-coupled fluorescence tomography scanner for molecular imaging of tissue. The Review of Scientific Instruments, 79(6). doi:10.1063/1.2919131

Fang, Q., & Boas, D. A. (2009). Monte Carlo simulation of photon migration in 3D turbid media accelerated by graphics processing units. Optics Express, 17(22), 20178–20190. doi:10.1364/OE.17.020178

Flynn, B. P., DSouza, A. V., Kanick, S. C., Davis, S. C., & Pogue, B. W. (2013). White light-informed optical properties improve ultrasound-guided fluorescence tomography of photoactive protoporphyrin IX. Journal of Biomedical Optics, 18(4), 046008–046008. doi:10.1117/1.JBO.18.4.046008

Gao, F., Zhao, H., & Yamada, Y. (2002). Improvement of Image Quality in Diffuse Optical Tomography by use of Full Time-Resolved Data. Applied Optics, 41(4), 778–791. doi:10.1364/AO.41.000778

Gibson, A. P., Hebden, J. C., & Arridge, S. R. (2005). Recent advances in diffuse optical imaging. Physics in Medicine and Biology, 50(4), R1–R43.

Hansen, P. C., & O'Leary, D. P. (1993). The Use of the L-Curve in the Regularization of Discrete Ill-Posed Problems. SIAM Journal on Scientific Computing, 14(6), 1487–1503. doi:10.1137/0914086

Jaffer, F. A., Libby, P., & Weissleder, R. (2009). Optical and Multimodality Molecular Imaging. Insights Into Atherosclerosis. Arterioscler Thromb Vasc Biol, ATVBAHA.108.165530. doi:10.1161/ATVBAHA.108.165530

Laidevant, A., Hervé, L., Debourdeau, M., Boutet, J., Grenier, N., & Dinten, J.-M. (2011). Fluorescence time-resolved imaging system embedded in an ultrasound prostate probe. Biomedical Optics Express, 2(1), 194–206. doi:10.1364/BOE.2.000194

Leblond, F., Tichauer, K. M., Holt, R. W., El-Ghussein, F., & Pogue, B. W. (2011). Toward whole-body optical imaging of rats using single-photon counting fluorescence tomography. Optics Letters, 36(19), 3723–3725.

Li, B., Abran, M., Matteau-Pelletier, C., Rouleau, L., Lam, T., Sharma, R., … Lesage, F. (2011). Low-cost three-dimensional imaging system combining fluorescence and ultrasound. Journal of Biomedical Optics, 16(12), 126010–126010–10. doi:doi:10.1117/1.3662455

Lin, Y., Barber, W. C., Iwanczyk, J. S., Roeck, W. W., Nalcioglu, O., & Gulsen, G. (2010). Quantitative fluorescence tomography using a trimodality system: in vivo validation. Journal of Biomedical Optics, 15(4), 040503–040503–3. doi:10.1117/1.3467495

Lin, Y., Ghijsen, M. T., Gao, H., Liu, N., Nalcioglu, O., & Gulsen, G. (2011). A photo-multiplier tube-based hybrid MRI and frequency domain fluorescence tomography system for small animal imaging. Physics in Medicine and Biology, 56(15), 4731–4747. doi:10.1088/0031-9155/56/15/007

Ntziachristos, V., & Weissleder, R. (2001). Experimental three-dimensional fluorescence reconstruction of diffuse media by use of a normalized Born approximation. Optics Letters, 26(12), 893–895. doi:10.1364/OL.26.000893

Prahl, S. A. (n.d.). Online resource: http://omlc.ogi.edu/spectra/. Retrieved February 18, 2014, from

Pyka, T., Schulz, R., Ale, A., & Ntziachristos, V. (2011). Revisiting the normalized Born approximation: effects of scattering. Optics Letters, 36(22), 4329–4331. doi:10.1364/OL.36.004329

Radrich, K., Ale, A., Ermolayev, V., & Ntziachristos, V. (2012). Improving limited-projection-angle fluorescence molecular tomography using a co-registered x-ray computed tomography scan. Journal of Biomedical Optics, 17(12), 126011–126011. doi:10.1117/1.JBO.17.12.126011

Sanan, D. A., Newland, D. L., Tao, R., Marcovina, S., Wang, J., Mooser, V., … Hobbs, H. H. (1998). Low density lipoprotein receptor-negative mice expressing human apolipoprotein B-100 develop complex atherosclerotic lesions on a chow diet: no accentuation by apolipoprotein(a). Proceedings of the National Academy of Sciences of the United States of America, 95(8), 4544–4549.

Sanz, J., & Fayad, Z. A. (2008). Imaging of atherosclerotic cardiovascular disease. Nature, 451(7181), 953–957. doi:10.1038/nature06803

Sosnovik, D. E., Nahrendorf, M., Deliolanis, N., Novikov, M., Aikawa, E., Josephson, L., … Ntziachristos, V. (2007). Fluorescence Tomography and Magnetic Resonance Imaging of Myocardial Macrophage Infiltration in Infarcted Myocardium In Vivo. Circulation, 115(11), 1384–1391. doi:10.1161/CIRCULATIONAHA.106.663351

Talanov, V. S., Regino, C. A. S., Kobayashi, H., Bernardo, M., Choyke, P. L., & Brechbiel, M. W. (2006). Dendrimer-Based Nanoprobe for Dual Modality Magnetic Resonance and Fluorescence Imaging. Nano Letters, 6(7), 1459–1463. doi:10.1021/nl060765q

Tardif, J.-C., Lesage, F., Harel, F., Romeo, P., & Pressacco, J. (2011). Imaging Biomarkers in Atherosclerosis Trials. Circulation: Cardiovascular Imaging, 4(3), 319–333. doi:10.1161/CIRCIMAGING.110.962001

Yalavarthy, P. K., Pogue, B. W., Dehghani, H., & Paulsen, K. D. (2007). Weight-matrix structured regularization provides optimal generalized least-squares estimate in diffuse optical tomography. Medical Physics, 34(6), 2085. doi:10.1118/1.2733803

Yuan, J., Bae, E., & Tai, X.-C. (2010). A study on continuous max-flow and min-cut approaches. In 2010 IEEE Conference on Computer Vision and Pattern Recognition (CVPR) (pp. 2217–2224). doi:10.1109/CVPR.2010.5539903

F. Leblond, K. M. Tichauer, R. W. Holt, F. El-Ghussein, and B. W. Pogue, "Toward whole-body optical imaging of rats using single-photon counting fluorescence tomography," Opt. Lett. 36(19), 3723–3725 (2011).

CHAPTER 6 GENERAL DISCUSSION

6.1 Article #1

6.1.1 System characterization

Corresponding to the first objective of the thesis, a combined fluorescence-US imaging system was developed. The fluorescence imaging subsystem was used to measure boundary fluorescent emission; the US subsystem was to delineate 3D interface of both the surface and the inclusion. Both fluorescence and US were performed in a raster-scanned fashion with motorized linear stage. For fluorescence, a single source-detector pair was scanned on the tissue surface with steps of 1 mm. For US, a single-element transducer was scanned in conjunction with a fluorescence probe. Thus, the irregular shape of tissue could be delineated and precisely co-registered with the reconstructed fluorescence images.

The system was characterized using two phantoms having different shapes, constitutions and dimensions. Phantom results showed that the fluorescence reconstruction image quality could be significantly improved using the US structural priors. Besides, proof-of-concept experiment with a mouse demonstrated the feasibility and potential of this combined imaging approach for in-vivo imaging with small animals. Therefore, this work exhibits a promising strategy for exploring anatomical and functional information at very low-cost (less than 9k$).

6.1.2 Limitations

Limitations are mainly due to the simplicity of this proposed system. First, the optical measurement recorded by scanning the single source-detector pair is less informative than a camera-based system would. Second, raster-scanning suggests longer acquisition time compared with system of camera-based detection. Moreover, our home-made US system needs to be

optimized towards an improved resolution of US images, which poses a challenge when trying to segment to gather a precise atlas for the whole body of small animals. As well, it would be even more difficult to image small objects in tissue, such as aorta in atherosclerotic imaging.

6.2 Article #2

6.2.1 System design

Following the Article #1, the fluorescence-US imaging system was upgraded in terms of sampling precision and reconstruction technique. For fluorescence imaging, the illumination was conducted point-by-point by a pair of motorized linear stages with steps of 2 mm at X and Y directions. In addition, the fluorescent emission was measured by an EMCCD camera in transmission mode. Again, controlled by the same linear stages, a single element US transducer was scanned with micrometer resolution at X and Y directions. Because the US transducer has a fixed focal length and was focused on the lesion, a profilometer was employed to extract the surface of tissue, thus providing supplementary information to the US image, hence benefiting the forward modeling and inverse problem.

6.2.2 Attenuation compensated born normalization and pattern based reconstruction

As extension, we proposed to compensate the attenuation involved in the BN approximation. With the ACBN method, fluorescence emission mapping was accurately recovered in phantoms using wide-field detection, not possible with the standard Born normalization. Finally, to take advantage of the enriched measurements on the detection side, a pattern-based reconstruction mechanism was employed showing accurate recovery of fluorescence information. A simulation study further demonstrated linearity, accuracy and

fidelity of this reconstruction mechanism. Using the phantom measurements again, an enhanced quantification of reconstruction was achieved with the ACBN method.

6.2.3 In-vivo imaging with preclinical tumorous mice

The system was applied in in-vivo study with preclinical tumorous mice. Following the administration of a molecular probe, activity of cancer cells could be revealed. With our proposed computational techniques, the tumor was accurately localized. Furthermore, the reconstructed fluorescence was in agreement with the ex-vivo result.

6.2.4 Limitations

First, the accuracy of the ACBN was compromised due to the variation of attenuation along the fluorescence propagation path. One potential solution would be to take into account only the measurement being co-linear to the illumination positions, which, unavoidably, would lose information from the experimental data. Second, the limited resolution and tissue contrast of US images challenged tissue recognition and image segmentation, which in turn brought difficulty for a precise forward modeling.

6.3 Article #3

6.3.1 Advantages

The last objective was to develop a MRI-guided FMT system targeted on atherosclerotic imaging with mice. To reach the MRI, long fibers were employed to collect photons in parallel to the MRI acquisition. With this configuration, all detection for each source could be recorded in one single snapshot by an EMCCD camera, thus exhibiting a fast imaging approach for this multi-modality imaging platform.

The benefits of this combined imaging system are twofold. First, the MRI anatomy benefited the forward model, which in this version, takes into account the heterogeneities of different tissue types. This benefit was evaluated by phantom and mice corpses comparing heterogeneous models with homogeneous ones, showing an improved quantization of fluorescence reconstruction when using heterogeneous modeling. Second, small objects, such as aorta in mice, could be visualized anatomically by MRI, thereby, guide the localization of fluorescence reconstruction.

6.3.2 Atherosclerotic imaging with mice

Finally, the FMT-MRI system was applied in in-vivo atherosclerotic imaging. Following administration of a molecular probe, fluorescence signal was detected, which revealed the MMPs activity involved in the progression of atherosclerosis. Reconstructed using the heterogeneous models derived from MR anatomy, the fluorescence yield from the hearts and aortas were in accordance with the *ex vivo* measurements.

6.3.3 Limitations

Limitations remain in this study. First, coarse segmentations of the MR anatomies and the inadequacy of literature values might induce modeling error. It might be expected that better known tissue properties derived by additional technique could optimize forward modeling. Besides, although a soft-prior could constrain and thus obtain better quantitative reconstructions, such priors are not always achievable in *in vivo* experiments. As in this study, heart and aorta are the major targets for atherosclerotic imaging, MMPs activated fluorescence was found more broadly from the body of mice. For example, lungs were found to have considerable amount of fluorescence. Furthermore, a more advanced detection mechanism could enhance the SNR of measurement so that the reliance of prior on reconstruction could be alleviated.

CHAPTER 7 CONCLUSION

In this thesis, fluorescence imaging was combined with supplemental anatomical imaging modalities, such as US and MRI. We first presented a fluorescence-US system to explore both structural and functional information of imaging objects. Although low-cost, phantom results demonstrated that the US structural prior could still benefit the fluorescence reconstruction significantly. A proof-of-concept in-vivo experiment with a mouse further verified the feasibility of this combined imaging approach for future animal studies. Following the first work, the fluorescence-US imaging system was optimized with an EMCCD camera and motorized scanning of micrometers resolution. In addition, a profilometer was employed to measure the 3D surface of the imaging objects, in addition to the US anatomy. These improvements were specific to the issues which limited the first version of fluorescence-US system. Besides, working with phantoms, the ACBN method associated with the pattern based reconstruction algorithm resulted in improved recovery of fluorescence with respect to quantification and localization. This combined system was ultimately applied to in-vivo imaging with preclinical timorous mice. The in-vivo results exhibited good correlation with ex-vivo measurement. However, the limited resolution of the US images challenged the application in atherosclerotic imaging. To address that, we proposed a MRI-guided FMT system to explore anatomy with high spatial resolution, expecting to better guide fluorescence reconstruction and interpret functional information. Derived by the MR anatomies, the benefits of heterogeneous forward modeling were demonstrated in experiments encompassing phantom and mouse corpse. Finally, the system was applied to atherosclerotic imaging with mice. The reconstructions with the heterogeneous models showed higher fidelity to the *ex vivo* measurements when compared to the homogeneous models. Therefore, the proposed MRI-guided FMT system associated with the reconstruction method

might serve as a tool for atherosclerosis imaging of small animals. In conclusion, multi-modality diffuse fluorescence imaging was studied with this thesis. Different imaging modalities, such as US and MRI were explored as supplement for better recovery and interpretation of fluorescence images. Results of phantoms and in-vivo mice experiments suggested that the benefits from supplementary imaging modalities were unique; and significant outcome in preclinical study could be expected by multi-modality fluorescence imaging.

REFERENCES

Abascal, J. F. P.-J., Aguirre, J., Chamorro-Servent, J., Schweiger, M., Arridge, S., Ripoll, J., … Desco, M. (2012). Influence of absorption and scattering on the quantification of fluorescence diffuse optical tomography using normalized data. *Journal of Biomedical Optics*, *17*(3), 0360131–0360139. doi:10.1117/1.JBO.17.3.036013

Abascal, J. F. P.-J., Chamorro-Servent, J., Aguirre, J., Arridge, S., Correia, T., Ripoll, J., … Desco, M. (2011). Fluorescence diffuse optical tomography using the split Bregman method. *Medical Physics*, *38*(11), 6275–6284. doi:10.1118/1.3656063

Aikawa, E., Nahrendorf, M., Sosnovik, D., Lok, V. M., Jaffer, F. A., Aikawa, M., & Weissleder, R. (2007). Multimodality Molecular Imaging Identifies Proteolytic and Osteogenic Activities in Early Aortic Valve Disease. *Circulation*, *115*(3), 377–386. doi:10.1161/CIRCULATIONAHA.106.654913

Ale, A., Ermolayev, V., Deliolanis, N. C., & Ntziachristos, V. (2013). Fluorescence background subtraction technique for hybrid fluorescence molecular tomography/x-ray computed tomography imaging of a mouse model of early stage lung cancer. *Journal of Biomedical Optics*, *18*(5), 056006–056006. doi:10.1117/1.JBO.18.5.056006

Ale, A., Ermolayev, V., Herzog, E., Cohrs, C., de Angelis, M. H., & Ntziachristos, V. (2012a). FMT-XCT: in vivo animal studies with hybrid fluorescence molecular tomography-X-ray computed tomography. *Nature Methods*, *9*(6), 615–620. doi:10.1038/nmeth.2014

Ale, A., Ermolayev, V., Herzog, E., Cohrs, C., de Angelis, M. H., & Ntziachristos, V. (2012b). FMT-XCT: in vivo animal studies with hybrid fluorescence molecular tomography-X-ray computed tomography. *Nature Methods*, *9*(6), 615–620. doi:10.1038/nmeth.2014

Ale, A., Schulz, R. B., Sarantopoulos, A., & Ntziachristos, V. (2010). Imaging performance of a hybrid x-ray computed tomography-fluorescence molecular tomography system using priors. *Medical Physics*, *37*(5), 1976–1986.

Alexandrakis, G., Rannou, F. R., & Chatziioannou, A. F. (2005). Tomographic bioluminescence imaging by use of a combined optical-PET (OPET) system: a computer simulation feasibility study. *Physics in Medicine and Biology*, *50*(17), 4225–4241. doi:10.1088/0031-9155/50/17/021

Arridge, S. R., & Schotland, J. C. (2009). Optical tomography: forward and inverse problems. *Inverse Problems*, *25*(12), 123010. doi:10.1088/0266-5611/25/12/123010

Axelsson, J., Davis, S. C., Gladstone, D. J., & Pogue, B. W. (2011). Cerenkov emission induced by external beam radiation stimulates molecular fluorescence. *Medical Physics*, *38*(7), 4127–4132.

Basevi, H. R. A., Tichauer, K. M., Leblond, F., Dehghani, H., Guggenheim, J. A., Holt, R. W., & Styles, I. B. (2012). Compressive sensing based reconstruction in bioluminescence tomography improves image resolution and robustness to noise. *Biomedical Optics Express*, *3*(9), 2131–2141. doi:10.1364/BOE.3.002131

Bec, J., Xie, H., Yankelevich, D. R., Zhou, F., Sun, Y., Ghata, N., … Marcu, L. (2012). Design, construction, and validation of a rotary multifunctional intravascular diagnostic catheter combining multispectral fluorescence lifetime imaging and intravascular ultrasound. *Journal of Biomedical Optics*, *17*(10), 1060121–10601210. doi:10.1117/1.JBO.17.10.106012

Behrooz, A., Zhou, H.-M., Eftekhar, A. A., & Adibi, A. (2012). Total variation regularization for 3D reconstruction in fluorescence tomography: experimental phantom studies. *Applied Optics*, *51*(34), 8216–8227.

Bélanger, S., Abran, M., Intes, X., Casanova, C., & Lesage, F. (2010). Real-time diffuse optical tomography based on structured illumination. *Journal of Biomedical Optics*, *15*(1), 016006. doi:10.1117/1.3290818

Björn, S., Ntziachristos, V., & Schulz, R. (2010). Mesoscopic epifluorescence tomography: reconstruction of superficial and deep fluorescence in highly-scattering media. *Optics Express*, *18*(8), 8422–8429.

Boas, D., Culver, J., Stott, J., & Dunn, A. (2002). Three dimensional Monte Carlo code for photon migration through complex heterogeneous media including the adult human head. *Optics Express*, *10*(3), 159–170.

Boffety, M., Allain, M., Sentenac, A., Massonneau, M., & Carminati, R. (2011). Cramer-Rao analysis of steady-state and time-domain fluorescence diffuse optical imaging. *Biomedical Optics Express*, *2*(6), 1626–1636. doi:10.1364/BOE.2.001626

Boutet, J., Saroul, L., Duboeuf, F., Herve, L., Debourdeau, M., Vray, D., … Dinten, J.-M. (2009). Bimodal ultrasound and fluorescence approach for prostate cancer diagnosis. *Journal of Biomedical Optics*, *14*(6), 064001–064001–7. doi:10.1117/1.3257236

Brooksby, B. A., Dehghani, H., Pogue, B. W., & Paulsen, K. D. (2003). Near-infrared (NIR) tomography breast image reconstruction with a priori structural information from MRI: algorithm development for reconstructing heterogeneities. *Selected Topics in Quantum Electronics, IEEE Journal of*, *9*(2), 199–209. doi:10.1109/JSTQE.2003.813304

Calfon, M. A., Vinegoni, C., Ntziachristos, V., & Jaffer, F. A. (2010). Intravascular near-infrared fluorescence molecular imaging of atherosclerosis: toward coronary arterial visualization of biologically high-risk plaques. *Journal of Biomedical Optics*, *15*(1), 011107–011107–6. doi:10.1117/1.3280282

Cao, L., & Peter, J. (2013). Investigating line- versus point-laser excitation for three-dimensional fluorescence imaging and tomography employing a trimodal imaging system. *Journal of Biomedical Optics*, *18*(6), 066015. doi:10.1117/1.JBO.18.6.066015

Cao, X., Wang, X., Zhang, B., Liu, F., Luo, J., & Bai, J. (2013). Accelerated image reconstruction in fluorescence molecular tomography using dimension reduction. *Biomedical Optics Express*, *4*(1), 1–14. doi:10.1364/BOE.4.000001

Carpenter, C. M., Rakow-Penner, R., Jiang, S., Daniel, B. L., Pogue, B. W., Glover, G. H., & Paulsen, K. D. (2010). Inspired gas-induced vascular change in tumors with magnetic-resonance-guided near-infrared imaging: human breast pilot study. *Journal of Biomedical Optics*, *15*(3), 036026. doi:10.1117/1.3430729

Chamorro-Servent, J., Abascal, J. F. P. J., Aguirre, J., Arridge, S., Correia, T., Ripoll, J., … Vaquero, J. J. (2013). Use of Split Bregman denoising for iterative reconstruction in fluorescence diffuse optical tomography. *Journal of Biomedical Optics*, *18*(7), 076016. doi:10.1117/1.JBO.18.7.076016

Chamorro-Servent, J., Aguirre, J., Ripoll, J., Vaquero, J. J., & Desco, M. (2011). Feasibility of U-curve method to select the regularization parameter for fluorescence diffuse optical tomography in phantom and small animal studies. *Optics Express*, *19*(12), 11490–11506.

Chatni, M. R., Li, G., & Porterfield, D. M. (2009). Frequency-domain fluorescence lifetime optrode system design and instrumentation without a concurrent reference light-emitting diode. *Applied Optics*, *48*(29), 5528–5536.

Chaudhari, A. J., Ahn, S., Levenson, R., Badawi, R. D., Cherry, S. R., & Leahy, R. M. (2009). Excitation spectroscopy in multispectral optical fluorescence tomography: methodology, feasibility and computer simulation studies. *Physics in Medicine and Biology*, *54*(15), 4687–4704. doi:10.1088/0031-9155/54/15/004

Chaudhari, A. J., Darvas, F., Bading, J. R., Moats, R. A., Conti, P. S., Smith, D. J., … Leahy, R. M. (2005). Hyperspectral and multispectral bioluminescence optical tomography for small animal imaging. *Physics in Medicine and Biology*, *50*(23), 5421–5441.

Chen, H. H., Mekkaoui, C., Cho, H., Ngoy, S., Marinelli, B., Waterman, P., … Sosnovik, D. E. (2013). Fluorescence tomography of rapamycin-induced autophagy and cardioprotection in vivo. *Circulation. Cardiovascular Imaging*, *6*(3), 441–447. doi:10.1161/CIRCIMAGING.112.000074

Chen, J., Venugopal, V., & Intes, X. (2011). Monte Carlo based method for fluorescence tomographic imaging with lifetime multiplexing using time gates. *Biomedical Optics Express*, *2*(4), 871–886. doi:10.1364/BOE.2.000871

Chen, J., Venugopal, V., Lesage, F., & Intes, X. (2010). Time-resolved diffuse optical tomography with patterned-light illumination and detection. *Optics Letters*, *35*(13), 2121–2123. doi:10.1364/OL.35.002121

Choi, H. Y., Ryu, S. Y., Kim, J. Y., Kim, G. H., Park, S. J., Lee, B. H., & Chang, K. S. (2011). Microlensed dual-fiber probe for depth-resolved fluorescence measurements. *Optics Express*, *19*(15), 14172–14181.

Choi, M., Choi, K., Ryu, S.-W., Lee, J., & Choi, C. (2011). Dynamic fluorescence imaging for multiparametric measurement of tumor vasculature. *Journal of Biomedical Optics*, *16*(4), 046008. doi:10.1117/1.3562956

Cooley, B. C. (2011). In Vivo Fluorescence Imaging of Large-Vessel Thrombosis in Mice. *Arteriosclerosis, Thrombosis, and Vascular Biology*, *31*(6), 1351–1356. doi:10.1161/ATVBAHA.111.225334

Correia, T., Rudge, T., Koch, M., Ntziachristos, V., & Arridge, S. (2013). Wavelet-based data and solution compression for efficient image reconstruction in fluorescence diffuse optical tomography. *Journal of Biomedical Optics*, *18*(8), 86008. doi:10.1117/1.JBO.18.8.086008

D'Andrea, C., Ducros, N., Bassi, A., Arridge, S., & Valentini, G. (2010). Fast 3D optical reconstruction in turbid media using spatially modulated light. *Biomedical Optics Express*, *1*(2), 471. doi:10.1364/BOE.1.000471

D'Andrea, C., Spinelli, L., Comelli, D., Valentini, G., & Cubeddu, R. (2005). Localization and quantification of fluorescent inclusions embedded in a turbid medium. *Physics in Medicine and Biology*, *50*(10), 2313–2327. doi:10.1088/0031-9155/50/10/009

Dancik, Y., Favre, A., Loy, C. J., Zvyagin, A. V., & Roberts, M. S. (2013). Use of multiphoton tomography and fluorescence lifetime imaging to investigate skin pigmentation in vivo. *Journal of Biomedical Optics*, *18*(2), 26022. doi:10.1117/1.JBO.18.2.026022

Darne, C. D., Lu, Y., Tan, I.-C., Zhu, B., Rasmussen, J. C., Smith, A. M., … Sevick-Muraca, E. M. (2012). A compact frequency-domain photon migration system for integration into commercial hybrid small animal imaging scanners for fluorescence tomography. *Physics in Medicine and Biology*, *57*(24), 8135–8152. doi:10.1088/0031-9155/57/24/8135

Davis, S. C., Dehghani, H., Wang, J., Jiang, S., Pogue, B. W., & Paulsen, K. D. (2007a). Image-guided diffuse optical fluorescence tomography implemented with Laplacian-type regularization. *Optics Express*, *15*(7), 4066–4082. doi:10.1364/OE.15.004066

Davis, S. C., Dehghani, H., Wang, J., Jiang, S., Pogue, B. W., & Paulsen, K. D. (2007b). Image-guided diffuse optical fluorescence tomography implemented with Laplacian-type regularization. *Optics Express*, *15*(7), 4066–4082.

Davis, S. C., Pogue, B. W., Springett, R., Leussler, C., Mazurkewitz, P., Tuttle, S. B., … Paulsen, K. D. (2008). Magnetic resonance-coupled fluorescence tomography scanner for molecular imaging of tissue. *The Review of Scientific Instruments*, *79*(6). doi:10.1063/1.2919131

Davis, S. C., Samkoe, K. S., O'Hara, J. A., Gibbs-Strauss, S. L., Paulsen, K. D., & Pogue, B. W. (2010). Comparing implementations of magnetic-resonance-guided fluorescence molecular tomography for diagnostic classification of brain tumors. *Journal of Biomedical Optics*, *15*(5), 051602. doi:10.1117/1.3483902

Dehghani, H., Eames, M. E., Yalavarthy, P. K., Davis, S. C., Srinivasan, S., Carpenter, C. M., … Paulsen, K. D. (2009). Near infrared optical tomography using NIRFAST: Algorithm for numerical model and image reconstruction. *Communications in Numerical Methods in Engineering*, *25*(6), 711–732. doi:10.1002/cnm.1162

Deliolanis, N. C., Dunham, J., Wurdinger, T., Figueiredo, J.-L., Tannous, B. A., Bakhos, T., & Ntziachristos, V. (2009). In-vivo imaging of murine tumors using complete-angle projection fluorescence molecular tomography. *Journal of Biomedical Optics*, *14*(3), 030509. doi:10.1117/1.3149854

Demers, J.-L., Davis, S. C., Zhang, R., Gladstone, D. J., & Pogue, B. W. (2013). Čerenkov excited fluorescence tomography using external beam radiation. *Optics Letters*, *38*(8), 1364–1366.

DiBenedetto, J., Capelle, G. A., & O'Neill, M. (2012). Time-resolved hyperspectral fluorescence spectroscopy using frequency-modulated excitation. *Journal of Applied Physics*, *112*(1), 013109. doi:10.1063/1.4731247

Ducros, N., Bassi, A., Valentini, G., Canti, G., Arridge, S., & D'Andrea, C. (2013). Fluorescence molecular tomography of an animal model using structured light rotating view acquisition. *Journal of Biomedical Optics*, *18*(2), 20503. doi:10.1117/1.JBO.18.2.020503

Ducros, N., Bassi, A., Valentini, G., Schweiger, M., Arridge, S., & D'Andrea, C. (2011). Multiple-view fluorescence optical tomography reconstruction using compression of experimental data. *Optics Letters*, *36*(8), 1377–1379.

Ducros, N., D'Andrea, C., Bassi, A., Valentini, G., & Arridge, S. (2012). A virtual source pattern method for fluorescence tomography with structured light. *Physics in Medicine and Biology*, *57*(12), 3811. doi:10.1088/0031-9155/57/12/3811

Ducros, N., D'andrea, C., Valentini, G., Rudge, T., Arridge, S., & Bassi, A. (2010). Full-wavelet approach for fluorescence diffuse optical tomography with structured illumination. *Optics Letters*, *35*(21), 3676. doi:10.1364/OL.35.003676

Ducros, N., Da Silva, A., Hervé, L., Dinten, J.-M., & Peyrin, F. (2009). A comprehensive study of the use of temporal moments in time-resolved diffuse optical tomography: part II. Three-dimensional reconstructions. *Physics in Medicine and Biology*, *54*(23), 7107–7119. doi:10.1088/0031-9155/54/23/005

Ducros, N., Hervé, L., Da Silva, A., Dinten, J.-M., & Peyrin, F. (2009). A comprehensive study of the use of temporal moments in time-resolved diffuse optical tomography: part I. Theoretical material. *Physics in Medicine and Biology*, *54*(23), 7089–7105. doi:10.1088/0031-9155/54/23/004

Dutta, J., Ahn, S., Joshi, A. A., & Leahy, R. M. (2010). Illumination pattern optimization for fluorescence tomography: theory and simulation studies. *Physics in Medicine and Biology*, *55*(10), 2961–2982. doi:10.1088/0031-9155/55/10/011

Dutta, J., Ahn, S., Li, C., Cherry, S. R., & Leahy, R. M. (2012). Joint L1 and total variation regularization for fluorescence molecular tomography. *Physics in Medicine and Biology*, *57*(6), 1459–1476. doi:10.1088/0031-9155/57/6/1459

Elder, A. D., Kaminski, C. F., & Frank, J. H. (2009). phi2FLIM: a technique for alias-free frequency domain fluorescence lifetime imaging. *Optics Express*, *17*(25), 23181–23203.

Erickson, S. J., Martinez, S. L., DeCerce, J., Romero, A., Caldera, L., & Godavarty, A. (2013). Three-dimensional fluorescence tomography of human breast tissues in vivo using a hand-held optical imager. *Physics in Medicine and Biology*, *58*(5), 1563–1579. doi:10.1088/0031-9155/58/5/1563

Erickson, S. J., Martinez, S. L., Gonzalez, J., Caldera, L., & Godavarty, A. (2010). Improved detection limits using a hand-held optical imager with coregistration capabilities. *Biomedical Optics Express*, *1*(1), 126–134. doi:10.1364/BOE.1.000126

Erten, A., Hall, D., Hoh, C., Tran Cao, H. S., Kaushal, S., Esener, S., … Makale, M. (2010). Enhancing magnetic resonance imaging tumor detection with fluorescence intensity and lifetime imaging. *Journal of Biomedical Optics*, *15*(6), 066012. doi:10.1117/1.3509111

Fang, Q. (2010). Mesh-based Monte Carlo method using fast ray-tracing in Plücker coordinates. *Biomedical Optics Express*, *1*(1), 165. doi:10.1364/BOE.1.000165

Fang, Q., & Boas, D. A. (2009). Monte Carlo simulation of photon migration in 3D turbid media accelerated by graphics processing units. *Optics Express*, *17*(22), 20178–20190. doi:10.1364/OE.17.020178

Fang, Q., Moore, R. H., Kopans, D. B., & Boas, D. A. (2010). Compositional-prior-guided image reconstruction algorithm for multi-modality imaging. *Biomedical Optics Express*, *1*(1), 223–235. doi:10.1364/BOE.1.000223

Fatakdawala, H., Poti, S., Zhou, F., Sun, Y., Bec, J., Liu, J., … Marcu, L. (2013). Multimodal in vivo imaging of oral cancer using fluorescence lifetime, photoacoustic and ultrasound techniques. *Biomedical Optics Express*, *4*(9), 1724–1741. doi:10.1364/BOE.4.001724

Flynn, B. P., DSouza, A. V., Kanick, S. C., Davis, S. C., & Pogue, B. W. (2013). White light-informed optical properties improve ultrasound-guided fluorescence tomography of photoactive protoporphyrin IX. *Journal of Biomedical Optics*, *18*(4), 046008–046008. doi:10.1117/1.JBO.18.4.046008

Fortin, P.-Y., Genevois, C., Koenig, A., Heinrich, E., Texier, I., & Couillaud, F. (2012). Detection of brain tumors using fluorescence diffuse optical tomography and nanoparticles as contrast agents. *Journal of Biomedical Optics*, *17*(12), 126004. doi:10.1117/1.JBO.17.12.126004

Freiberger, M., Clason, C., & Scharfetter, H. (2010). Total variation regularization for nonlinear fluorescence tomography with an augmented Lagrangian splitting approach. *Applied Optics*, *49*(19), 3741–3747.

Freiberger, M., Egger, H., Liebmann, M., & Scharfetter, H. (2011). High-performance image reconstruction in fluorescence tomography on desktop computers and graphics hardware. *Biomedical Optics Express*, *2*(11), 3207–3222. doi:10.1364/BOE.2.003207

Fu, G., Meng, L.-J., Eng, P., Newville, M., Vargas, P., & Riviere, P. L. (2013). Experimental demonstration of novel imaging geometries for x-ray fluorescence computed tomography. *Medical Physics*, *40*(6), 061903. doi:10.1118/1.4801907

Gao, F., Li, J., Zhang, L., Poulet, P., Zhao, H., & Yamada, Y. (2010). Simultaneous fluorescence yield and lifetime tomography from time-resolved transmittances of small-animal-sized phantom. *Applied Optics*, *49*(16), 3163–3172.

Gao, F., Zhao, H., & Yamada, Y. (2002). Improvement of Image Quality in Diffuse Optical Tomography by use of Full Time-Resolved Data. *Applied Optics*, *41*(4), 778–791. doi:10.1364/AO.41.000778

Ge, J., Erickson, S. J., & Godavarty, A. (2010). Multi-projection fluorescence optical tomography using a handheld-probe-based optical imager: phantom studies. *Applied Optics*, *49*(23), 4343–4354.

Gibbs-Strauss, S. L., O'Hara, J. A., Srinivasan, S., Hoopes, P. J., Hasan, T., & Pogue, B. W. (2009). Diagnostic detection of diffuse glioma tumors in vivo with molecular fluorescent probe-based transmission spectroscopy. *Medical Physics*, *36*(3), 974–983. doi:10.1118/1.3075770

Gibson, A. P., Hebden, J. C., & Arridge, S. R. (2005). Recent advances in diffuse optical imaging. *Physics in Medicine and Biology*, *50*(4), R1–R43.

Gioux, S., Lomnes, S. J., Choi, H. S., & Frangioni, J. V. (2010). Low-frequency wide-field fluorescence lifetime imaging using a high-power near-infrared light-emitting diode light source. *Journal of Biomedical Optics*, *15*(2), 026005. doi:10.1117/1.3368997

Goergen, C. J., Chen, H. H., Bogdanov, A., Sosnovik, D. E., & Kumar, A. T. N. (2012). In vivo fluorescence lifetime detection of an activatable probe in infarcted myocardium. *Journal of Biomedical Optics*, *17*(5), 056001. doi:10.1117/1.JBO.17.5.056001

Goiffon, R. J., Akers, W. J., Berezin, M. Y., Lee, H., & Achilefu, S. (2009). Dynamic noninvasive monitoring of renal function in vivo by fluorescence lifetime imaging. *Journal of Biomedical Optics*, *14*(2), 020501. doi:10.1117/1.3095800

Gorpas, D., & Andersson-Engels, S. (2012). Evaluation of a radiative transfer equation and diffusion approximation hybrid forward solver for fluorescence molecular imaging. *Journal of Biomedical Optics*, *17*(12), 126010. doi:10.1117/1.JBO.17.12.126010

Graves, E. E., Ripoll, J., Weissleder, R., & Ntziachristos, V. (2003). A submillimeter resolution fluorescence molecular imaging system for small animal imaging. *Medical Physics*, *30*(5), 901–911.

Grosenick, D., Hagen, A., Steinkellner, O., Poellinger, A., Burock, S., Schlag, P. M., … Macdonald, R. (2011). A multichannel time-domain scanning fluorescence mammograph: performance assessment and first in vivo results. *The Review of Scientific Instruments*, *82*(2), 024302. doi:10.1063/1.3543820

Gruber, J. D., Paliwal, A., Krishnaswamy, V., Ghadyani, H., Jermyn, M., O'Hara, J. A., … Pogue, B. W. (2010a). System development for high frequency ultrasound-guided fluorescence quantification of skin layers. *Journal of Biomedical Optics*, *15*(2), 026028. doi:10.1117/1.3374040

Gruber, J. D., Paliwal, A., Krishnaswamy, V., Ghadyani, H., Jermyn, M., O'Hara, J. A., … Pogue, B. W. (2010b). System development for high frequency ultrasound-guided fluorescence quantification of skin layers. *Journal of Biomedical Optics*, *15*(2), 026028–5.

Guven, M., Yazici, B., Intes, X., & Chance, B. (2005). Diffuse optical tomography with a priori anatomical information. *Physics in Medicine and Biology*, *50*(12), 2837–2858. doi:10.1088/0031-9155/50/12/008

Hagen, A., Grosenick, D., Macdonald, R., Rinneberg, H., Burock, S., Warnick, P., … Schlag, P. M. (2009). Late-fluorescence mammography assesses tumor capillary permeability and differentiates malignant from benign lesions. *Optics Express*, *17*(19), 17016–17033.

Han, D., Tian, J., Zhu, S., Feng, J., Qin, C., Zhang, B., & Yang, X. (2010). A fast reconstruction algorithm for fluorescence molecular tomography with sparsity regularization. *Optics Express*, *18*(8), 8630–8646.

Hansen, P. C., & O'Leary, D. P. (1993). The Use of the L-Curve in the Regularization of Discrete Ill-Posed Problems. *SIAM Journal on Scientific Computing*, *14*(6), 1487–1503. doi:10.1137/0914086

He, B., Xi, L., Samuelson, S. R., Xie, H., Yang, L., & Jiang, H. (2012). Microelectromechanical systems scanning-mirror-based handheld probe for fluorescence molecular tomography. *Applied Optics*, *51*(20), 4678–4683.

Hight, M. R., Nolting, D. D., McKinley, E. T., Lander, A. D., Wyatt, S. K., Gonyea, M., … Manning, H. C. (2011). Multispectral fluorescence imaging to assess pH in biological specimens. *Journal of Biomedical Optics*, *16*(1), 016007. doi:10.1117/1.3533264

Hillman, E. M. C., & Moore, A. (2007). All-optical anatomical co-registration for molecular imaging of small animals using dynamic contrast. *Nature Photonics*, *1*(9), 526–530. doi:10.1038/nphoton.2007.146

Hoffman, R. (2002). Green fluorescent protein imaging of tumour growth, metastasis, and angiogenesis in mouse models. *The Lancet Oncology*, *3*(9), 546–556.

Holboke, M. J., Tromberg, B. J., Li, X., Shah, N., Fishkin, J., Kidney, D., … Yodh, A. G. (2000). Three-dimensional diffuse optical mammography with ultrasound localization in a human subject. *Journal of Biomedical Optics*, *5*(2), 237–247.

Holt, R. W., Tichauer, K. M., Dehghani, H., Pogue, B. W., & Leblond, F. (2012). Multiple-gate time domain diffuse fluorescence tomography allows more sparse tissue sampling without compromising image quality. *Optics Letters*, *37*(13), 2559–2561.

Intes, X., Maloux, C., Guven, M., Yazici, B., & Chance, B. (2004). Diffuse optical tomography with physiological and spatial a priori constraints. *Physics in Medicine and Biology*, *49*(12), N155–N163. doi:10.1088/0031-9155/49/12/N01

J, G., Sj, E., & A, G. (2009). Fluorescence Tomographic Imaging using a Hand-held Probe based Optical Imager: Extensive Phantom Studies. *Applied Optics, Applied Optics*, *48, 48*(33, 33), 6408, 6408–6416. doi:10.1364/AO.48.006408

Jaffer, F. A., Kim, D.-E., Quinti, L., Tung, C.-H., Aikawa, E., Pande, A. N., … Weissleder, R. (2007). Optical Visualization of Cathepsin K Activity in Atherosclerosis With a Novel, Protease-Activatable Fluorescence Sensor. *Circulation*, *115*(17), 2292–2298. doi:10.1161/CIRCULATIONAHA.106.660340

Jaffer, F. A., Libby, P., & Weissleder, R. (2007). Molecular imaging of cardiovascular disease. *Circulation*, *116*(9), 1052–1061. doi:10.1161/CIRCULATIONAHA.106.647164

Jaffer, F. A., Libby, P., & Weissleder, R. (2009a). Optical and Multimodality Molecular Imaging. Insights Into Atherosclerosis. *Arterioscler Thromb Vasc Biol*, ATVBAHA.108.165530. doi:10.1161/ATVBAHA.108.165530

Jaffer, F. A., Libby, P., & Weissleder, R. (2009b). Optical and multimodality molecular imaging: insights into atherosclerosis. *Arteriosclerosis, Thrombosis, and Vascular Biology*, *29*(7), 1017–1024. doi:10.1161/ATVBAHA.108.165530

Kavuri, V. C., Lin, Z.-J., Tian, F., & Liu, H. (2012). Sparsity enhanced spatial resolution and depth localization in diffuse optical tomography. *Biomedical Optics Express*, *3*(5), 943–957. doi:10.1364/BOE.3.000943

Kepshire, D. L., Dehghani, H., Leblond, F., & Pogue, B. W. (2009). Automatic exposure control and estimation of effective system noise in diffuse fluorescence tomography. *Optics Express*, *17*(25), 23272–23283.

Kepshire, D., Mincu, N., Hutchins, M., Gruber, J., Dehghani, H., Hypnarowski, J., … Pogue, B. W. (2009). A microcomputed tomography guided fluorescence tomography system for small animal molecular imaging. *The Review of Scientific Instruments*, *80*(4), 043701. doi:10.1063/1.3109903

Kepshire, D. S., Gibbs-Strauss, S. L., Gibbs-Struass, S. L., O'Hara, J. A., Hutchins, M., Mincu, N., … Pogue, B. W. (2009). Imaging of glioma tumor with endogenous fluorescence tomography. *Journal of Biomedical Optics*, *14*(3), 030501. doi:10.1117/1.3127202

Klose, A. D., & Pöschinger, T. (2011). Excitation-resolved fluorescence tomography with simplified spherical harmonics equations. *Physics in Medicine and Biology*, *56*(5), 1443–1469. doi:10.1088/0031-9155/56/5/015

Konecky, S. D., Owen, C. M., Rice, T., Valdés, P. A., Kolste, K., Wilson, B. C., … Tromberg, B. J. (2012). Spatial frequency domain tomography of protoporphyrin IX fluorescence in preclinical glioma models. *Journal of Biomedical Optics*, *17*(5), 056008. doi:10.1117/1.JBO.17.5.056008

Korideck, H., & Peterson, J. D. (2008). Noninvasive, in vivo quantification of asthma severity using fluorescence molecular tomography. *Nature Methods | Application Notes*. doi:10.1038/nmeth.f.218

Kumar, A. T. N. (2012). Direct Monte Carlo computation of time-resolved fluorescence in heterogeneous turbid media. *Optics Letters*, *37*(22), 4783–4785.

Kumar, A. T. N., Raymond, S. B., Dunn, A. K., Bacskai, B. J., & Boas, D. A. (2008). A time domain fluorescence tomography system for small animal imaging. *IEEE Transactions on Medical Imaging*, *27*(8), 1152–1163. doi:10.1109/TMI.2008.918341

Kwon, S., Agollah, G. D., Wu, G., Chan, W., & Sevick-Muraca, E. M. (2013). Direct visualization of changes of lymphatic function and drainage pathways in lymph node metastasis of B16F10 melanoma using near-infrared fluorescence imaging. *Biomedical Optics Express*, *4*(6), 967–977. doi:10.1364/BOE.4.000967

Kwon, S., & Sevick-Muraca, E. M. (2011). Mouse phenotyping with near-infrared fluorescence lymphatic imaging. *Biomedical Optics Express*, *2*(6), 1403. doi:10.1364/BOE.2.001403

Laidevant, A., Hervé, L., Debourdeau, M., Boutet, J., Grenier, N., & Dinten, J.-M. (2011). Fluorescence time-resolved imaging system embedded in an ultrasound prostate probe. *Biomedical Optics Express*, *2*(1), 194–206. doi:10.1364/BOE.2.000194

Lam, S., Lesage, F., & Intes, X. (2005). Time Domain Fluorescent Diffuse Optical Tomography: analytical expressions. *Optics Express*, *13*(7), 2263–2275.

Landragin-Frassati, A., Dinten, J.-M., Georges, D., & Da Silva, A. (2009). Model reduction using wavelet multiresolution technique applied to fluorescence diffuse optical tomography. *Applied Optics*, *48*(36), 6878–6892.

Langsner, R. J., Middleton, L. P., Sun, J., Meric-Bernstam, F., Hunt, K. K., Drezek, R. A., & Yu, T. K. (2011). Wide-field imaging of fluorescent deoxy-glucose in ex vivo malignant and normal breast tissue. *Biomedical Optics Express*, *2*(6), 1514–1523. doi:10.1364/BOE.2.001514

Lapointe, E., Pichette, J., & Bérubé-Lauzière, Y. (2012). A multi-view time-domain non-contact diffuse optical tomography scanner with dual wavelength detection for intrinsic and fluorescence small animal imaging. *The Review of Scientific Instruments*, *83*(6), 063703. doi:10.1063/1.4726016

Larsen, E. L. P., Randeberg, L. L., Olstad, E., Haugen, O. A., Aksnes, A., & Svaasand, L. O. (2011). Hyperspectral imaging of atherosclerotic plaques in vitro. *Journal of Biomedical Optics*, *16*(2), 026011. doi:10.1117/1.3540657

Leavesley, S., Jiang, Y., Patsekin, V., Rajwa, B., & Robinson, J. P. (2008). An excitation wavelength-scanning spectral imaging system for preclinical imaging. *The Review of Scientific Instruments*, *79*(2 Pt 1), 023707. doi:10.1063/1.2885043

Leblond, F., Davis, S. C., Valdés, P. A., & Pogue, B. W. (2010). Pre-clinical whole-body fluorescence imaging: Review of instruments, methods and applications. *Journal of Photochemistry and Photobiology. B, Biology*, *98*(1), 77–94. doi:10.1016/j.jphotobiol.2009.11.007

Leblond, F., Kepshire, D., O'Hara, J. A., Dehghani, H., Srinivasan, S., Mincu, N., … Pogue, B. W. (2009). Imaging protoporphyrin IX fluorescence with a time-domain FMT/microCT

system. In *Proceedings of SPIE* (pp. 717106–717106–10). San Jose, CA, USA. doi:10.1117/12.809267

Leblond, F., Ovanesyan, Z., Davis, S. C., Valdés, P. A., Kim, A., Hartov, A., … Roberts, D. W. (2011). Analytic expression of fluorescence ratio detection correlates with depth in multi-spectral sub-surface imaging. *Physics in Medicine and Biology*, *56*(21), 6823–6837. doi:10.1088/0031-9155/56/21/005

Leblond, F., Tichauer, K. M., Holt, R. W., El-Ghussein, F., & Pogue, B. W. (2011). Toward whole-body optical imaging of rats using single-photon counting fluorescence tomography. *Optics Letters*, *36*(19), 3723–3725.

Lehtikangas, O., Tarvainen, T., & Kim, A. D. (2012). Modeling boundary measurements of scattered light using the corrected diffusion approximation. *Biomedical Optics Express*, *3*(3), 552–571. doi:10.1364/BOE.3.000552

Leproux, A., van der Voort, M., van der Mark, M. B., Harbers, R., van de Ven, S. M. W. Y., & van Leeuwen, T. G. (2011). Optical mammography combined with fluorescence imaging: lesion detection using scatterplots. *Biomedical Optics Express*, *2*(4), 1007–1020. doi:10.1364/BOE.2.001007

Li, B., Abran, M., Matteau-Pelletier, C., Rouleau, L., Lam, T., Sharma, R., … Lesage, F. (2011). Low-cost three-dimensional imaging system combining fluorescence and ultrasound. *Journal of Biomedical Optics*, *16*(12), 126010–126010–10. doi:doi:10.1117/1.3662455

Li, B., & Lesage, F. (2012). Ultrasound guided fluorescence tomography, 841208–841208. doi:10.1117/12.2001441

Li, C., Wang, G., Qi, J., & Cherry, S. R. (2009). Three-dimensional fluorescence optical tomography in small-animal imaging using simultaneous positron-emission-tomography priors. *Optics Letters*, *34*(19), 2933–2935.

Li, J., Wang, X., Yi, X., Zhang, L., Zhou, Z., Zhao, H., & Gao, F. (2012). Towards pH-sensitive imaging of small animals with photon-counting difference diffuse fluorescence tomography. *Journal of Biomedical Optics*, *17*(9), 96011–96011. doi:10.1117/1.JBO.17.9.096011

Li, Z., & Niedre, M. (2011). Hybrid use of early and quasi-continuous wave photons in time-domain tomographic imaging for improved resolution and quantitative accuracy. *Biomedical Optics Express*, *2*(3), 665–679. doi:10.1364/BOE.2.000665

Liemert, A., & Kienle, A. (2012). Infinite space Green's function of the time-dependent radiative transfer equation. *Biomedical Optics Express*, *3*(3), 543–551. doi:10.1364/BOE.3.000543

Lin, Y., Barber, W. C., Iwanczyk, J. S., Roeck, W., Nalcioglu, O., & Gulsen, G. (2010a). Quantitative fluorescence tomography using a combined tri-modality FT/DOT/XCT system. *Optics Express*, *18*(8), 7835–7850. doi:10.1364/OE.18.007835

Lin, Y., Barber, W. C., Iwanczyk, J. S., Roeck, W. W., Nalcioglu, O., & Gulsen, G. (2010b). Quantitative fluorescence tomography using a trimodality system: in vivo validation. *Journal of Biomedical Optics*, *15*(4), 040503–040503–3. doi:10.1117/1.3467495

Lin, Y., Gao, H., Nalcioglu, O., & Gulsen, G. (2007). Fluorescence diffuse optical tomography with functional and anatomical a priori information: feasibility study. *Physics in Medicine and Biology*, *52*(18), 5569–5585. doi:10.1088/0031-9155/52/18/007

Lin, Y., Ghijsen, M., Nalcioglu, O., & Gulsen, G. (2012). In vivo validation of quantitative frequency domain fluorescence tomography. *Journal of Biomedical Optics*, *17*(12), 126021–126021. doi:10.1117/1.JBO.17.12.126021

Lin, Y., Ghijsen, M. T., Gao, H., Liu, N., Nalcioglu, O., & Gulsen, G. (2011a). A photo-multiplier tube-based hybrid MRI and frequency domain fluorescence tomography system for small animal imaging. *Physics in Medicine and Biology*, *56*(15), 4731–4747. doi:10.1088/0031-9155/56/15/007

Lin, Y., Ghijsen, M. T., Gao, H., Liu, N., Nalcioglu, O., & Gulsen, G. (2011b). A photo-multiplier tube-based hybrid MRI and frequency domain fluorescence tomography system for small animal imaging. *Physics in Medicine and Biology*, *56*(15), 4731–4747. doi:10.1088/0031-9155/56/15/007

Liu, J., Sun, Y., Qi, J., & Marcu, L. (2012). A novel method for fast and robust estimation of fluorescence decay dynamics using constrained least-squares deconvolution with Laguerre expansion. *Physics in Medicine and Biology*, *57*(4), 843–865. doi:10.1088/0031-9155/57/4/843

Lu, Y., Zhu, B., Shen, H., Rasmussen, J. C., Wang, G., & Sevick-Muraca, E. M. (2010). A parallel adaptive finite element simplified spherical harmonics approximation solver for frequency domain fluorescence molecular imaging. *Physics in Medicine and Biology*, *55*(16), 4625–4645. doi:10.1088/0031-9155/55/16/002

Mallas, G., Brooks, D. H., Rosenthal, A., Nudelman, R. N., Mauskapf, A., Jaffer, F. A., & Ntziachristos, V. (2012). Improving quantification of intravascular fluorescence imaging using structural information. *Physics in Medicine and Biology*, *57*(20), 6395. doi:10.1088/0031-9155/57/20/6395

Markel, V. A., Mital, V., & Schotland, J. C. (2003). Inverse problem in optical diffusion tomography. III. Inversion formulas and singular-value decomposition. *Journal of the Optical Society of America A*, *20*(5), 890–902. doi:10.1364/JOSAA.20.000890

May, A., Bhaumik, S., Gambhir, S. S., Zhan, C., & Yazdanfar, S. (2009). Whole-body, real-time preclinical imaging of quantum dot fluorescence with time-gated detection. *Journal of Biomedical Optics*, *14*(6), 060504. doi:10.1117/1.3269675

Mazhar, A., Cuccia, D. J., Gioux, S., Durkin, A. J., Frangioni, J. V., & Tromberg, B. J. (2010). Structured illumination enhances resolution and contrast in thick tissue fluorescence imaging. *Journal of Biomedical Optics*, *15*(1), 010506. doi:10.1117/1.3299321

McGinty, J., Galletly, N. P., Dunsby, C., Munro, I., Elson, D. S., Requejo-Isidro, J., … Stamp, G. W. (2010). Wide-field fluorescence lifetime imaging of cancer. *Biomedical Optics Express*, *1*(2), 627–640. doi:10.1364/BOE.1.000627

Milej, D., Gerega, A., Zołek, N., Weigl, W., Kacprzak, M., Sawosz, P., … Liebert, A. (2012). Time-resolved detection of fluorescent light during inflow of ICG to the brain-a methodological study. *Physics in Medicine and Biology*, *57*(20), 6725–6742. doi:10.1088/0031-9155/57/20/6725

Milstein, A. B., Stott, J. J., Oh, S., Boas, D. A., Millane, R. P., Bouman, C. A., & Webb, K. J. (2004). Fluorescence optical diffusion tomography using multiple-frequency data. *Journal of the Optical Society of America. A, Optics, Image Science, and Vision*, *21*(6), 1035–1049.

Mo, W., Rohrbach, D., & Sunar, U. (2012). Imaging a photodynamic therapy photosensitizer in vivo with a time-gated fluorescence tomography system. *Journal of Biomedical Optics*, *17*(7), 071306. doi:10.1117/1.JBO.17.7.071306

Mohajerani, P., Adibi, A., Kempner, J., & Yared, W. (2009). Compensation of optical heterogeneity-induced artifacts in fluorescence molecular tomography: theory and in vivo validation. *Journal of Biomedical Optics*, *14*(3), 034021. doi:10.1117/1.3149855

Mohajerani, P., & Ntziachristos, V. (2013). Compression of Born ratio for fluorescence molecular tomography/x-ray computed tomography hybrid imaging: methodology and in vivo validation. *Optics Letters*, *38*(13), 2324–2326.

Montejo, L. D., Klose, A. D., & Hielscher, A. H. (2010). Implementation of the equation of radiative transfer on block-structured grids for modeling light propagation in tissue. *Biomedical Optics Express*, *1*(3), 861–878. doi:10.1364/BOE.1.000861

Montet, X., Figueiredo, J.-L., Alencar, H., Ntziachristos, V., Mahmood, U., & Weissleder, R. (2007). Tomographic fluorescence imaging of tumor vascular volume in mice. *Radiology*, *242*(3), 751–758. doi:10.1148/radiol.2423052065

Nahrendorf, M., Keliher, E., Marinelli, B., Waterman, P., Feruglio, P. F., Fexon, L., … Weissleder, R. (2010). Hybrid PET-optical imaging using targeted probes. *Proceedings of the National Academy of Sciences*, *107*(17), 7910–7915. doi:10.1073/pnas.0915163107

Nahrendorf, M., Waterman, P., Thurber, G., Groves, K., Rajopadhye, M., Panizzi, P., … Weissleder, R. (2009). Hybrid In Vivo FMT-CT Imaging of Protease Activity in Atherosclerosis With Customized Nanosensors. *Arterioscler Thromb Vasc Biol*, ATVBAHA.109.193086. doi:10.1161/ATVBAHA.109.193086

Najiminaini, M., Vasefi, F., Tichauer, K. M., Lee, T.-Y., Kaminska, B., & Carson, J. J. L. (2010). Angular domain fluorescence lifetime imaging: a tissue-like phantom study. *Optics Express*, *18*(22), 23247–23257.

Nakashima, Y., Plump, A., Raines, E., Breslow, J., & Ross, R. (1994). ApoE-deficient mice develop lesions of all phases of atherosclerosis throughout the arterial tree. *Arterioscler Thromb Vasc Biol.* Retrieved from http://atvb.ahajournals.org/cgi/content/abstract/14/1/133

Naser, M. A., & Patterson, M. S. (2010a). Algorithms for bioluminescence tomography incorporating anatomical information and reconstruction of tissue optical properties. *Biomedical Optics Express*, *1*(2), 512–526. doi:10.1364/BOE.1.000512

Naser, M. A., & Patterson, M. S. (2010b). Improved bioluminescence and fluorescence reconstruction algorithms using diffuse optical tomography, normalized data, and optimized selection of the permissible source region. *Biomedical Optics Express*, *2*(1), 169–184. doi:10.1364/BOE.2.000169

Nie, Z., An, R., Hayward, J. E., Farrell, T. J., & Fang, Q. (2013). Hyperspectral fluorescence lifetime imaging for optical biopsy. *Journal of Biomedical Optics*, *18*(9), 096001. doi:10.1117/1.JBO.18.9.096001

Niedre, M., & Ntziachristos, V. (2010). Comparison of fluorescence tomographic imaging in mice with early-arriving and quasi-continuous-wave photons. *Optics Letters*, *35*(3), 369–371.

Nothdurft, R. E., Patwardhan, S. V., Akers, W., Ye, Y., Achilefu, S., & Culver, J. P. (2009). In vivo fluorescence lifetime tomography. *Journal of Biomedical Optics*, *14*(2), 024004. doi:10.1117/1.3086607

Ntziachristos, V., Bremer, C., & Weissleder, R. (2003). Fluorescence imaging with near-infrared light: new technological advances that enable in vivo molecular imaging. *European Radiology*, *13*(1), 195–208. doi:10.1007/s00330-002-1524-x

Ntziachristos, V., & Weissleder, R. (2001). Experimental three-dimensional fluorescence reconstruction of diffuse media by use of a normalized Born approximation. *Optics Letters*, *26*(12), 893–895. doi:10.1364/OL.26.000893

Ntziachristos, V., & Weissleder, R. (2002). Charge-coupled-device based scanner for tomography of fluorescent near-infrared probes in turbid media. *Medical Physics*, *29*(5), 803–809.

Patel, N. L., Lin, Z.-J., Rathore, Y., Livingston, E. H., Liu, H., & Alexandrakis, G. (2010). Relative capacities of time-gated versus continuous-wave imaging to localize tissue embedded vessels with increasing depth. *Journal of Biomedical Optics*, *15*(1), 016015. doi:10.1117/1.3299728

Patwardhan, S., Bloch, S., Achilefu, S., & Culver, J. (2005). Time-dependent whole-body fluorescence tomography of probe bio-distributions in mice. *Optics Express*, *13*(7), 2564–2577. doi:10.1364/OPEX.13.002564

Pichette, J., Domínguez, J. B., & Bérubé-Lauzière, Y. (2013). Time-domain geometrical localization of point-like fluorescence inclusions in turbid media with early photon arrival times. *Applied Optics*, *52*(24), 5985–5999.

Pogue, B. W., Gibbs, S. L., Chen, B., & Savellano, M. (2004). Fluorescence imaging in vivo: raster scanned point-source imaging provides more accurate quantification than broad beam geometries. *Technology in Cancer Research & Treatment*, *3*(1), 15–21.

Prahl, S. A. (n.d.). Online resource: http://omlc.ogi.edu/spectra/. Retrieved February 18, 2014, from

Prahl, U., Holdfeldt, P., Bergström, G., Fagerberg, B., Hulthe, J., & Gustavsson, T. (2010). Percentage white: a new feature for ultrasound classification of plaque echogenicity in

carotid artery atherosclerosis. *Ultrasound in Medicine & Biology*, *36*(2), 218–226. doi:10.1016/j.ultrasmedbio.2009.10.002

Pu, H., He, W., Zhang, G., Zhang, B., Liu, F., Zhang, Y., … Bai, J. (2013). Separating structures of different fluorophore concentrations by principal component analysis on multispectral excitation-resolved fluorescence tomography images. *Biomedical Optics Express*, *4*(10), 1829–1845. doi:10.1364/BOE.4.001829

Puszka, A., Herve, L., Planat-Chretien, A., Koenig, A., Derouard, J., & Dinten, J.-M. (2013). Time-domain reflectance diffuse optical tomography with Mellin-Laplace transform for experimental detection and depth localization of a single absorbing inclusion. *Biomedical Optics Express*, *4*(4), 569–583. doi:10.1364/BOE.4.000569

Pyka, T., Schulz, R., Ale, A., & Ntziachristos, V. (2011). Revisiting the normalized Born approximation: effects of scattering. *Optics Letters*, *36*(22), 4329–4331. doi:10.1364/OL.36.004329

Rader, D. J., & Daugherty, A. (2008). Translating molecular discoveries into new therapies for atherosclerosis. *Nature*, *451*(7181), 904–913. doi:10.1038/nature06796

Radrich, K., Ale, A., Ermolayev, V., & Ntziachristos, V. (2012). Improving limited-projection-angle fluorescence molecular tomography using a co-registered x-ray computed tomography scan. *Journal of Biomedical Optics*, *17*(12), 126011–126011. doi:10.1117/1.JBO.17.12.126011

Raymond, S. B., Boas, D. A., Bacskai, B. J., & Kumar, A. T. N. (2010). Lifetime-based tomographic multiplexing. *Journal of Biomedical Optics*, *15*(4), 046011. doi:10.1117/1.3469797

Raymond, S. B., Kumar, A. T. N., Boas, D. A., & Bacskai, B. J. (2009). Optimal parameters for near infrared fluorescence imaging of amyloid plaques in Alzheimer's disease mouse models. *Physics in Medicine and Biology*, *54*(20), 6201–6216. doi:10.1088/0031-9155/54/20/011

Razansky, R. N., Rosenthal, A., Mallas, G., Razansky, D., Jaffer, F. A., & Ntziachristos, V. (2010). Near-infrared fluorescence catheter system for two-dimensional intravascular imaging in vivo. *Optics Express*, *18*(11), 11372–11381.

Rice, W. L., Hou, S., & Kumar, A. T. N. (2013). Resolution below the point spread function for diffuse optical imaging using fluorescence lifetime multiplexing. *Optics Letters*, *38*(12), 2038–2040.

Ricketts, K., Guazzoni, C., Castoldi, A., Gibson, A. P., & Royle, G. J. (2013). An x-ray fluorescence imaging system for gold nanoparticle detection. *Physics in Medicine and Biology*, *58*(21), 7841. doi:10.1088/0031-9155/58/21/7841

Ripplinger, C. M., Kessinger, C. W., Li, C., Kim, J. W., McCarthy, J. R., Weissleder, R., … Jaffer, F. A. (2012). Inflammation Modulates Murine Venous Thrombosis Resolution In Vivo: Assessment by Multimodal Fluorescence Molecular Imaging. *Arteriosclerosis, Thrombosis, and Vascular Biology*, *32*(11), 2616–2624. doi:10.1161/ATVBAHA.112.251983

Saager, R. B., Cuccia, D. J., Saggese, S., Kelly, K. M., & Durkin, A. J. (2011). Quantitative fluorescence imaging of protoporphyrin IX through determination of tissue optical properties in the spatial frequency domain. *Journal of Biomedical Optics*, *16*(12), 126013. doi:10.1117/1.3665440

Sanan, D. A., Newland, D. L., Tao, R., Marcovina, S., Wang, J., Mooser, V., … Hobbs, H. H. (1998). Low density lipoprotein receptor-negative mice expressing human apolipoprotein B-100 develop complex atherosclerotic lesions on a chow diet: no accentuation by apolipoprotein(a). *Proceedings of the National Academy of Sciences of the United States of America*, *95*(8), 4544–4549.

Sanz, J., & Fayad, Z. A. (2008). Imaging of atherosclerotic cardiovascular disease. *Nature*, *451*(7181), 953–957. doi:10.1038/nature06803

Sćepanović, O. R., Fitzmaurice, M., Miller, A., Kong, C.-R., Volynskaya, Z., Dasari, R. R., … Feld, M. S. (2011). Multimodal spectroscopy detects features of vulnerable atherosclerotic plaque. *Journal of Biomedical Optics*, *16*(1), 011009. doi:10.1117/1.3525287

Schulz, R. B., Ale, A., Sarantopoulos, A., Freyer, M., Söhngen, R., Zientkowska, M., & Ntziachristos, V. (2009). Hybrid fluorescence tomography/x-ray tomography improves reconstruction quality, 73700H–73700H. doi:10.1117/12.831714

Sexton, K., Davis, S. C., McClatchy, D., 3rd, Valdes, P. A., Kanick, S. C., Paulsen, K. D., … Pogue, B. W. (2013). Pulsed-light imaging for fluorescence guided surgery under normal room lighting. *Optics Letters*, *38*(17), 3249–3252.

Snyder, C., Kaushal, S., Kono, Y., Tran Cao, H., Hoffman, R., & Bouvet, M. (2009). Complementarity of ultrasound and fluorescence imaging in an orthotopic mouse model of pancreatic cancer. *BMC Cancer*, *9*(1), 106. doi:10.1186/1471-2407-9-106

Solomon, M., White, B. R., Nothdruft, R. E., Akers, W., Sudlow, G., Eggebrecht, A. T., … Culver, J. P. (2011). Video-rate fluorescence diffuse optical tomography for in vivo

sentinel lymph node imaging. *Biomedical Optics Express*, *2*(12), 3267–3277. doi:10.1364/BOE.2.003267

Sosnovik, D. E., Nahrendorf, M., Deliolanis, N., Novikov, M., Aikawa, E., Josephson, L., … Ntziachristos, V. (2007). Fluorescence Tomography and Magnetic Resonance Imaging of Myocardial Macrophage Infiltration in Infarcted Myocardium In Vivo. *Circulation*, *115*(11), 1384–1391. doi:10.1161/CIRCULATIONAHA.106.663351

Soubret, A., Ripoll, J., & Ntziachristos, V. (2005). Accuracy of fluorescent tomography in the presence of heterogeneities: Study of thenormalized born ratio. *IEEE Transactions on Medical Imaging*, *24*(10), 1377–1386.

Srinivasan, S., Ghadyani, H. R., Pogue, B. W., & Paulsen, K. D. (2010). A coupled finite element-boundary element method for modeling Diffusion equation in 3D multi-modality optical imaging. *Biomedical Optics Express*, *1*(2), 398–413. doi:10.1364/BOE.1.000398

Srinivasan, S., Pogue, B. W., Dehghani, H., Jiang, S., Song, X., & Paulsen, K. D. (2004). Improved quantification of small objects in near-infrared diffuse optical tomography. *Journal of Biomedical Optics*, *9*(6), 1161–1171. doi:10.1117/1.1803545

Sun, Y., Chaudhari, A. J., Lam, M., Xie, H., Yankelevich, D. R., Phipps, J., … Marcu, L. (2011). Multimodal characterization of compositional, structural and functional features of human atherosclerotic plaques. *Biomedical Optics Express*, *2*(8), 2288–2298. doi:10.1364/BOE.2.002288

Sun, Y., Sun, Y., Stephens, D., Xie, H., Phipps, J., Saroufeem, R., … Marcu, L. (2011). Dynamic tissue analysis using time- and wavelength-resolved fluorescence spectroscopy for atherosclerosis diagnosis. *Optics Express*, *19*(5), 3890–3901.

Sunar, U., Rohrbach, D. J., Morgan, J., Zeitouni, N., & Henderson, B. W. (2013). Quantification of PpIX concentration in basal cell carcinoma and squamous cell carcinoma models using spatial frequency domain imaging. *Biomedical Optics Express*, *4*(4), 531–537. doi:10.1364/BOE.4.000531

Takeda, M., & Mutoh, K. (1983). Fourier transform profilometry for the automatic measurement of 3-D object shapes. *Applied Optics*, *22*(24), 3977–3982. doi:10.1364/AO.22.003977

Talanov, V. S., Regino, C. A. S., Kobayashi, H., Bernardo, M., Choyke, P. L., & Brechbiel, M. W. (2006). Dendrimer-Based Nanoprobe for Dual Modality Magnetic Resonance and Fluorescence Imaging. *Nano Letters*, *6*(7), 1459–1463. doi:10.1021/nl060765q

Tan, Y., & Jiang, H. (2008). Diffuse optical tomography guided quantitative fluorescence molecular tomography. *Applied Optics*, *47*(12), 2011–2016. doi:10.1364/AO.47.002011

Tardif, J.-C., Lesage, F., Harel, F., Romeo, P., & Pressacco, J. (2011). Imaging Biomarkers in Atherosclerosis Trials. *Circulation: Cardiovascular Imaging*, *4*(3), 319–333. doi:10.1161/CIRCIMAGING.110.962001

Tawakol, A., Castano, A. P., Gad, F., Zahra, T., Bashian, G., Migrino, R. Q., … Hamblin, M. R. (2008). Intravascular detection of inflamed atherosclerotic plaques using a fluorescent photosensitizer targeted to the scavenger receptor. *Photochemical & Photobiological Sciences*, *7*(1), 33–39.

Themelis, G., Yoo, J. S., Soh, K.-S., Schulz, R., & Ntziachristos, V. (2009). Real-time intraoperative fluorescence imaging system using light-absorption correction. *Journal of Biomedical Optics*, *14*(6), 064012. doi:10.1117/1.3259362

Tichauer, K. M., Holt, R. W., El-Ghussein, F., Davis, S. C., Samkoe, K. S., Gunn, J. R., … Pogue, B. W. (2013). Dual-tracer background subtraction approach for fluorescent

molecular tomography. *Journal of Biomedical Optics*, *18*(1), 16003. doi:10.1117/1.JBO.18.1.016003

Tichauer, K. M., Holt, R. W., El-Ghussein, F., Zhu, Q., Dehghani, H., Leblond, F., & Pogue, B. W. (2011). Imaging workflow and calibration for CT-guided time-domain fluorescence tomography. *Biomedical Optics Express*, *2*(11), 3021–3036. doi:10.1364/BOE.2.003021

Vasefi, F., Belton, M., Kaminska, B., Chapman, G. H., & Carson, J. J. L. (2010). Angular domain fluorescence imaging for small animal research. *Journal of Biomedical Optics*, *15*(1), 016023. doi:10.1117/1.3281670

Vasefi, F., Ng, E., Kaminska, B., Chapman, G. H., Jordan, K., & Carson, J. J. L. (2009). Transmission and fluorescence angular domain optical projection tomography of turbid media. *Applied Optics*, *48*(33), 6448–6457.

Venugopal, V., Chen, J., & Intes, X. (2010). Development of an optical imaging platform for functional imaging of small animals using wide-field excitation. *Biomedical Optics Express*, *1*(1), 143–156. doi:10.1364/BOE.1.000143

Venugopal, V., Chen, J., Lesage, F., & Intes, X. (2010). Full-field time-resolved fluorescence tomography of small animals. *Optics Letters*, *35*(19), 3189–3191. doi:10.1364/OL.35.003189

Vinegoni, C., Razansky, D., Figueiredo, J.-L., Fexon, L., Pivovarov, M., Nahrendorf, M., … Weissleder, R. (2009). Born normalization for fluorescence optical projection tomography for whole heart imaging. *Journal of Visualized Experiments: JoVE*, (28). doi:10.3791/1389

Vinegoni, C., Razansky, D., Figueiredo, J.-L., Nahrendorf, M., Ntziachristos, V., & Weissleder, R. (2009). Normalized Born ratio for fluorescence optical projection tomography. *Optics Letters*, *34*(3), 319–321. doi:10.1364/OL.34.000319

Vinegoni, C., Razansky, D., Hilderbrand, S. A., Shao, F., Ntziachristos, V., & Weissleder, R. (2009). Transillumination fluorescence imaging in mice using biocompatible upconverting nanoparticles. *Optics Letters*, *34*(17), 2566–2568.

Vries, B. M. W. de, Hillebrands, J.-L., Dam, G. M. van, Tio, R. A., Jong, J. S. de, Slart, R. H. J. A., & Zeebregts, C. J. (2009). Multispectral Near-Infrared Fluorescence Molecular Imaging of Matrix Metalloproteinases in a Human Carotid Plaque Using a Matrix-Degrading Metalloproteinase–Sensitive Activatable Fluorescent Probe. *Circulation*, *119*(20), e534–e536. doi:10.1161/CIRCULATIONAHA.108.821389

Waldeck, J., Hager, F., Holtke, C., Lanckohr, C., von Wallbrunn, A., Torsello, G., … Bremer, C. (2008). Fluorescence Reflectance Imaging of Macrophage-Rich Atherosclerotic Plaques Using an v 3 Integrin-Targeted Fluorochrome. *Journal of Nuclear Medicine*, *49*(11), 1845–1851. doi:10.2967/jnumed.108.052514

Wallis de Vries, B. M., Hillebrands, J.-L., van Dam, G. M., Tio, R. A., de Jong, J. S., Slart, R. H. J. A., & Zeebregts, C. J. (2009). Multispectral Near-Infrared Fluorescence Molecular Imaging of Matrix Metalloproteinases in a Human Carotid Plaque Using a Matrix-Degrading Metalloproteinase-Sensitive Activatable Fluorescent Probe. *Circulation*, *119*(20), e534–536. doi:10.1161/CIRCULATIONAHA.108.821389

Wang, B., Zhao, Q., Barkey, N. M., Morse, D. L., & Jiang, H. (2012). Photoacoustic tomography and fluorescence molecular tomography: a comparative study based on indocyanine green. *Medical Physics*, *39*(5), 2512–2517. doi:10.1118/1.3700401

Wang, D., Liu, X., & Bai, J. (2009). Analysis of fast full angle fluorescence diffuse optical tomography with beam-forming illumination. *Optics Express*, *17*(24), 21376–21395.

Wang, L., Jacques, S. L., & Zheng, L. (1995). MCML—Monte Carlo modeling of light transport in multi-layered tissues. *Computer Methods and Programs in Biomedicine*, *47*(2), 131–146. doi:10.1016/0169-2607(95)01640-F

Wang, L. V., & Wu, H. (2007). *Biomedical Optics: Principles and Imaging* (1st ed.). Wiley-Interscience.

Weber, J. R., Cuccia, D. J., Johnson, W. R., Bearman, G. H., Durkin, A. J., Hsu, M., … Tromberg, B. J. (2011). Multispectral imaging of tissue absorption and scattering using spatial frequency domain imaging and a computed-tomography imaging spectrometer. *Journal of Biomedical Optics*, *16*(1), 011015. doi:10.1117/1.3528628

Weissleder, R., Tung, C.-H., Mahmood, U., & Bogdanov, A. (1999). In vivo imaging of tumors with protease-activated near-infrared fluorescent probes. *Nat Biotech*, *17*(4), 375–378. doi:10.1038/7933

Xie, H., Bec, J., Liu, J., Sun, Y., Lam, M., Yankelevich, D. R., & Marcu, L. (2012). Multispectral scanning time-resolved fluorescence spectroscopy (TRFS) technique for intravascular diagnosis. *Biomedical Optics Express*, *3*(7), 1521–1533. doi:10.1364/BOE.3.001521

Yalavarthy, P. K., Pogue, B. W., Dehghani, H., Carpenter, C. M., Jiang, S., & Paulsen, K. D. (2007). Structural information within regularization matrices improves near infrared diffuse optical tomography. *Optics Express*, *15*(13), 8043–8058. doi:10.1364/OE.15.008043

Yalavarthy, P. K., Pogue, B. W., Dehghani, H., & Paulsen, K. D. (2007). Weight-matrix structured regularization provides optimal generalized least-squares estimate in diffuse optical tomography. *Medical Physics*, *34*(6), 2085. doi:10.1118/1.2733803

Yuan, B., McClellan, S. R., Al-Mifgai, B. F., Growney, E. A., & Komolafe, O. A. (2009). A cost-efficient frequency domain fluorescence lifetime measurement system. *American Journal of Physics*, *78*(1), 28–34. doi:10.1119/1.3224765

Yuan, J., Bae, E., & Tai, X.-C. (2010). A study on continuous max-flow and min-cut approaches. In *2010 IEEE Conference on Computer Vision and Pattern Recognition (CVPR)* (pp. 2217–2224). doi:10.1109/CVPR.2010.5539903

Yuan, Z., Zhang, Q., Sobel, E. S., & Jiang, H. (2010). Image-guided optical spectroscopy in diagnosis of osteoarthritis: a clinical study. *Biomedical Optics Express*, *1*(1), 74–86. doi:10.1364/BOE.1.000074

Zacharopoulos, A. D., Svenmarker, P., Axelsson, J., Schweiger, M., Arridge, S. R., & Andersson-Engels, S. (2009). A matrix-free algorithm for multiple wavelength fluorescence tomography. *Optics Express*, *17*(5), 3042–3051. doi:10.1364/OE.17.003042

Zavattini, G., Vecchi, S., Mitchell, G., Weisser, U., Leahy, R. M., Pichler, B. J., … Cherry, S. R. (2006a). A hyperspectral fluorescence system for 3D in vivo optical imaging. *Physics in Medicine and Biology*, *51*(8), 2029–2043. doi:10.1088/0031-9155/51/8/005

Zavattini, G., Vecchi, S., Mitchell, G., Weisser, U., Leahy, R. M., Pichler, B. J., … Cherry, S. R. (2006b). A hyperspectral fluorescence system for 3D in vivo optical imaging. *Physics in Medicine and Biology*, *51*(8), 2029–2043.

Zhang, B., Cao, X., Liu, F., Liu, X., Wang, X., & Bai, J. (2011). Early-photon fluorescence tomography of a heterogeneous mouse model with the telegraph equation. *Applied Optics*, *50*(28), 5397–5407.

Zhang, Q., Chen, X., Qu, X., Liang, J., & Tian, J. (2012). Comparative studies of l(p)-regularization-based reconstruction algorithms for bioluminescence tomography. *Biomedical Optics Express*, *3*(11), 2916–2936. doi:10.1364/BOE.3.002916

Zhang, W., Wu, L., Li, J., Yi, X., Wang, X., Lu, Y., … Gao, F. (2013). Combined hemoglobin and fluorescence diffuse optical tomography for breast tumor diagnosis: a pilot study on time-domain methodology. *Biomedical Optics Express*, *4*(2), 331–348. doi:10.1364/BOE.4.000331

Zhang, X., Badea, C., Hood, G., Wetzel, A., Qi, Y., Stiles, J., & Johnson, G. A. (2011). High-resolution reconstruction of fluorescent inclusions in mouse thorax using anatomically guided sampling and parallel Monte Carlo computing. *Biomedical Optics Express*, *2*(9), 2449–2460. doi:10.1364/BOE.2.002449

Zhao, L., Abe, K., Barroso, M., & Intes, X. (2013). Active wide-field illumination for high-throughput fluorescence lifetime imaging. *Optics Letters*, *38*(19), 3976–3979.

Zhao, Q., Jiang, H., Cao, Z., Yang, L., Mao, H., & Lipowska, M. (2011). A handheld fluorescence molecular tomography system for intraoperative optical imaging of tumor margins. *Medical Physics*, *38*(11), 5873–5878. doi:10.1118/1.3641877

Zhao, Q., Spinelli, L., Bassi, A., Valentini, G., Contini, D., Torricelli, A., … Pifferi, A. (2011). Functional tomography using a time-gated ICCD camera. *Biomedical Optics Express*, *2*(3), 705–716. doi:10.1364/BOE.2.000705

Zhu, B., Rasmussen, J. C., Lu, Y., & Sevick-Muraca, E. M. (2010). Reduction of excitation light leakage to improve near-infrared fluorescence imaging for tissue surface and deep tissue imaging. *Medical Physics*, *37*(11), 5961–5970.

Zhu, Q., Dehghani, H., Tichauer, K. M., Holt, R. W., Vishwanath, K., Leblond, F., & Pogue, B. W. (2011). A three-dimensional finite element model and image reconstruction algorithm for time-domain fluorescence imaging in highly scattering media. *Physics in Medicine and Biology*, *56*(23), 7419–7434. doi:10.1088/0031-9155/56/23/006

Zhu, Q., Durduran, T., Ntziachristos, V., Holboke, M., & Yodh, A. G. (1999). Imager that combines near-infrared diffusive light and ultrasound. *Optics Letters*, *24*(15), 1050–1052. doi:10.1364/OL.24.001050

Zhu, Q., Huang, M., Chen, N., Zarfos, K., Jagjivan, B., Kane, M., … Kurtzman, H. S. (2003). Ultrasound-Guided Optical Tomographic Imaging of Malignant and Benign Breast Lesions: Initial Clinical Results of 19 Cases. *Neoplasia (New York, N.Y.)*, *5*(5), 379–388.